Parameter studies for the aeroacoustic design of helicopter rotors based on different methods

B.Sc. Dirk Rabe
Matr.-Nr.: 4033679

Supervisor: Dipl.-Ing. Gunther Andreas Wilke
Professors: Prof. Dr. Jan Werner Delfs
Prof. Dr.-Ing. Cord-Christian Rossow

Braunschweig, 24. Juli 2017

Eidesstattliche Erklärung

Ich erkläre hiermit an Eides statt, dass ich die vorliegende Masterarbeit „Parameter studies for the aeroacoustic design of helicopter rotors based on different methods“ selbstständig verfasst sowie alle benutzten Quellen und Hilfsmittel vollständig angegeben habe und dass die Arbeit nicht bereits als Prüfungsarbeit vorgelegen hat.

Statement in Lieu of an Oath

I hereby confirm that I have written the thesis „Parameter studies for the aeroacoustic design of helicopter rotors based on different methods“ on my own and that I have not used any other media or materials than the ones referred to in this thesis.

Braunschweig, 24. Juli 2017

Dirk Rabe

Abstract

The goal of this thesis is to perform a parametric study on planform parameters of rotor blades with variable fidelity methods. The aim is to investigate the effect of each parameter on emitted noise and how it can be reduced. In descent flight, the rotor blades hit vortices generated from the preceding blades. This noise is known as blade-vortex-interaction (BVI). To simulate the noise of BVI accurately, the vortices need to be simulated correctly. Therefore, a prescribed and a free wake model in combination with the blade element theory (BET) and an unsteady panel method (UPM) are used. These models promise a more efficient way to capture the vortices, compared to computational fluid dynamics (CFD).

The results of the wake models, UPM and the CFD are compared with experimental wind-tunnel tests from the HARTII, 7AD and ERATO campaigns. The wake models with the BET do not reach the noise levels or overpredict it. Additionally, they are not able to predict the correct amount of spread around the peaks. Although UPM predicts the number of peaks and the noise levels better, more offsets are calculated for the more advanced blades. The CFD results give coarse representations of the experiments and are in need of large computational resources. If more resources become available these results could be improved too. Hence, the wake models with the BET and UPM are used to perform the parametric study on the parameters chord length, anhedral, sweep and twist.

The summary of the parametric study is that each planform parameter is capable of reducing the emitted noise in descent-flight. The most promising results are obtained through the coupling of UPM with the BET. Reducing the chord length at the tip is reducing the overall noise level. Due to this change in planform, the size of the tip vortices increases, thus the blades do not hit the full vortex. An upwards directed tip is focusing the vortices at the tip of the blade and sets off the vortices above the rotor plane, so that the noise is even further reduced compared to reducing the chord length. Giving the blade a backward-forward swept tip is reducing the noise by similar amounts like anhedral. Twisting the blade has the least reduction capabilities compared to the other planform parameters.

Yet, contradictory results are obtained among the methods. Hence, further investigation using either windtunnel experiments or full blown CFD is necessary to validate the results from the parametric study.

Zusammenfassung

Das Ziel dieser Arbeit besteht darin die Blattparameter von Hubschrauberrotoren mit Verfahren unterschiedlicher Genauigkeit auf den verursachten Lärm hin zu untersuchen. Im Sinkflug verursacht ein Helikopter viel Lärm, hervorgerufen durch Blatt-Wirbel-Interaktion (BVI). Dabei treffen die Rotorblätter auf Wirbel, die von vorhergehenden Blättern erzeugt wurden. Dazu werden ein fixes und ein freies Wirbelmodell zusammen mit der Blatt-Elementen-Theorie (BET) genutzt. Des Weiteren wird ein instationäres Panel Verfahren (UPM) zusammen mit einem freien Wirbelmodell genutzt. Diese Methoden sind in der Lage die Wirbel effizienter als Verfahren der numerischen Strömungsmechanik (CFD) der aktuellen Generation vorherzusagen.

Die Ergebnisse der Methoden werden mit experimentellen Daten aus Windkanalmessungen für verschiedene Rotorblätter verglichen. Hierbei handelt es sich um das HARTII, 7AD und ERATO Blatt. Die Wirbelmodelle, die mit der BET zusammen genutzt werden sind nicht in der Lage das Lärmniveau der Experimente zu ermitteln. Des Weiteren sind sie nicht in der Lage die Lärmspitzen der einzelnen Rotoren korrekt wiederzugeben. Obwohl UPM die Lärmspitzen besser wiedergibt, entstehen größere Unterschiede bei verbesserten Blattgeometrien. Die CFD-Simulationen geben eine grobe Übersicht über das Lärmverhalten der einzelnen Rotoren wieder. Es ist sehr wahrscheinlich, dass diese Ergebnisse durch eine höhere Auflösung verbessert werden. Aufgrund der hohen Dauer für CFD Simulationen werden die BET, mit dem fixen und freien Wirbelmodell sowie UPM genutzt um die Parameterstudie durchzuführen. Bei den Parametern handelt es sich um die Blatttiefe, V-Stellung, Pfeilung und Verwindung.

Die Zusammenfassung der Parameterstudie ist, dass jeder Parameter die Möglichkeit besitzt den abgestrahlten Lärm im Sinkflug zu reduzieren. Von den verschiedenen Methoden, die für die Studie genutzt wurden, sind die Ergebnisse, die mit einer Kopplung aus UPM und BET erzielt wurden die Vielversprechensten. Eine kürzere Profiltiefe an der Blattspitze reduziert den globalen Lärm. Durch diese Änderung werden größere Wirbel erzeugt, die nicht mit voller Größe die nachfolgenden Blätter treffen. Eine nach oben gerichtete V-Stellung an der Blattspitze bewirkt, dass die Wirbel über der Rotorebene abgesetzt werden und der Lärm noch mehr reduziert werden kann, im Vergleich zur Verringerung der Profiltiefe. Eine rückwärts-vorwärts Pfeilung reduziert den Lärm ebenso gut wie die V-Stellung. Die Verwindung hat den geringsten Einfluss auf den abgestrahlten Lärm im Vergleich zu den anderen Blattparametern.

Allerdings zeigen die Ergbnisse der einzelnen Methoden unterschiedliche Tendenzen. Daher ist es notwendig zusätzliche Untersuchungen mit Windkanalexperimenten oder höher aufgelösten CFD-Rechnungen durchzuführen, um die Ergebnisse der Parameterstudie zu überprüfen.

Contents

List of Figures

List of Tables

Nomenclature

Acronyms

AH	Airbus Helicopters. formerly Eurocopter
APSIM [1]	Acoustic Prediction System base in Integral Method - Aeroacoustic Code developed by the DLR
ATR	Advanced Technology Rotor
BPF	Blade Passing Frequency
BVI	Blade Vortex Interaction
CAA	Computational Aeroacoustics
FW-H	Ffowcs William-Hawkings
HLRS	Hochleistungs Rechenzentrum Stuttgart
HSI	High Speed Impulsive
JST	Jameson-Schmidt-Turkel
LEE	Linearized Euler Equations
MR	Main Rotor
NACA	National Advisory Committee for Aeronautics
NASA	National Aeronautics and Space Administration
NS	Navier-Stokes-equations
RANS	Reynolds-Averaged-Navier-Stokes
RPM	Revolutions per minute
SPL	Sound Pressure Level
TR	Tail Rotor
BET	Blade Element Theory
EU	Euler solution of **FLOWer** [2] coupled with **HOST** [3]

CFD	Computational Fluid Dynamics
NS	Navier Stokes solution of **FLOWer** [2] coupled with **HOST** [3]
FLOWer [2]	**CFD** flow solver developed by the DLR
HOST [3]	Helicopter Overall Simulation Tool
MESIR [4]	Free wake model implemented in **HOST** [3]
METAR [5]	Prescribed wake model implemented in **HOST** [3]
UPM-BET	UPM coupled with **BET** [4]
UPM-METAR	UPM with one precalculation of **METAR** [5]
UPM [6]	Unsteady Panel Method developed by the DLR

Roman Letters

μ	Advance ratio
ψ	Azimuthal angle
θ	Pitch angle of rotor blades
θ_0	Collective pitch of rotor blades
θ_C	Cosine of cyclic pitch of rotor blades
θ_S	Sine of cyclic pitch of rotor blades
c_{ref}	Dimensionless chord length
Ma	Mach number
Ma_∞	Free stream Mach number
Ma_{tip}	Tip Mach number
R	Blade radius
r	Specific location on blade geometry
r/R	Dimensionless blade position

Greek Letters

Δ	Delta - Difference in Values
$\delta(f)$	Dirac delta

δ_{ij}	Kronecker delta
∇	Gradient operator
∂	Partial derivative operator
ρ	Air density
ρ_0	Air density in undisturbed medium
$\tilde{p}$	Root Mean Square of Sound Pressure
$\tilde{p}_{max}$	Maximum threshold of hearing
$\tilde{p}_{min} = p_{ref}$	Minimum threshold of hearing, reference value
$\vec{n}$	Unit normal vector
c	Speed of sound
dB	decibel
f	Frequency
l_i	Aerodynamic force acting on the fluid per unit area in the i-th direction
L_p	Sound pressure level
lg	Logarhitmic function/scale
n	Number of blades
p'	Unsteady sound pressure
$P\delta_{ij}$	Stress tensor for an inviscid fluid
P_{ij}	Compressive stress tensor
Pa	Pascal
t	Observer (reception) time
T_{ij}	Lighthill stress tensor
u_i	i-th component of the local fluid velocity
u_n	Local fluid velocity normal to the surface
v_i	i-th component of the surface velocity
v_n	Surface velocity in direction normal to the surface
x	Observer position vector, with components x_i
y	Source position vector, with components y_i
Hz	Hertz

Chapter 1

Introduction

1.1 Motivation

The helicopter has some unique abilities superseding those of common aircraft. Its ability to start and land vertically, to hover and to pan left and right make it ideal for maneuvers and missions in areas where normal aircrafts can not operate [7]. Especially urban areas are the scenes of helicopters where they do fly at a low altitude. Therefore, the population is exposed to emitted noise, that is a necessary byproduct of lift generation [8].

In figure 1.1, the complicated aeromechanics of a helicopter, that are fundamentally unsteady, are presented [9]. When the helicopter is hovering the wake of the rotor is pushed below the plane and the velocity of all blades are identical. In forward flight, the blades experience different velocities through the rotation of the rotor and the translatory forward speed of the helicopter. Furthermore does the helicopter operate near its own wake, which makes the understanding of vortex generation and interactions of the different structural parts even more important. These effects and the lack of its understanding are reasons why helicopters were introduced later than planes.

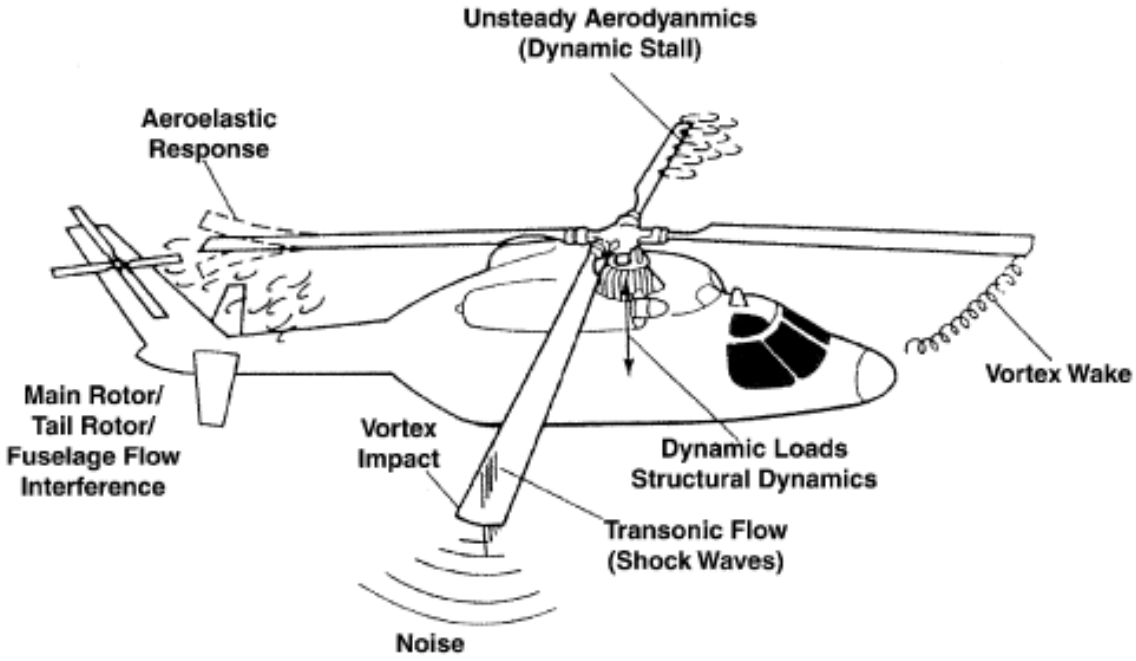

Figure 1.1: Aeromechanical environment of a helicopter [9]

At the beginning of aviation the emitted noise of aircraft was very high. Militaries were the

major user of aircrafts, therefore the noise was not a concern to deal with. When world war II ended, the amount of civil aircraft did rise up and with it the people exposed to aircraft noise. Schmitz [8] and Van der Wall et al [10] mention, that since then until today, there were and are different scientific programs to identify and reduce the emitted noise.

The major noise sources of a helicopter are the main rotor, tail rotor and the engine [11]. Due to improvements in engine design and ducted fans around the tail rotor, the noise of these sources has been reduced. In addition is the generated noise dependent on the flight state of the helicopter. Especially in descent and forward flight the emitted noise is annoying [12]. High speed impulsive (HSI) noise is generated when flying forward as described by Bebesel [13]. He also compares the effect of different rotor tip shapes on emitted noise. Kowarsch [12] and Yin [14] do research on the descent flight state, where the helicopter produces a lot of noise through blade vortex interaction (BVI) that is one of major concerns to deal with, when designing a helicopter.

BVI is caused by unsteady pressure fluctuations at the blades. These pressure fluctuations occur, when the blades and tip vortices, generated from preceding blades, hit each other. The vortices are not pushed out of the plane by the rotor thrust, nor do they convect as quickly as in level flight [14]. The problem with this kind of noise is the frequency range, in which it is emitted. The human ear is responsive from 20 Hz to 20 kHz. Sound that is generated at 3 to 4 kHz is a range where the ear is very receptive [15]. BVI occurs near that range and the helicopter is flying at a low altitude and has therefore a greater impact on the population than for flying at high altitudes.

1.2 State of the Art

The following chapter gives an insight in the necessary parts of helicopter aeroacoustic calculations. First, different methods for the determination of generated noise are described. Secondly, the different methods that are used to calculate the required aerodynamic and flight mechanical parameters are presented. Finally, recent work and research in blade tip design and parameters is presented.

1.2.1 Introducing Aeroacoustics

In figure 1.2, the directions of different helicopter noise sources are displayed. Although broadband noise is directed below the helicopter, its contribution to the overall emitted noise is small. HSI noise is present on the advancing blades, when the helicopter is flying forward at very high speeds, so that transonic areas are appearing. Thus, the thickness and loading noise are amplified by the high Mach numbers. The more concerning noise is BVI. This noise occurs through sudden rapid changes on the blades lift. The pressure fluctuations occur when the helicopter operates in descending or decelerating flight, where the blades pass parallel through the tip vortices from previous blades [8].

Lighthill formulated the acoustic wave equations, what was the beginning of the simulation of aerodynamic sound generation. Because of his formulated noise sources it was possible to determine the cause of sound back to turbulence. These sources are called the terms of Lighthill and are: turbulence, fluctuation in friction and entropy [15]. Ffowcs-William and Hawkings (FW-H) published their equation, which is used to combine the terms of Lighthill and thickness noise and loading noise on moving objects. This equation is seen as the basic form of the terms of Lighthill and may be used to determine the noise of the complex movements of a helicopter, especially in forward and descent flight to calculate HSI and BVI noise [16].

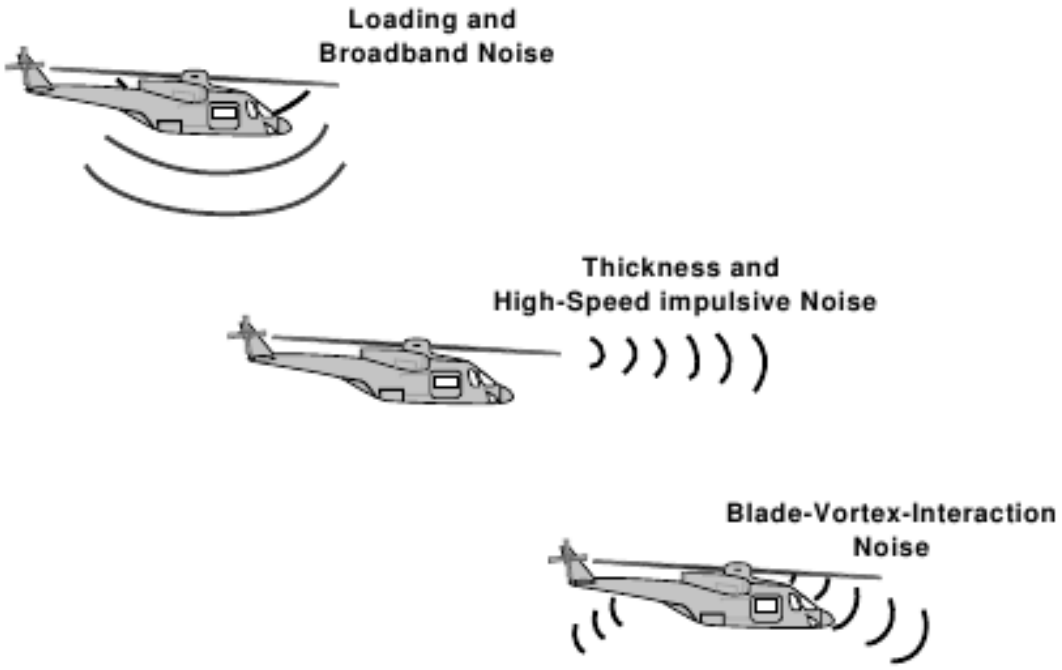

Figure 1.2: Helicopter noise directions of different sources [9]

An overview of possible methods in aeroacoustics is given by Brentner [17]. He describes three methods to simulate the noise generated by rotor blades:

- Computational Aeroacoustics (CAA)
- Hawkings formulation of Kirchhoff
- Ffowcs-William Hawkings (FW-H)

CAA is often referred to solve the linearized Euler equations (LEE). This method is expensive in computational effort because the mesh that is used has to be very fine in the whole flow field which raises the simulation time [18].

The next approach is the formulation of Kirchhoff, a derivative of the FW-H-equation. Brentner and Farassat [9] give reasons why it is unreliable for helicopter rotor noise. If the observer is 0.7 chords away from the blade surface then both methods, the FW-H and Kirchoff analogy, agree reasonable. If the pressure is calculated closer to the surface, the results become unrealistic [9].

The FW-H-equation solves three different source terms: the terms of Lighthill, loading noise and thickness noise [17]. Each of these terms have specifications that need to be fulfilled. Therefore, the already mentioned sources are mathematically described. Thickness noise is described by a monopole and it needs the geometry and the kinematics of the rotor blade. The loading noise is presented by a dipole and needs additionally the geometry and kinematic of the loads on the surface of the blade. The terms of Lighthill are described by a quadrupole and thus need the solution of the flow field around the blade to perform a volume integration. For the FW-H equation, the input data is used in the Farassat 1A formulation [19]. Thus, the deformed blade pressure surfaces are needed that are obtained from windtunnel experiments or simulations. A positive effect of FW-H based codes is that the computational effort is highly reduced in comparison to the LEE. However, the aerodynamic loads have to be obtained separately. Wide spread and known FW-H-based codes are for example the WOPWOP+ from NASA or TRAC (Tiltrotor Aeroacoustic Codes) [17].

1.2.2 Aerodynamical Methods

To compute the emitted noise, the loadings, surrounding pressure and the trim of the rotor blades are required. This leads to an aero-mechanical problem, which is in need of multiple disciplines for accurate modeling. The loads are calculated from aerodynamics. The structure of the blades are deformed elastically through aerodynamic and inertial forces. Finally, the flight mechanics are covered by the rigid-body motion which is required to account for blade dynamics as well as trim settings. This multidisciplinary problem of dynamics is usually solved by comprehensive codes. Kunz describes codes like CAMRAD, UMARC and RCAS [20].

The blade element theory (BET) computes the airloads on a rotor blade [21]. The forces are calculated from airfoil coefficient tables. The blade itself is discretized at the quarter chord line where the forces are computed in dependency of the inflow. The main advantage of the BET is the low computational effort and the robustness of it. However, no vortex structures are computed, therefore it is not suited for the already mentioned BVI-noise.

To resolve the vortex structures that are necessary for capturing the BVI event, the BET can be used together with wake models. There are two available approaches, the free and the prescribed wake models. The use of the Kutta-Joukowski lift theorem and the law of Biot-Savart are used to generate the wake of the rotor. The bound vortices of the blade are determined through the lift that is generated. Afterwards, the trailing wakes and the vortices are convected. Finally, the induced velocities are computed by the law of Biot-Savart. For the prescribed model the wake geometry is based on thrust, blade number and the flight condition [5]. The free wake model solves the geometry of the wake iteratively. This is done by convecting the vortices with induced velocities. Michea and Chauvin [4] mention that these models offer the possibility to resolve BVI. The general assumptions of these models are: incompressible, inviscid and irrotational flow.

Another technique are panel methods. The surface of the blade is divided in many panels instead of a line. These panels are described through velocity potentials. This method has the same assumptions as the wake models concerning the flow. The great advantage of a panel method is that together with a free wake model it is capable of resolving BVI-effect without the effort of an expensive computational fluid dynamics (CFD) simulation [14].

An expensive but more accurate way, to model the airloads offer the Euler- and RANS-(Reynolds-Averaged-Navier-Stokes) equations. They are capable of resolving 3D-effects at a rotor blade and in the flow field. The Euler equations are neglecting viscous effects, but are able to compute compressible flow. In combination with a turbulence model the RANS equations offer the possibility to account for viscosity. Kowarsch et al [12] simulated a complete H145 helicopter in descent flight with over 190 million grid cells at the High Performance Computing Center Stuttgart (HLRS). They state that this approach is unsuitable for parametric studies on blade design in the near future.

1.2.3 Overview of Rotor Blade Development

An overview of rotor blade designs is given by Brocklehurst and Barakos [11]. They compare the development of rotor blades with wings and mention where analogies exist. One analogy for example is the special treatment of the tip of a wing or blade. At the tip of planes, winglets are used to virtually increase the span and reduce the induced drag. The use of anhedral for rotor blades is also able to achieve a reduction in induced drag [22] [23].

In the opinion of Brocklehurst and Barakos [11], the early development of rotor blades was

focused on aerodynamics. New improvements in CFD helps to understand the influence of the parameters. The focus lies on the blade tip design where speed is highest and most lift and drag are generated. The emitted noise of a rotor blade is directly connected to the blade tip because of the high velocities which are directly responsible. When the helicopter is in hover the speed rises linearly up with the length of the rotor blade. As already mentioned this is different in forward or descent flight.

The four main planform parameters of a rotor blade are: chord length, an-/dihedral, sweep and twist. Each of the parameters has different influences on the performance of a helicopter and on the surrounding flow field. Each parameter has to be investigated independently and its influence on the emitted noise.

1.3 Objective of this Research

The objective of this thesis is to perform a parametric study on planform parameters with variable fidelity methods available to model rotor noise. The goal is to find a suitable method for optimization. Different existing rotor blades are investigated with different numerical tools.

In chapter 2, the basics of aeroacoustics and the used FW-H-code are described. Afterwards, different methods to compute the aerodynamics are described and compared with each other. Furthermore, the influences of the planform parameters of a rotor blade are given. In chapter 3, the results of the simulations of the rotor blades in descent flight are discussed. In chapter 4, the results of the parametric study of the used methods are displayed. Finally, the thesis is summarized to give a conclusion of the effectiveness of each parameter to reduce BVI-noise and which method is suitable for optimization.

Chapter 2

Theoretical Review

In the following chapter, an introduction in aeroacoustics and the used FW-H based code is given. Additionally, the variable methods and the planform parameters and their effects on the aerodynamics of a helicopter are presented. In figure 2.1, the order of the numerical process chain for aeroacoustic analysis is given. The sound is generated on a carpet of microphones to compare numerical results with the experimental ones. Before the sound pressure level (SPL) is computed, the loads on the rotor blades are needed. The loads are resolved with aerodynamic models of different fidelity implemented in HOST, UPM or FLOWer. To calculate the loads and vortices of a blade correctly, it is important to know the deformation of the blades. For this, the beam model of the comprehensive code HOST is used.

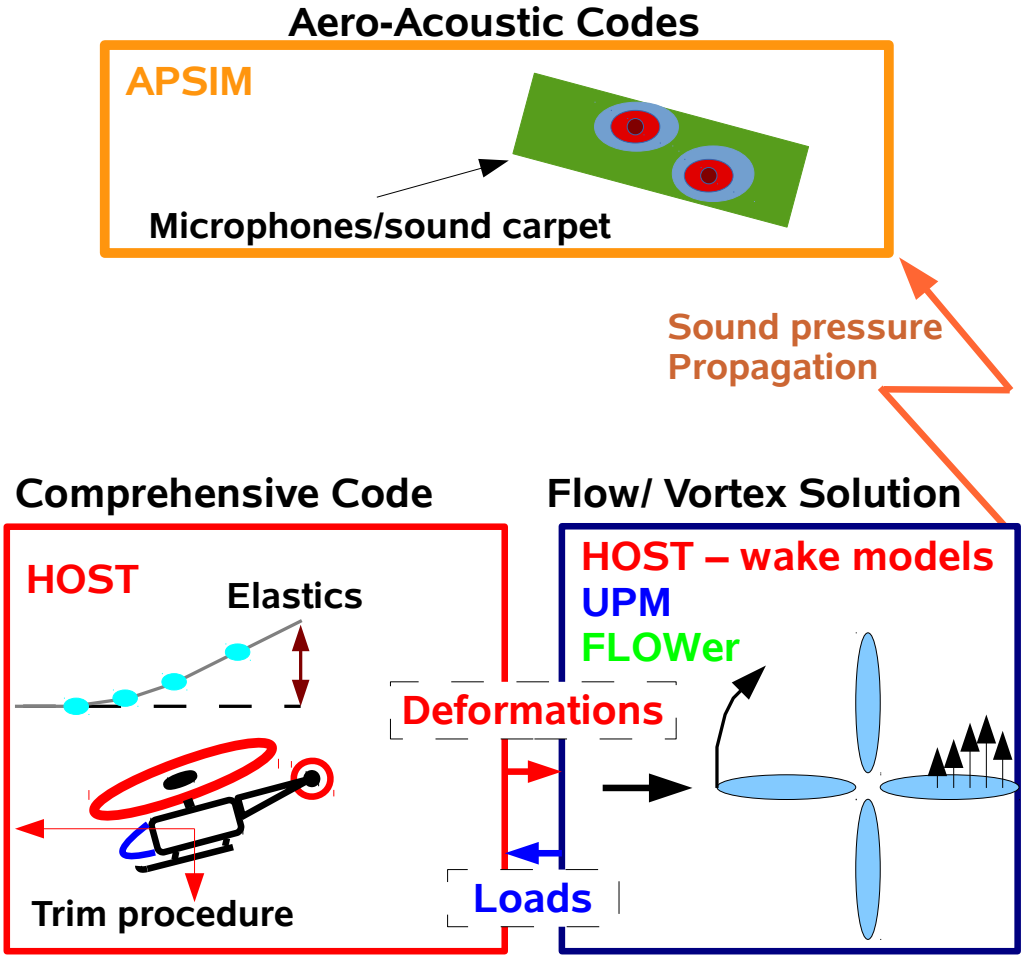

Figure 2.1: Process chain of numerical solution for aeroacoustic analysis

2.1 Introduction of the Basics of Aeroacoustics

In the following part, the basics of acoustics, aeroacoustics and the FW-H based code will be explained.

2.1.1 Basics of Acoustics

Due to differences in pressure signals, the stimulus in the human ear responses to it and perceives it as a perception of sound. The pressure range, the ear responds to, is very wide: 20 Hz to 20 kHz. The strength of an acoustic signal is set with the root mean square, where p' is the unsteady sound pressure [15]:

$$\tilde{p} = \sqrt{\overline{(p')^2}} \tag{2.1}$$

As already mentioned, the ear is capable of receiving a wide range of sound pressures. The minimum and maximum are the thresholds of hearing and pain respectively [15]:

- $\tilde{p}_{min} = p_{ref} = 10^{-5}\ Pa \approx 0\ dB$
- $\tilde{p}_{max} = 10^{2}\ Pa \approx 120\ dB$

The large range of pressure signals, the human ear can receive, sets the need for a readable level. The scientist Bel defined the sound pressure level (SPL) L_p $[dB]$ [15]:

$$L_p = 10 \lg \left(\frac{\tilde{p}}{p_{ref}} \right)^2 = 20 \lg \left(\frac{\tilde{p}}{p_{ref}} \right) \tag{2.2}$$

In figure 2.2, the perception of sound is displayed. Represented are the areas, where the human ear operates. Additionally to the dependancy of frequency, the noisiness of sound rises with [24]:

- Sound pressure (most dominating)
- Variation/Difference in time
- Content of information (speech, danger/siren)
- Tonality (peaks in the spectrum)

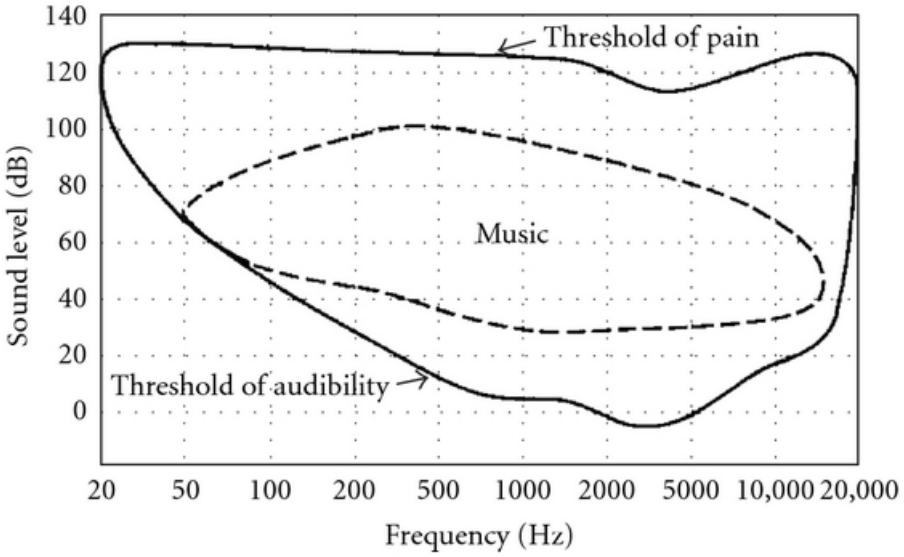

Figure 2.2: Perception of sound pressure level [25]

Because humans are individuals, a differentiation has to be made. Hence, a noise weighting is introduced to ease the handling with acoustics. Though signals are no pure tones of frequency, noise weighting helps to understand some basic characteristics of low noise designing. Internationally, four weightings (A-D) are agreed up on, yet the A-weighting is the most applied one. In figure 2.3, the noise weighting with A- and B-scale is presented. The focus lies on the A-scale. dBs are added or subtracted in dependency of the frequency to the SPL [15] [24]. Additionally, the range where BVI occurs is marked. Van der Wall et al [10] mentions that the Blade-Passing-Frequency, where BVI occurs is about $8 - 20$. The frequency range is calculated with the following equation:

$$f = BPF * n * RPM/60 \tag{2.3}$$

The number of blades is displayed by n and RPM are the revolutions per minute. Using this formula and assuming $RPM = 1000\ 1/min$, the boundaries of BVI are:

$$f = 533 - 1333Hz$$

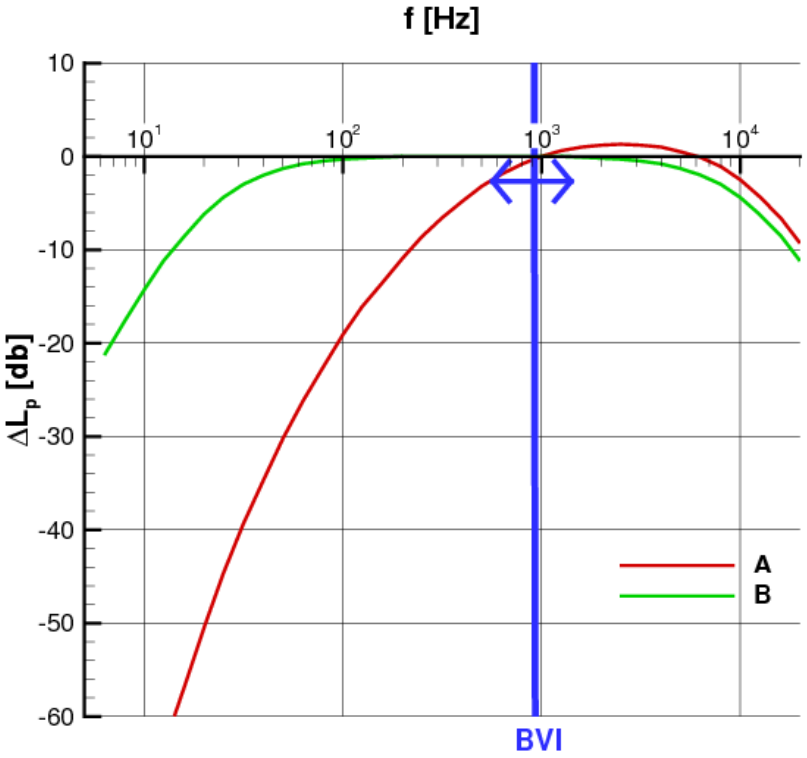

Figure 2.3: Noise weighting A/B-scale, logarithmic scaled frequency, [DIN-IEC 651]

2.1.2 Aeroacoustic

Aeroacoustics is the sound generation by aerodynamic means. Since the foundation of this field, a lot of effort was put into it, to understand the sources of aeroacoustics and to reduce its effects. For helicopter development this is challenging [12]. Schmitz [8] describes rotor noise as an inevitable by-product of necessary lift-generation for helicopters. He also mentions that a rotor in undisturbed air will create less noise than one in turbulent air. Turbulence causes local changes in blade loading, thus causing unsteady disturbances leading to more noise. In addition, he ranks the importance of helicopter noise sources:

1. Main-rotor impulsive
   - High-speed-impulsive (HSI)
   - Blade-vortex-interaction (BVI)
2. Tail rotor (TR)
3. Main rotor (MR) - loading and thickness noise
4. Engine/Transmission
5. MR/TR interaction

The concerning noise in this thesis is BVI. Key parameters for BVI are the advance ratio μ, tip Mach-number Ma_{tip} and the strength of the shed vortices. Altering the shape of the leading edge and the tip can reduce BVI events, shown by the Blue Edge^{TM} blade from Eurocopter [10]. In 1980, another attempt was to serrate the leading edge of a blade to reduce BVI noise [8]. It was shown that it has a positive aeroacoustic effect. But, each change in the planform of a blade, changes the effect on the aerodynamics and the dynamics of the blade, possibly reducing the effectiveness of the helicopter. That means each effect works both ways and can not be forseen. Hence, the effect of changing the planform parameters has to be investigated. It is infeasible if the emitted noise is 20 dB below each other helicopter and the new blade can not even lift the helicopter anymore with the crew.

The challenge to compute BVI is difficult, because of the excessive numerical dissipation implemented by state of the art 2nd order schemes. Kowarsch et al [12] mentions this problem and they performed simulations on a complete H145 helicopter via **CFD** with over 190 million grid cells and higher order schemes. This large number of cells requires a supercluster and is not applicable for industry nor parametric studies.

2.1.3 FW-H-Code APSIM

The Acoustic Prediction System base on Integral Method (APSIM) is developed at the DLR Institute of Aerodynamics and Flow Technologies. It is based on the Ffowcs-William Hawkings equation. Only linear sound propagation is taken into account [1]. APSIM solves the general FW-H equation that is obtained after rearranging the Navier-Stokes (NS) conservation equations. The general form of the FW-H equation for an inhomogeneous wave equation is the following:

$$\left(\frac{1}{c^2}\frac{\partial^2}{\partial t^2} - \nabla^2\right)[c^2(\rho-\rho_0)] = \frac{\partial^2}{\partial x_i \partial x_j}[T_{ij}] - \frac{\partial}{\partial x_i}\{[P_{ij}n_j + \rho n_i(u_n - v_n)]\delta(f)\} + \frac{\partial}{\partial t}\{[\rho_0 v_n + \rho(u_n - v_n)]\delta(f)\} \tag{2.4}$$

The symbol c is the speed of sound, t the observer reception time, ρ the density of air and ρ_0 the density in undisturbed air. The Lighthill stress tensor is displayed by T_{ij}, and x_i and x_j are the position of the observer. The fluid and surface velocity are described by u_n and v_n respectively, which are in direction normal to the surface. $\vec{n}$ is the unit normal vector. The compressive stress tensor is described by P_{ij} and $P_{ij} = P\delta_{ij}$ for an inviscid fluid. The Kronecker delta and the Dirac delta function are δ_{ij} and $\delta(f)$ respectively. If the observer is outside the source region, the notation $p' = c^2\rho' = c^2(\rho - \rho_0)$ can be used on the left hand side. Furthermore, when the surface $f(\vec{x}, t) = 0$ is on the body surface and not penetrable, that $u_n - v_n = 0$, then the classical FW-H equation is obtained:

$$\frac{1}{c^2}\frac{\partial^2 p'}{\partial t^2} - \nabla^2 p' = \frac{\partial^2}{\partial x_i \partial x_j}[T_{ij}] + \frac{\partial}{\partial t}[\rho_0 v_n \delta(f)] - \frac{\partial}{\partial x_j}[l_i \delta(f)] \tag{2.5}$$

The forces are on the right hand side of the equation. $\frac{\partial}{\partial t}[\rho_0 v_n \delta(f)]$ represents the thickness term, $\frac{\partial}{\partial x_j}[l_i \delta(f)]$ the loading term and the quadrupole term is described by $\frac{\partial^2}{\partial x_i \partial x_j}[T_{ij}]$. The different source terms has physical meaning only when the integral surface is located on a real impenetrable physical body. For the integral formulation two possibilities are implemented in APSIM [1]. For the following cases the deformed blade surface pressure 1A formulation of Farassat is used [19]. These pressure data are obtained from windtunnel experiments or numerical simulations. In addition, $\dot{dS}/dS$ surface dilatation effects are included [19].

2.2 Theoretical Review of Aerodynamic Methods

Figure 2.4 shows the approach to investigate the aerodynamics of rotor blades. The methods that are used to perform the investigations are the following: METAR, MESIR, UPM, EU and NS. The perceived fidelities and relative amount of computational time needed for the different methods is presented too. The theoretical basics and the physical effects that can be simulated are described in the following part for each method.

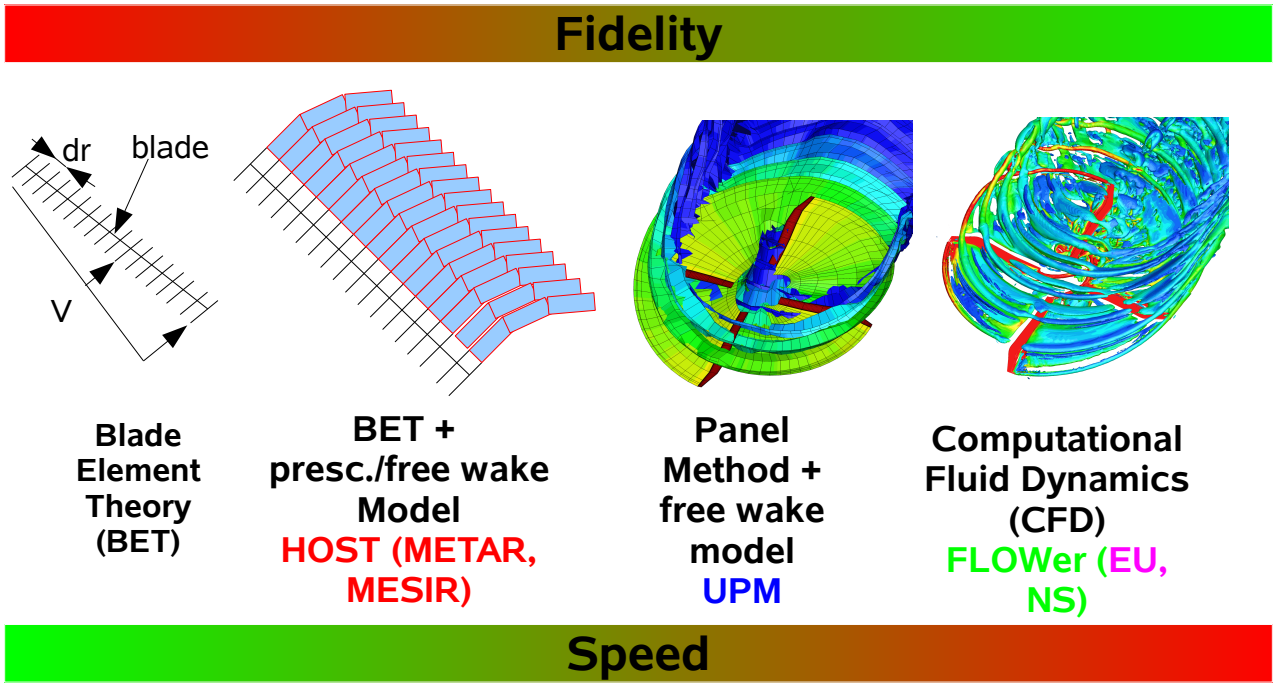

Figure 2.4: Different methods to investigate rotor blades dependent on time and fidelity

2.2.1 Blade Element Theory

The airloads of a rotor blade are computed with the blade element theory (BET). The blade is discretized along the quarter chord line [21]. From airfoil coefficient tables, the respective forces are computed. This method has drawbacks like limited accuracy and no vortex modeling. The viscosity and compressibility are given in airfoil tables. The determination of the inflow is non-trivial and thus, with the neglection of 3D-effects, not applicable for an aeroacoustic study. This method is implemented in the comprehensive code HOST (Helicopter Overall Simulation Tool) [3] developed by Airbus Helicopters (AH), formerly Eurocopter.

2.2.2 Vortex Modeling

The mentioned drawbacks of the **BET** may be compensated by the use of wake models. In the comprehensive code **HOST**, two wake models have been implemented. The prescribed wake model **METAR** [5] moves the vortices according to a semi-empirical definition. The free wake model **MESIR** [4] uses the induced velocities to move the filaments downstream. The free wake approach results in a better wake representation. The disadvantage of **MESIR** is the reduced stability in comparison to **METAR**, the prescribed model. Both types of wake modeling allow the resolution of BVI effects, but only take incompressible, inviscid, irrotational flow.

2.2.3 Panel Method

The surface of the rotor blades may be discretized via panels to improve the resolution of the tip vortices. The general assumptions for this method are the same as for the wake models: incompressible, inviscid and irrotational flow. Although incompressible flow is assumed, the Prandtl Glauert correction $1/\sqrt{|1-Ma^2|}$ is applied to each airfoil section to alleviate the compressible effect. Sources and sinks are used to describe the surface of the blade. This method is implemented in **UPM** (Unsteady Panel Method), developed by the DLR [26]. When there are shocks in the flow field this correction becomes invalid. **UPM** may be coupled with **HOST** to obtain a valid trim. This has been validated by Yin et al [14]. With **HOST** the forces, the trim and elastic effects are computed and afterwards with **UPM** the wake of the rotor. The great advantage of **UPM** over RANS based **CFD** is the little computational effort it requires.

2.2.4 CFD

The **CFD**-based, block structured finite-volume code **FLOWer** was also developed at the DLR [2]. In this study the Euler (**EU**) as well as the RANS (**NS**) equations are used. Time is progressed by using a 2^{nd} order dual time-stepping scheme, for which the inner iterations are calculated with a five step Runge-Kutta scheme [27]. For the rotor blades a 2^{nd} order Jameson-Schmidt-Turkel (JST) scheme is used [28]. The fuselage, for the **NS** simulations, uses a mixed version of the JST and Pade scheme. A 6^{th} order Pade filter is used for numerical dampening and the JST scheme is used to calculate the flux. These settings are taken from Wilke [27]. The Pade scheme is a compact higher-order finite difference scheme, developed by Lele [29]. The JST scheme is a finite volume approach, which also has a high level of robustness and flexibility.

With the Euler equations it is possible to resolve 3D and compressible effects and even BVI. It is possible that sonic events like shocks are not as well captured as in a RANS computation. For the RANS calculation a turbulence model is required to calculate the viscous effects, that are neglected in the Euler simulation. To get qualitatively correct results, the aeroelastics of the rotor blades must taken into account [30]. Thus, the solver **HOST** is used to calculate the trim and the deformations of the blades. The big advantage of **CFD**-methods over all other methods is the high resolution, but at high computational costs in terms of time. Another effect that can occur is that vortices dissipate too early and that BVI is not captured properly. This happens because of numerical viscosity that is necessary for a stable solution.

2.2.5 Comparison of Used Methods

In table 2.1, the main advantages and disadvantages of each method are displayed. The length of each simulation can not be determined at this point, but a higher fidelity usually leads to higher computational times. How the results from the simulations differ from the experiments can not be foretold either. How efficient each method in the end is, will be displayed in chapter 3.

Fidelity	Low		Mid	Mid-High	High
Methods	BET & prescr. wake model	BET & free wake model	Panel method & free wake	Euler	RANS
Boundary layer/ friction/ Laminar-turb./ transition	Tab ⊙-⊕	Tab ⊙-⊕	N/A ⊖	N/A ⊖	turb. model ⊕/ no laminar transition here
Compressible flow	Tab ⊖ - ⊙	Tab ⊖ - ⊙	CF ⊖	FS ⊕	FS ⊕⊕
Stall	Tab ⊙	Tab ⊙	N/A ⊖	FS ⊖	FS ⊕
Downwash	CF VX ⊙	CF VX ⊕	FS ⊕	FS ⊕	FS ⊕⊕
3D effects	CF VX ⊙	CF VX ⊙-⊕	VX ⊕	FS ⊕	FS ⊕
Vorticity	CF VX ⊙-⊕	CF VX ⊙-⊕	VX ⊕⊕	FS ⊕	FS ⊕
Numerical/ Artificial dissipation	Viscous core model			Numerical filter, Pressure sensor	
Applications	Acoustics Performance		Acoustics	Acoustics Performance	Performance Loads, Acoustics

Table 2.1: Accuracy of the different methods deduced from Wilke [31], Legend: CF - correction factors, FS - complete field solution, VX - velocity field, Tab - tabled data, ⊖ - poor/no, ⊙ - fair, ⊕ - good, ⊕⊕ - very good prediction capabilities

2.3 Aerodynamic Properties of Planform Parameters

In the following, the major planform parameters and their influence on the helicopter acoustics are presented. Additionally, the advantages and disadvantages of the parameters are compared. The parameters and the respective changes that can be made are displayed in figure 2.5, namely chord length, anhedral, sweep and twist. For further information on the development of modern rotor blades consult Brocklehurst and Barackos [11]. In table 2.2, an overview of the parameters and their influences is given. Especially the use of sweep already showed that it has a large impact on the emitted noise. The Blue Edge^{TM} blade developed by AH is a double swept blade [10]. An example for reduced chord length is the Ogee tip, explained by Brocklehurst and Barackos [11]. To understand each effect on its own, a parametric study on all four parameters will be conducted with the already described methods.

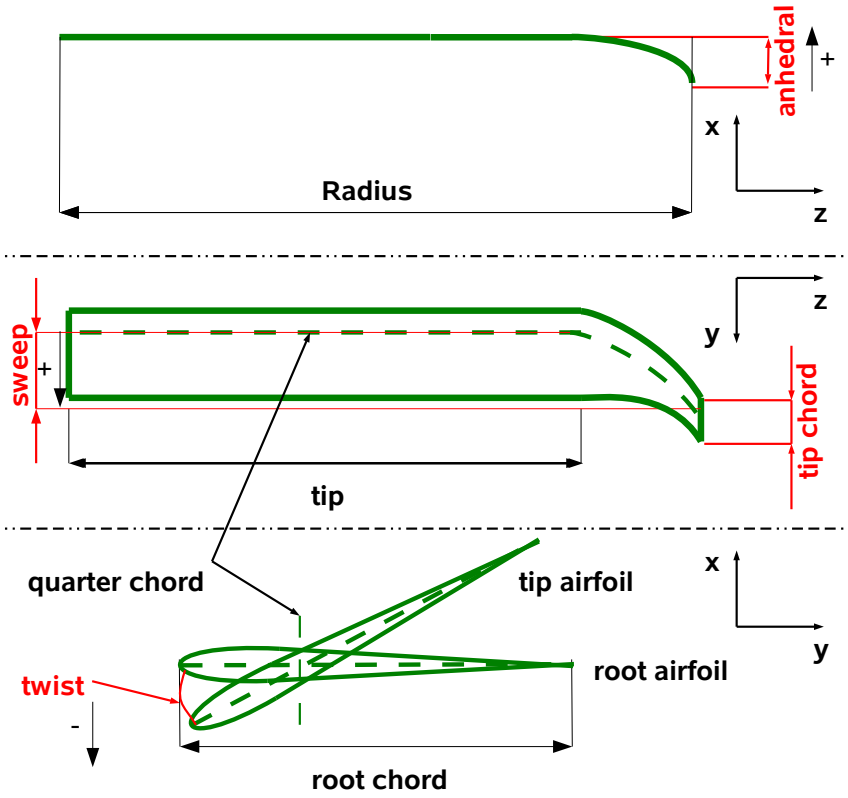

Figure 2.5: Major planform parameters of rotor blades [31]

Parameter	Physics	Advantages	Disadvantages
chord length decrease	area inflow distribution, friction	reduced (friction) drag, better circulation distribution	less lift, potential stall, decreased inertia (autorotation)
anhedral increase	vortex field	reduced induced drag, BVI reduction (acoustics), offset of vortices	structural challenges
sweep increase	compressibility	reduced transonic drag, circulation	structural instability
twist (negative) increase	angle of attack inflow distribution, vortex field	better circulation distribution, reduced induced drag	less lift, possible stall, vibrations

Table 2.2: Influence of major parameters and their advantages and disadvantages from [22] and [23]

2.3.1 Tapering and Chord Length Distribution

The circulation of the blade can be modified by increasing or decreasing the area. Another factor that is increased by a larger area is the viscous drag of the blade.

Tapering the leading and trailing edge can result in a swept blade. Connected with the sweep parameter very high sweep angles can be achieved. Aero-elastic blade deformations are influenced

by the change of mass through the chord distribution and the sweep [32].

To optimize this parameter, a tool that takes fluid-structural coupling into account is needed. To represent the design properly, transonic and inviscid as well as viscous effects need to be simulated.

The already mentioned Ogee tip is displayed in figure 2.6, which is designed to reduce noise [11]. The aim is to reduce peak velocities of the tip vortex, but a disadvantage of tapering is the possibility of stall due to an higher required blade pitch and less lift. If the noise is reduced to a certain level and the disadvantages made smaller, this could be a way to new helicopter rotor blades. This tip was never mounted on a production blade.

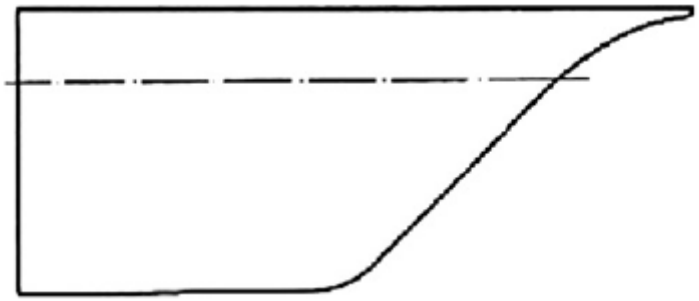

Figure 2.6: Ogee tip planform [11]

2.3.2 An-/Dihedral

The strength of tip vortices and their shed position is determined by the an- or dihedral of the blade. Through the decreased strength the induced power is lowered, thus the interaction with the next blade is also reduced. This leads to a reduced BVI-effect [11].

At modern airplanes, there are winglets at the tip of the wings. Yet, these do not underlay unsteady flow conditions. In forward flight, the strong aero-elastic effects on helicopter blades are the reason why there are no winglets. On one hand, Heilers [7] found out that in hover a winglet can be beneficial. On the other hand a mild dihedral is beneficial in forward flight [33]. However, these investigations are focused on the performance of a helicopter.

The simulation of the anhedral effects must be done correctly to model the tip vortices. Otherwise, BVI can not be captured properly. It is also crucial to model the fluid-structural coupling due to strong aero-elastic effects.

2.3.3 Sweep

The main purpose of a swept blade is the minimization of the transonic drag. At high revolutions per minute (RPM) and high speed forward flight, it happens that the tip operates in the transonic regime.

A forward swept blade is briefly mentioned by Brocklehurst and Barakos [11]. Due to the delaying of delocalization the noise is reduced. Especially for high impulsive noise at high Mach numbers this method becomes interesting. Wether or not forward swept blades are also effective at lower Mach numbers in descent flight is not mentioned.

The challenge when working with this parameter is the need of a fluid-structural coupling. This method needs to simulate compressibility effects, the vortex field around the blade and viscous effects, so that the aerodynamic torsional load on the blade are correctly represented. Imiela [34] mentions that the aeroelastic problems are the reason why there exist no strong swept blades.

Examples of swept blades are the **ERATO** blade or its derivative the Blue Edge^{TM}, displayed in figure 2.7 blade [10] [11]. The leading edge of the blade does not hit the parallel vortex.

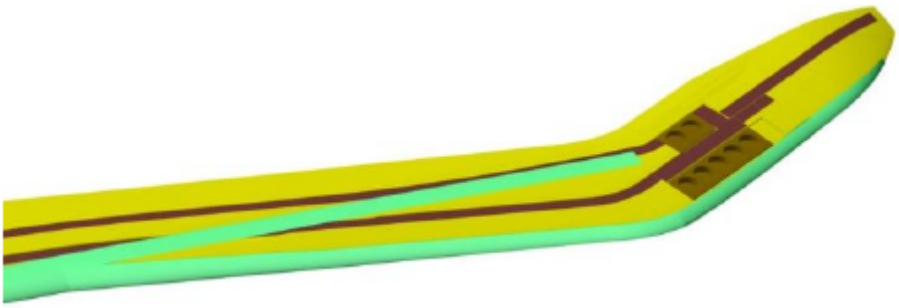

Figure 2.7: Blue Edge^{TM} blade structure [10]

2.3.4 Twist

The strongest effect on the performance of the rotor blade is the twist. It indirectly sets the angle of attack, which defines the circulation of the blade. The inflow is induced by the downwash and tip vortices of previous blades and thus directly affects the choice of twist for a blade. Another point of twist is the torsion of the blade. The torsion rises by the pitching from non-symmetric airfoils and an offset from the quarter chord to the elastic axis. This occurs due to sweeping or anhedral of the blade [34].

2.3.5 Aeroacoustic Review of the Parameters

A blade that was meant to receive all advantages of the effects with no boundaries, was the advanced technology rotor (ATR) [13]. Five different airfoils were used and a swept back tip. The aim was to design a blade that had low noise emissions and moderate loads. The effect of each parameter on the emitted noise could not been predicted. Yet, from the review of the already conducted research and regarding the Ogee tip [11] and the BlueEdge^{TM} [10] blade: It can be said that sweep and a smaller chord length at the tip have great potential to passively reduce rotor noise. Anhedral does affect the vortices directly and thus has a great potential to reduce BVI too. If a change of twist does affect the emitted noise can not be foretold. Hence, these four parameters will be changed over an acceptable and reasonable range to investigate the respected influences.

Chapter 3

Comparison of Numerical Methods for selected Rotor Blades

In the following chapter, the results of the methods described in chapter 2 are presented. The rotor blades are the **HARTII** [35], **7AD** and **ERATO** [36] blades, that were investigated in previous windtunnel experiments. These blades also represent different generations by aeroacoustic means, where the **ERATO** is the furthest developed one.

First, the combination of the methods and the respective discretizations are presented. In addition, the different descent flight conditions for each rotor blade is given. Afterwards, the results are depicted via trim angles, noise carpet, airloads and their derivatives.

3.1 Numerical Setup and Flight Conditions

The different methods, combinations, codes and their respective fidelities and solution approaches are listed below.

The wake models implemented in **HOST** are neither able to represent the fuselage of the rotor, nor the surface.

For the simulations with **UPM**, the fuselage is implemented, because noise is better captured, according to Yin et al [14]. The simulations of **UPM** are coupled with **HOST** that calculates the trim. Afterwards, **UPM** resolves the wake and loads of the rotor. **UPM-METAR** is coupled with **METAR** one time and **UPM-BET** is coupled with the **BET** five times.

Wilke [27] showed in his paper that it is possible to determine the noise of the **HARTII** rotor with **CFD** using 100 million points. He mentions the possibility to receive similar results by the use of less grid cells and a smaller time step size. This is tried in this thesis. The computational method uses a second order Jameson-Schmidt-Turkel (JST) scheme for the rotor and a fourth order Pade scheme for the background mesh. The fuselage for the **NS** uses a second order JST scheme and a sixth order filter. For more details see [27].

- Low-Fidelity (**HOST**)
  - **METAR**: **BET**+prescribed wake model (isolated rotor)
  - **MESIR**: **BET**+free wake model (isolated rotor)
- Mid-fidelity (**UPM**)
  - **UPM-METAR**: **UPM** in combination with **METAR** (4 blades + fuselage)
  - **UPM-BET**: **UPM** coupled with **BET** (4 blades + fuselage)

- Mid-High-fidelity (**FLOWer**)
  - **EU**: Euler (4 blades with 2^{nd} order JST scheme with 2^{nd} order filter, isolated rotor, background with 4^{th} order Pade scheme with 6^{th} order filter)
- High-fidelity (**FLOWer**)
  - **NS**: Navier-Stokes (4 blades with 2^{nd} order JST scheme with 2^{nd} order filter + fuselage with 2^{nd} order JST scheme and 6^{th} order filter, background with 4^{th} order Pade scheme with 6^{th} order filter)

In table 3.1, the individual surface discretization for each method is presented. For each method, the number of radial and chordwise points could be increased, but the resolution was chosen accordingly to the results of previous performed best practice studies, except for **METAR** or **MESIR** [27]. The number of chordwise panels for **UPM** and **FLOWer** must be sufficient enough, with emphasis on the leading edge, to correctly capture the suction peak, which strongly affects BVI.

Location	Radial	Chord	Stepsize [°]
METAR	39	1	2
MESIR	39	1	2
UPM-METAR	17	49	2
UPM-BET	17	49	2
EU	96	112	0.125
	≈20,000,000 grid cells		
NS	96	112	0.125
	≈20,000,000 grid cells		

Table 3.1: Individual discretization for each method including stepsize in degrees and grid size for **CFD**

In table 3.2, the flight conditions of the simulations for the descent flight are depicted. Additionally, the different RPM and blade radii are given. The lower RPM of the **ERATO** and thus the lower tip Mach number is one reason why this rotor emits less noise than the other two. The symbol R stands for the rotor radius, μ for the descent-rate and Ma_{tip} and Ma_{∞} for the tip Mach number and the free stream velocity respectively.

	HARTII	**7AD**	**ERATO**
$R\ [m]$	2.0	2.1	2.1
$RPM\ [1/min]$	1042	1022	946
$\mu\ [-]$	0.150	0.154	0.165
$Ma_{tip}[-]$	0.638	0.660	0.616
$Ma_{\infty}[-]$	0.096	0.102	0.102
Sense of rotation	ccw	cw	cw

Table 3.2: Descent flight conditions and sense of rotation: cw=clockwise, ccw=counter clockwise

3.2 Results of Variable Fidelity Methods for different Rotor Blades

The results for each rotor blade are presented individually. First, the blade planform and the noise carpet of the experiment are analyzed. Then, the trim results and the carpet plots of the simulations are compared with the experiment. Additionally, the airloads and their derivatives are presented to identify the causes for the differences between the simulations and the experiment.

3.2.1 HARTII

The **HARTII** blade is rectangular with one airfoil, the NACA 23012, and a linear twist distribution. The blade has neither sweep, nor anhedral, as seen in figures 3.1(a) and 3.1(c). As already mentioned, BVI shows an impulsive character and occurs in the mid frequency range around $8 - 20$ BPF [10]. Therefore, the following noise carpets are represented in that range. In previous experimental studies, thirteen equally distributed microphones in lateral direction and seventeen in downstream direction were placed [35]. At the same locations, the noise levels for the simulations are computed.

In figure 3.1(b), the noise carpet of the **HARTII** experiment is displayed. Additionally, the free stream direction, the radius of the blade and the direction of rotation are displayed, for orientation. In the noise carpet, two peaks are observed, one on the advancing side and one on the retreating side of the blade. These hotspots occur due to the rapid unsteady pressure changes on the rotor blades through vortex interaction with previously generated vortices. The different tip speeds on the advancing and retreating side are the reason why the SPL differs from each other. In addition, the second peak is not at $\psi = 270°$, due to the translatory flying speed of the helicopter and the directivity of the sound. The low noise between the hotspots occurs through the fuselage in the experiment.

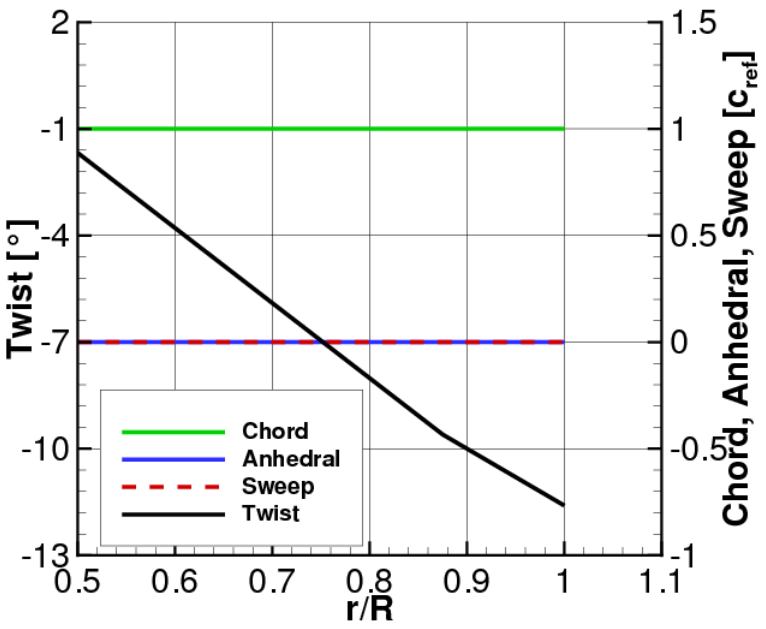

(a) Planform parameters **HARTII**

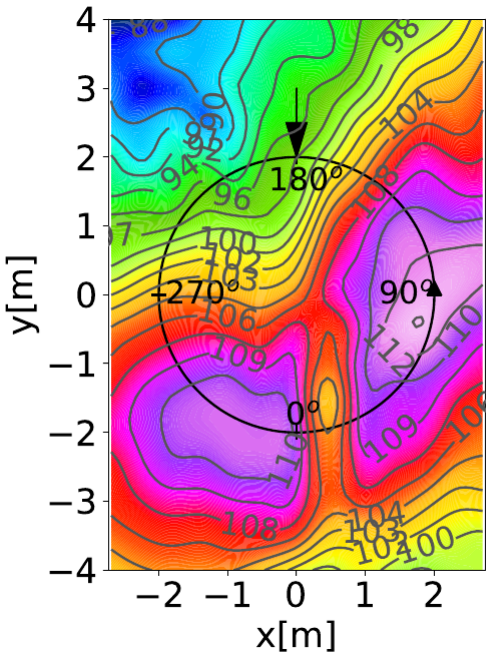

(b) SPL - **HARTII** experiment

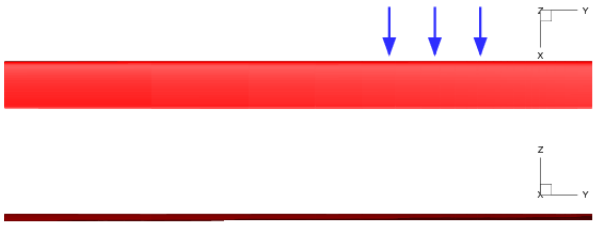

(c) Blade design **HARTII**

Figure 3.1: Planform and SPL $[dB]$ of the **HARTII** experiment

In table 3.3, the trim results for each simulation are displayed. θ_0 represents the collective pitch that sets the angle of attack for all rotor blades and is mainly responsible for the thrust. θ_C and θ_S are the cosine and sine portion of the cyclic pitch that are used to control the roll and pitch moment of the helicopter [7]. For additional visualization of the trim angles, calculated by the different methods, consult figure A.1 depicted in the appendix.

METAR shows small offsets for both cyclic angles, yet is able to capture the collective pitch. In figure 3.2(a), the noise carpet is displayed. Only one peak is calculated on the advancing side of the blade. Its location is overpredicted and the noise level is underpredicted by 3 dB. There is no sign of a second peak on the retreating side.

MESIR predicts even more offsets in all trim angles. Therefore, the blade location does not match the experiment and the vortices are differently resolved. This is the reason why the noise level in figure 3.2(b) is overpredicted by 1 to 3 dB and the hotspots are not isolated. A potential reason for the differences with the experiment is that METAR and MESIR are performed as isolated rotors with no fuselage.

UPM-METAR uses the METAR predicted trim angles for its own prediction of the vortex field. Therefore, UPM-METAR shows the same trim as METAR. In figure 3.2(c), the noise

carpet with an appropirate noise level is presented. The BVI peaks match the experiment in location and noise level with small discrepancies. The offsets in the trim angles may be the reason why there is no perfect match. The differences between **METAR** and **UPM-METAR** occur due to the different aerodynamic models.

UPM-BET receives the trim from iteratively coupling with **HOST**. The cyclic pitch is captured well, yet the collective shows the largest difference of all simulations. Through this difference, the location of the blade is wrong determined and thus the resolution of the vortices. This is a reason why only one peak is captured properly in figure 3.2(d). In addition, the noise level is 2 dB lower, compared to the experiment. The second peak at $(x = -1, y = -2)$ is not predicted as for **UPM-METAR**.

One similarity between the simulations performed with **HOST** and **UPM** is the prediction of the peak on the advancing side. The noise levels in **HOST** are either over or underpredicted, where **UPM** for the main peak matches the experiment well. Reasons for this behaviour is the neglection of the fuselage in **HOST** and the assumption of a line for the wake models, where **UPM** models the rotor as a surface and takes the displacement of the fuselage into account.

The collective pitch and sine portion of the cyclic pitch of the **CFD** simulations show nearly the same discrepancies, compared to the experiment. Only **NS** is able to capture the cosine pitch. The offset of the **EU** may be a reason why the hotspots in figure 3.2(e) are underpredicted by 3 to 5 dB. The center of both peaks show small differences compared to the experiment. A possible reason for this is the neglection of the fuselage. Unlike the low and mid fidelity simulations, **EU** is able to simulate the lowest noise outside the rotor disc in the top left corner. This noise level is close to the noise as in the experiment.

The **NS** simulation in figure 3.2(f) is also able to simulate this low noise in the corner, but is unable to simulate the second peak properly that is part of a twin peak. The main peak matches the experiment well, except that its noise level is 3 to 5 dB too low.

Although **CFD** is considered mid-high to high-fidelity, it is not able to identify BVI events as good as the simulation conducted with **UPM-METAR** and the noise is predicted too low. One reason for the behaviour of the **CFD** simulations may be the relative small number of grid cells used for the simulation, despite the fact that a higher order scheme is used. Wilke [27] shows that it is possible to better match the experiment by the use of about 100 million points.

HARTII			
Methods	$\theta_0[^\circ]$	$\theta_C[^\circ]$	$\theta_S[^\circ]$
Experiment	3.8	1.92	−1.34
METAR	3.78	1.71	−1.10
MESIR	3.64	1.58	−0.91
UPM-METAR	3.78	1.71	−1.10
UPM-BET	3.56	1.93	−1.11
EU	3.66	1.68	−1.05
NS	3.67	1.95	−1.02

Table 3.3: Different trim results of the **HARTII** simulation

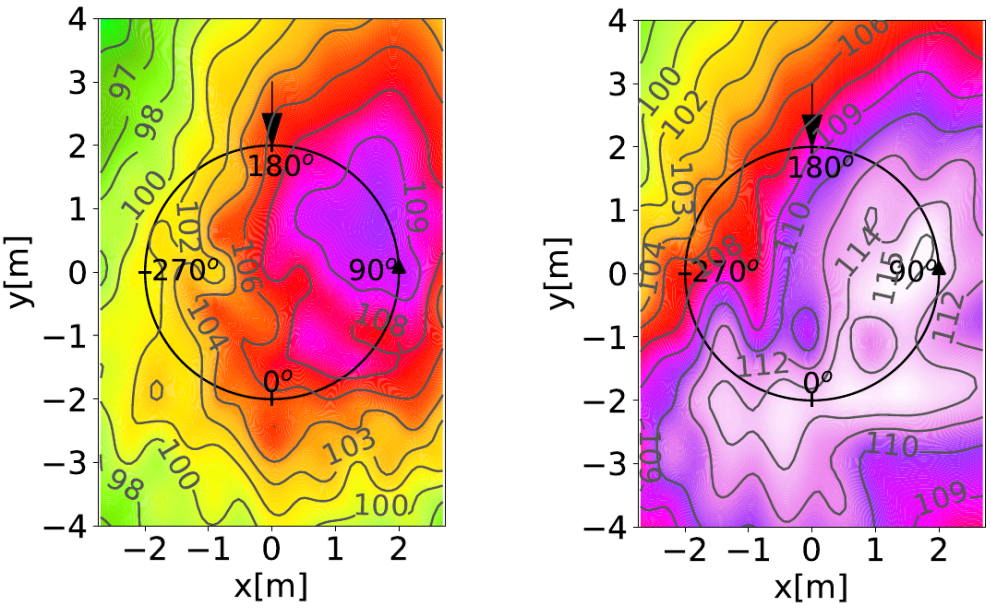

(a) SPL - **METAR**

(b) SPL - **MESIR**

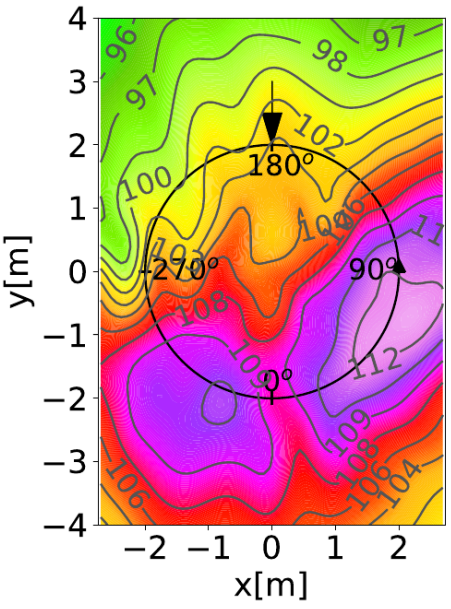

(c) SPL - **UPM-METAR**

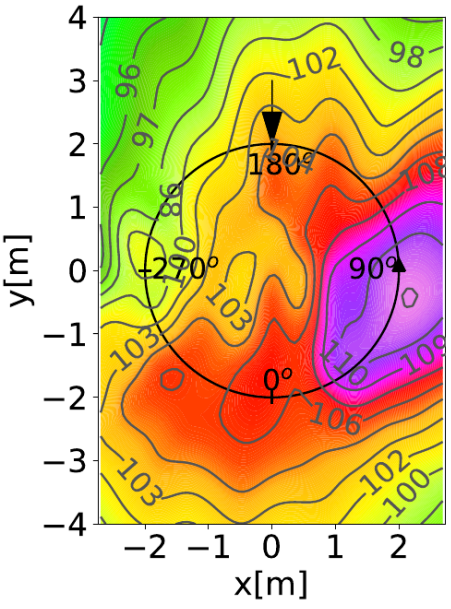

(d) SPL - **UPM-BET**

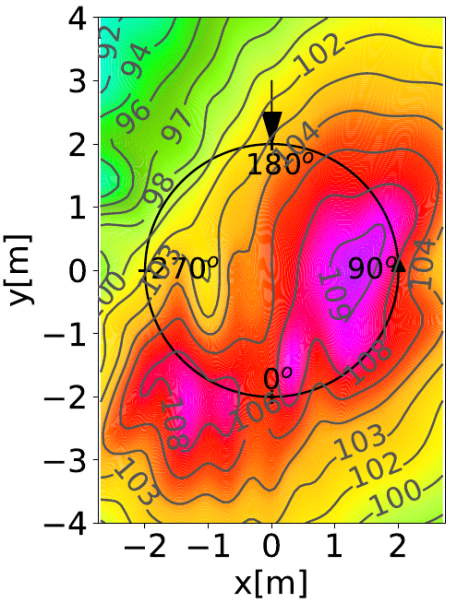

(e) SPL - **EU**

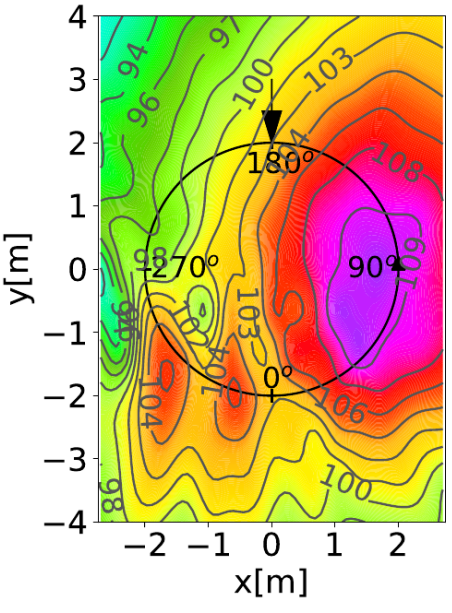

(f) SPL - **NS**

Figure 3.2: SPL [dB] plots for the **HARTII** blade

In figure 3.3, the load-coefficients, $c_n M^2$ and their temporal derivatives $\frac{dc_n M^2}{d\psi}$ for each investigated method and the experiment are displayed. The location of the radial cut of the blade is at $r/R = 0.87$.

The normal forces from **METAR** and **MESIR** are displayed in figure 3.3(a). **METAR** underpredicts the airloads from $\psi = 0°$ to $\psi = 130°$ on the advancing side of the blade. On the retreating side, from $\psi = 240°$ to $\psi = 330°$ too low loads and high frequency oscillations with small amplitudes are generated. In figure 3.3(b), the derivatives of the loads are depicted. These oscillations are directly connected to the emitted noise. Although the amplitudes are higher than in the experiment, the oscillations do occur later, where the tip Mach number is smaller. Hence, the noise generated is lower.

MESIR also underpredicts the airloads as **METAR**, yet the peaks do occur at the same time as in the experiment. The amplitudes of the fluctuations are larger on the retreating side of the blade. The derivatives are displayed in figure 3.3(b). Observing the peaks from $\psi = 270°$ to $\psi = 90°$, one long high frequency oscillation is identified. Therefore, the peaks are not as isolated as in the other carpets. The higher calculated amplitudes in connection with the respective tip Mach numbers are the reason why the noise is overpredicted with **MESIR**.

In figure 3.3(c), the results from **UPM** are displayed, where **UPM-METAR** underpredicts the loads on the advancing side from $\psi = 0°$ to $\psi = 100°$. On the retreating side they match the experiment with a small offset. The derivatives, in figure 3.3(d), show similar results as the loads in terms of locationand wiggles across the curve. The small offsets and the last false prediction of **UPM-METAR**, near $\psi = 360°$ that do not occur in the experiment, are the reason why the noise carpet do not fit with the experiment.

UPM-BET underpredicts the loads across the complete graph except at $\psi = 270°$, where it shows a match with the experiment. Although it is able to match the number and location of the peaks with small offsets, it is not able to match their strength. This is better presented in figure 3.3(d), where the wiggles with smaller amplitudes are identified. The smaller amplitudes are accountable for the lower noise than the experiment.

EU and **NS** are able to match the form of the experiment, yet both underpredict the loads, displayed in figure 3.3(e). **EU** shows less and weaker oscillations on the advancing side and smaller values with the same phase as the experiment on the retreating side. The location of the derivatives in figure 3.3(f) matches the experiment well. Yet, the amplitudes are too small, thus less noise, compared to the experiment is generated.

NS determines even less oscillations than **EU** with even smaller amplitudes on both sides. The peak in figure 3.3(f) that has the same amplitude like the experiment is the reason for the main peak in the **NS** noise carpet. As already seen for **MESIR**, in figure 3.3(b), both **CFD** methods show a similar behaviour and long oscillations with small amplitudes from $\psi = 270°$ to $\psi = 90°$. Therefore, the noise carpet for **EU** shows no isolated peaks and **NS** the twin peak.

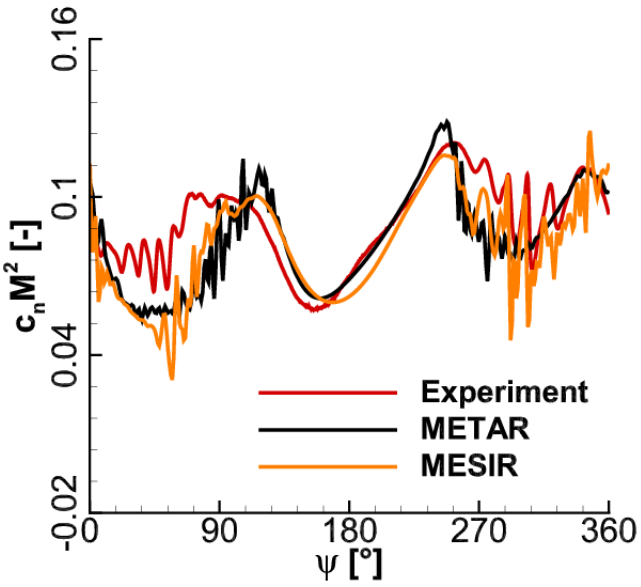

(a) Loads - **HOST**

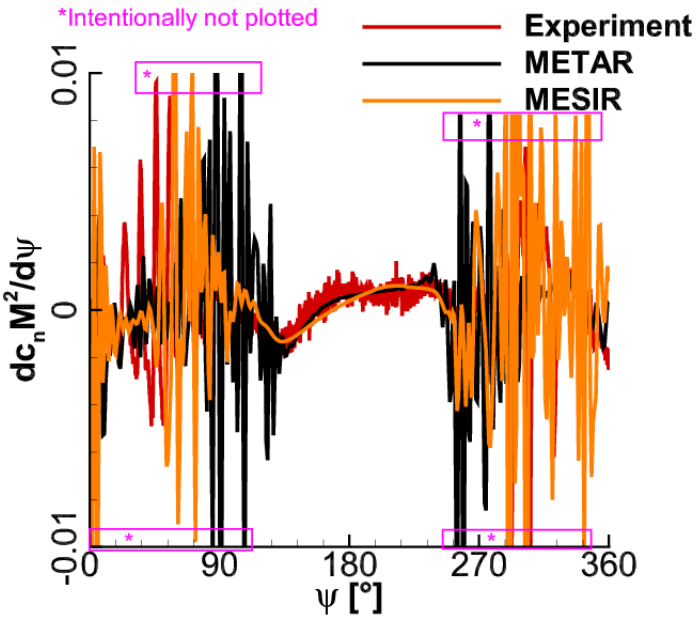

(b) Derivatives - **HOST**

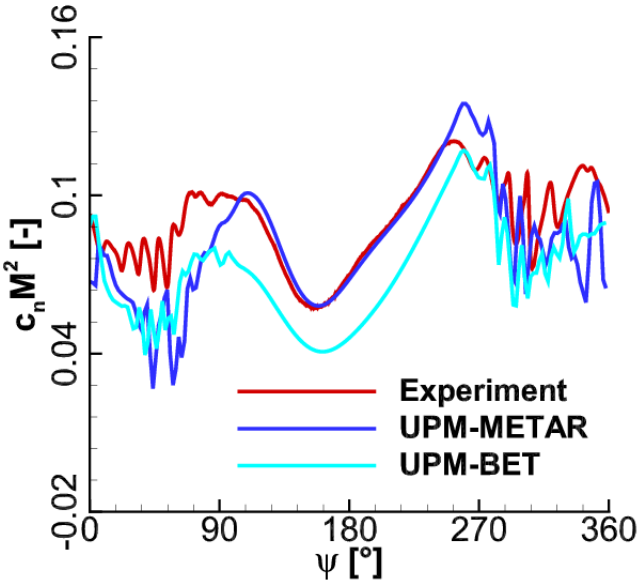

(c) Loads - **UPM**

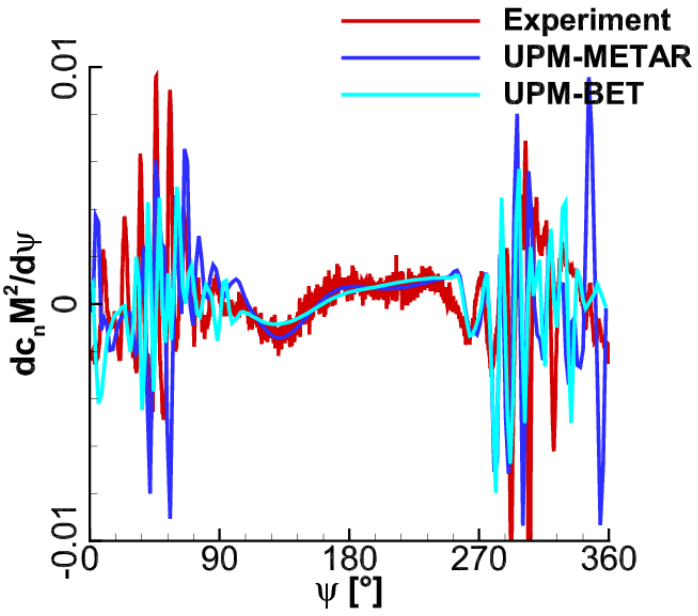

(d) Derivatives - **UPM**

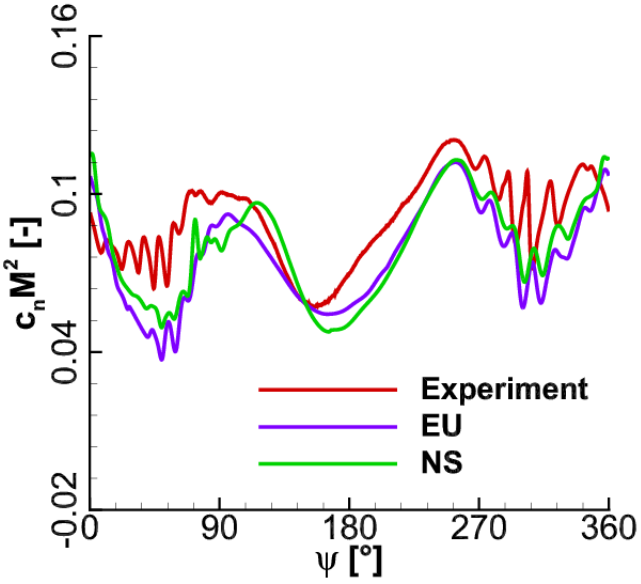

(e) Loads - **FLOWer**

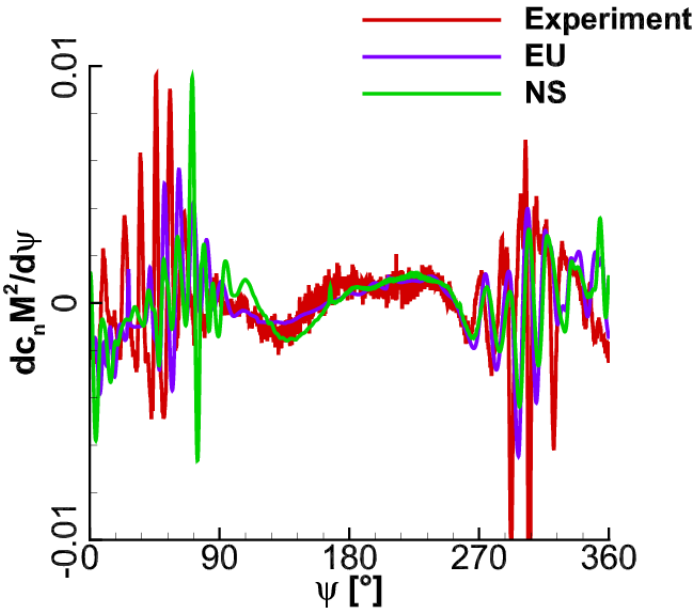

(f) Derivatives - **FLOWer**

Figure 3.3: Loads and derivatives of the **HARTII** for variable methods at $r/R = 0.87$

3.2.2 7AD

The **7AD** blade is the baseline for the **ERATO** program. Unlike the **HARTII** blade, it has a swept back tip and an anhedral downwards, seen in figures 3.4(a) and 3.4(c). Additionally, it is made of two different airfoils from the OA200 series. In figure 3.4(b), the noise carpet of the experiment is presented. First, it is mentionable that both, **7AD** and **ERATO**, have the opposite direction of rotation than the **HARTII**. Second, the **7AD** has one main peak on the advancing side and two smaller peaks on the retreating side. The locations of the main peak at $(x = -2, y = 0)$ and the smaller peak at $(x = 1, y = -2)$ approximately match the **HARTII** experiment, but the maximum noise generated is higher. Although the RPM from the **7AD** are less than the **HARTII**, its radius is larger, hence the tip Mach number is increased, thus more noise is emitted.

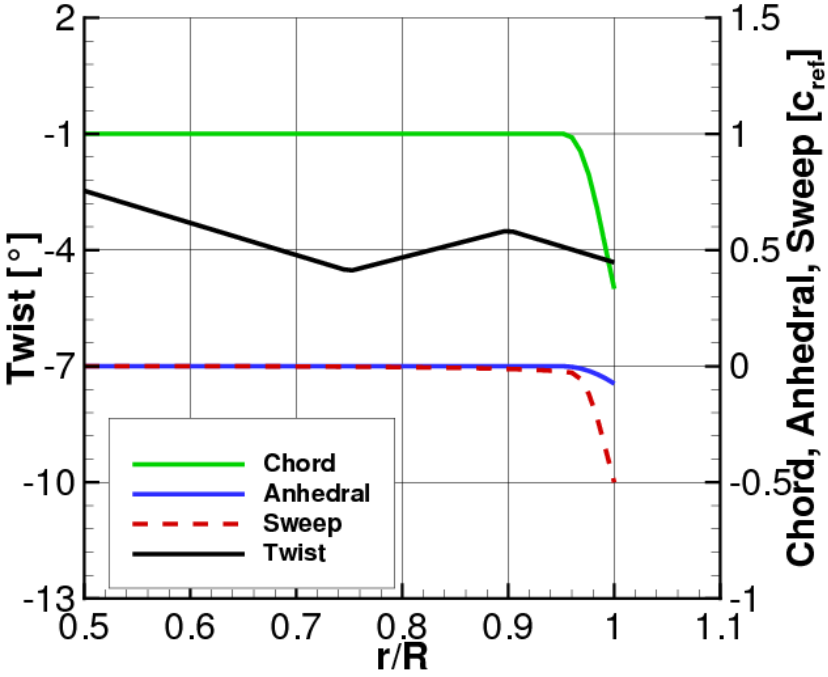

(a) Planform parameters **7AD**

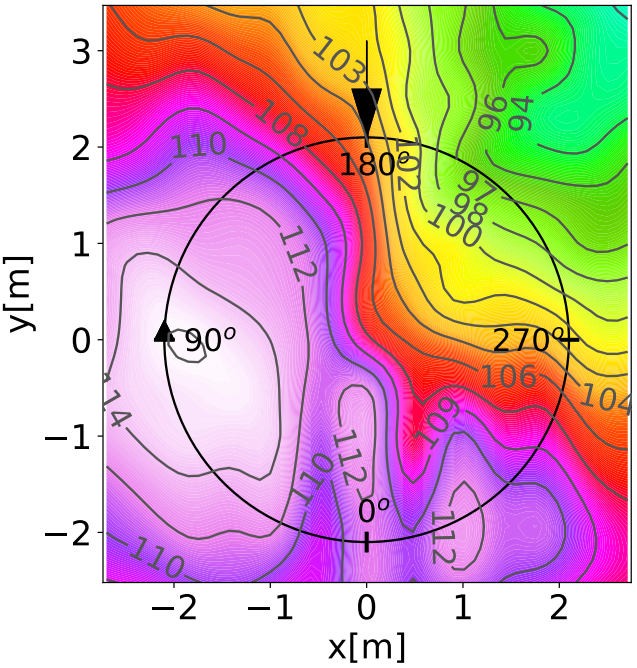

(b) SPL - **7AD** experiment

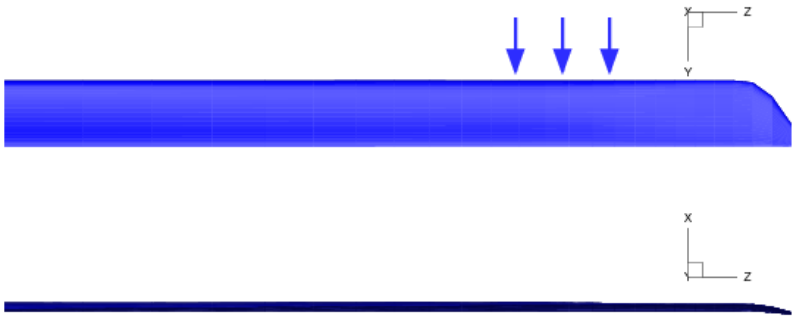

(c) Blade design **7AD**

Figure 3.4: Planform and SPL $[dB]$ of the **7AD** experiment

In table 3.4, the trim angles of the different methods are presented for the **7AD**. As already mentioned for the **HARTII**, the trim angles for the **7AD** are also depicted in the appendix in figure A.2(a).

METAR does not match the collective and cosine portion of the cyclic pitch angles in comparison to the experiment. The large offsets of the different angles may be a reason why the noise carpet, in figure 3.5(a) for METAR, is false predicted in terms of location and number of peaks. As already seen at the **HARTII** carpet for METAR, the main peak is also positioned upstream on the advancing side. The two smaller peaks on the retreating side near $\psi = 0°$ are not simulated at all.

The trim angles computed by MESIR show the largest deviation for the collective pitch, compared the experiment. In contrast, the cyclic pitch is captured better. The noise, displayed in figure 3.5(b) shows large differences to experiment. First, it predicts two peaks, one on the

advancing side of the blade and one inside the rotor disc. In addition, a larger emission of noise than the experiment is observed. The noise level of the left peak nearly matches the experiment. Although **MESIR** has larger differences to the experiment than **METAR**, it is able to simulate the smaller peaks with small offsets from the experiment near $\psi = 0°$ and $\psi = 300°$.

UPM-METAR underpredicts the noise level by 4 to 5 dB in figure 3.5(c), yet is able to capture one of the smaller peaks from the experiment at $(x = 1, y = -1.5)$. Although the prediction is not well, the low noise level in the top right corner is captured very well.

UPM-BET underpredicts the collective and sine portion of the cyclic pitch and overpredicts the cosine cyclic pitch. Although the deviations are bigger than **UPM-METAR**, **UPM-BET**, seen in figure 3.5(d), is able to give a good representation of the experiment for the **7AD**. The main noise level is 2 to 3 dB lower than the experiment. However, the contour of the experiment is predicted well. Furthermore, the second peak near $\psi = 0°$ and the third peak as a twin peak near $\psi = 300°$ are simulated.

Both **CFD** methods predict similar collective pitch angles, yet only **EU** is able to match the cyclic angles. **NS** shows the largest offsets for both cyclic pitch angles. These offsets are one reason why a similar behaviour like for **UPM-METAR** is observed. The noise carpet for **EU** is displayed in figure 3.5(e). The overall noise level is too low, yet it is able to simulate one of the smaller peaks as a twin peak, located at $(x = 0, y = -2)$. The third peak is located near $(x = 2, y = -1)$. Comparing these results and the ones from the **HARTII**, **EU** is not able to predict the top right corner well.

In figure 3.5(f), the noise for the **NS** is too small predicted too, compared to the experiment. Like **UPM-BET**, it is able to simulate the smaller peaks of the experiment. The twin peaks were already observed in the **HARTII** noise carpet in figure 3.2(f).

7AD			
Methods	$\theta_0[°]$	$\theta_C[°]$	$\theta_S[°]$
Experiment	6.53	2.15	−0.77
METAR	6.21	2.36	−0.76
MESIR	5.89	2.26	−0.56
UPM-METAR	6.21	2.36	−0.76
UPM-BET	6.25	2.44	−0.95
EU	6.33	2.13	−0.81
NS	6.30	2.72	−1.21

Table 3.4: Trim results of the **7AD** simulation

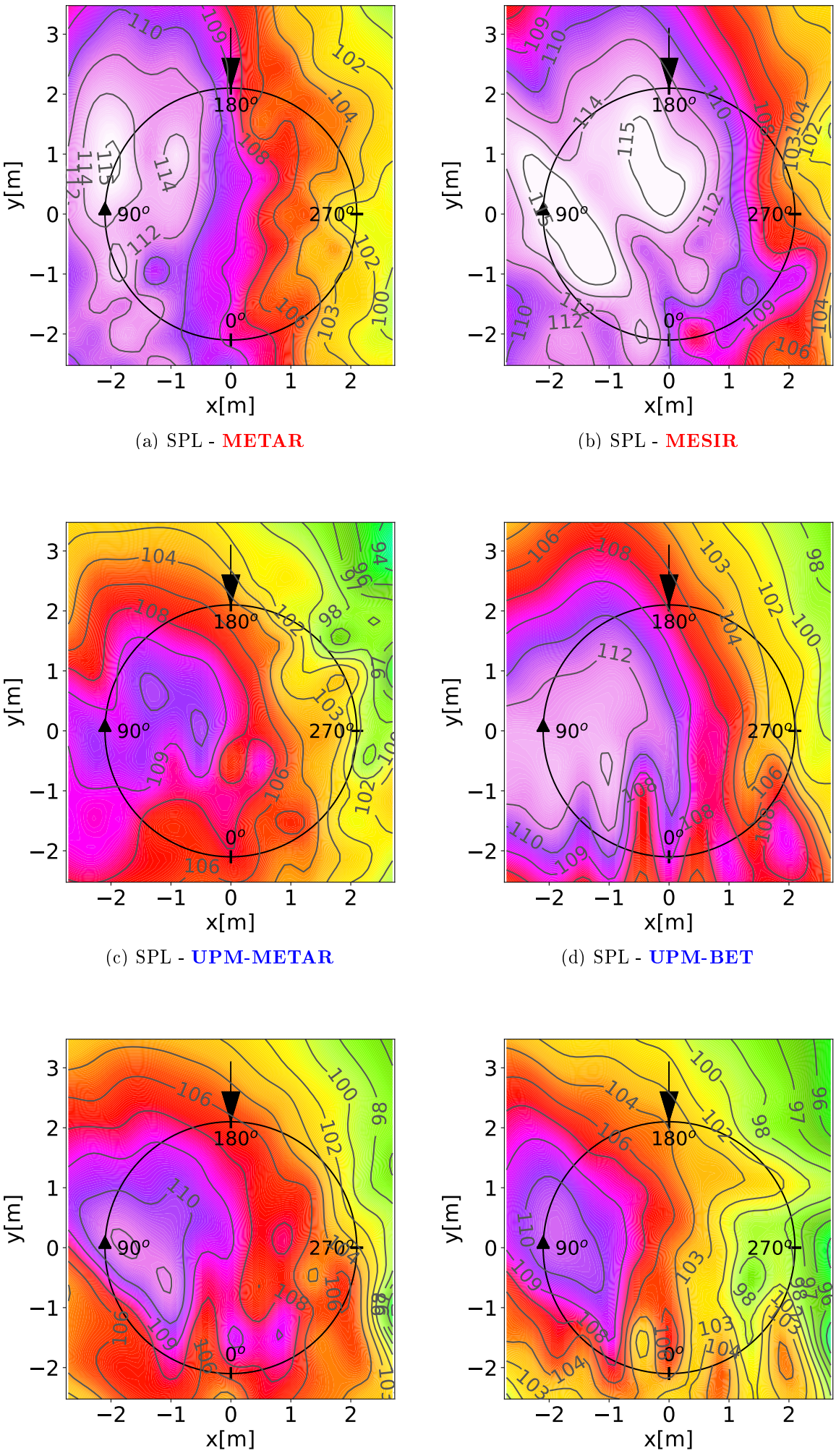

(a) SPL - **METAR**

(b) SPL - **MESIR**

(c) SPL - **UPM-METAR**

(d) SPL - **UPM-BET**

(e) SPL - **EU**

(f) SPL - **NS**

Figure 3.5: SPL [dB] plots for the **7AD** blade

In figure 3.6, the loads and their temporal derivatives for the investigated methods and the experiment are displayed. The location of the radial cut is at $r/R = 0.825$ of the blade geometry.

On the advancing and retreating side, both **METAR** and **MESIR** underpredict the integral loads compared to the experiment, seen in figure 3.6(a). Both also simulate a lot of oscillations with small and big amplitudes. As already seen for the **HARTII** blade, **METAR** also predicts more fluctuations than the experiment seen at $\psi = 100°$. At $\psi = 180°$ **METAR** overpredicts the integral airloads compared to the experiment, yet **MESIR** is able to match it well in this area. On the retreating side at $\psi = 270°$, both methods are close, yet **METAR** generates small oscillations and **MESIR** simulates more fluctuations with smaller amplitudes, compared to the experiment. In figure 3.6(b), the overprediction of wiggles with high amplitudes is observed, not only on the advancing side but also on the retreating side. The high Mach number and the high amplitudes lead to the high noise generated in the respective noise carpets. The large amplitudes on the retreating side for **MESIR** are the reason why the noise is widely spread in figure 3.5(b). From $\psi = 270°$ to $\psi = 90°$, the same phenomenon as for the **HARTII** simulation can be seen that there is one big row of oscillations with high amplitudes. Hence, the noise peaks are not isolated and the noise level is overpredicted.

UPM-METAR underpredicts the airloads on the advancing side even more than **METAR** or **MESIR**, seen in figure 3.6(c). Additionally, it shows the same offset like **METAR** at $\psi = 180°$. Hence, this effect seems to be related to the structural model and not the aerodynamic model. On the retreating side, the loads match for a short time the experiment, yet fewer fluctuations and smaller amplitudes are observed, compared to the experiment. This behaviour is also observed in the derivatives, in figure 3.6(d), where **UPM-METAR** underpredicts the number of wiggles compared to the experiment. The lower amplitude in combination with the respective tip Mach numbers lead to the low noise, generated in the noise carpet.

Unlike for the **HARTII** loads, **UPM-BET** matches the experiment well across the whole span for the **7AD**. In addition, it does not capture the same offset like **UPM-METAR**. In figure 3.6(d) the same effect is observed. On the advancing side the amplitudes are lower than the experiment, which lead to the lower noise in figure 3.5(d). The wiggles on the retreating side are directly responsible for the smaller peaks in the noise carpet.

EU underpredicts the airloads by a small amount and determines more fluctuations and smaller amplitudes on both sides, compared to the experiment. The mid near $\psi = 180°$ is captured well. Although **EU** predicts the correct number of oscillations in figure 3.6(f), it also determines the amplitudes too small. The amplitudes for the oscillations on the retreating side also show larger deviations. The lower amplitudes on both sides lead to the lower noise that is generated.

NS underpredicts the airloads nearly across the complete span. The number of oscillations and their amplitudes is calculated too small and near $\psi = 180°$, it shows the largest offset. On the advancing side near $\psi = 90°$ it matches the experiment. In figure 3.6(f), a similar behaviour can be observed. The number and amplitudes of the fluctuations are too small. Therefore, the noise is calculated with large deviation to the experiment.

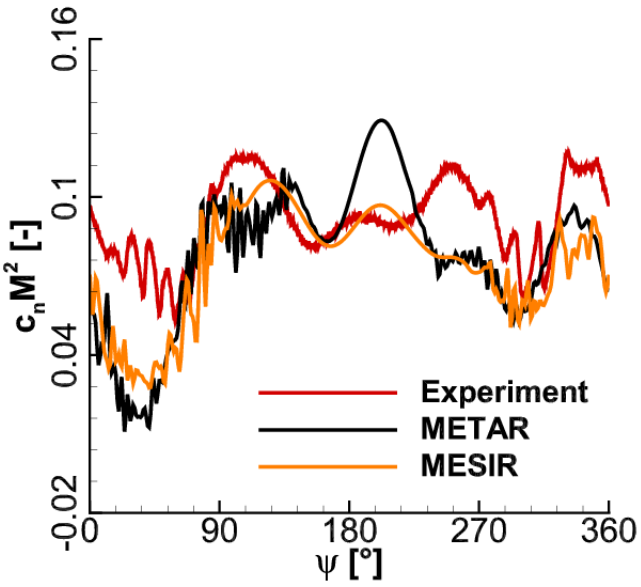

(a) Loads - **HOST**

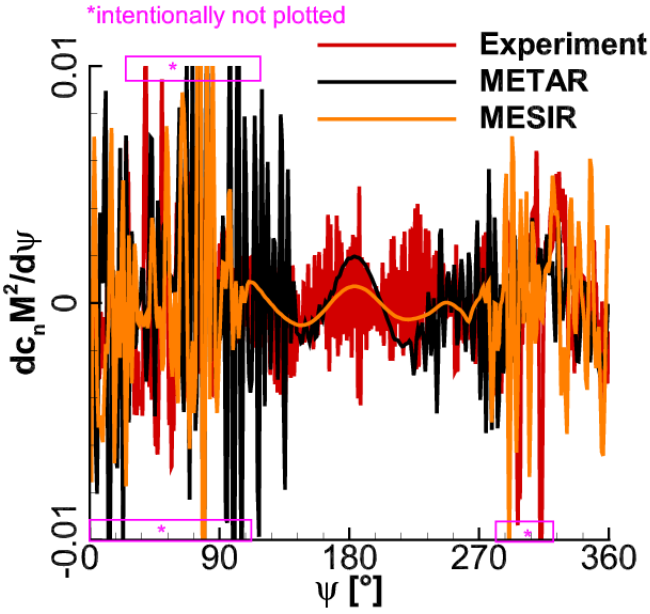

(b) Derivatives - **HOST**

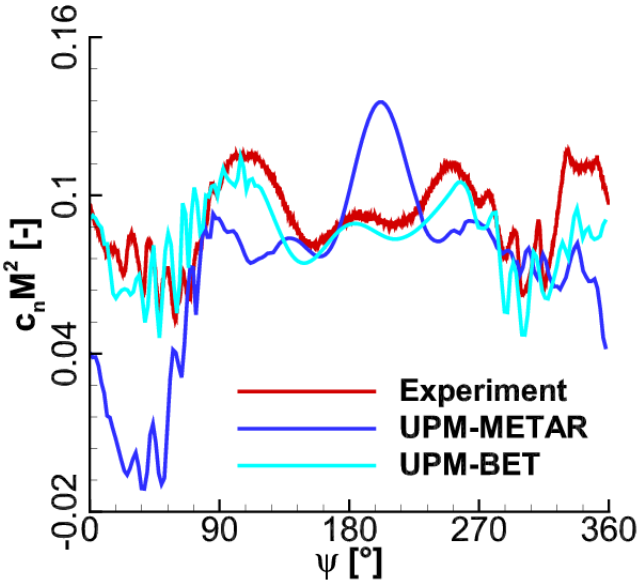

(c) Loads - **UPM**

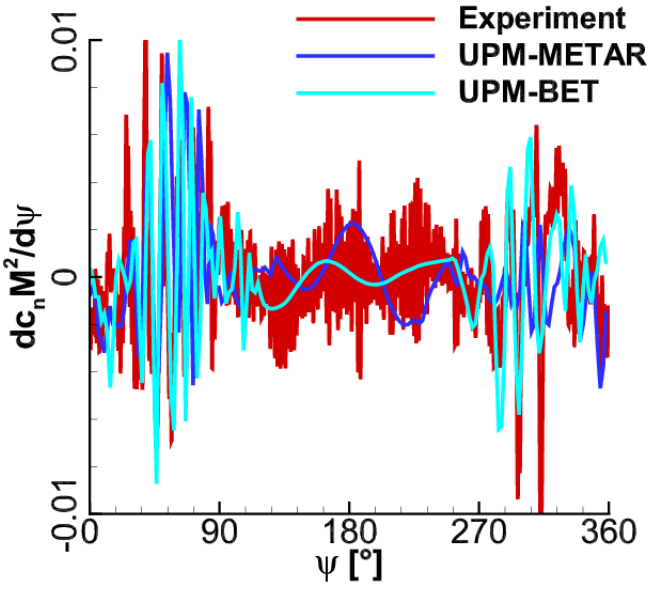

(d) Derivatives - **UPM**

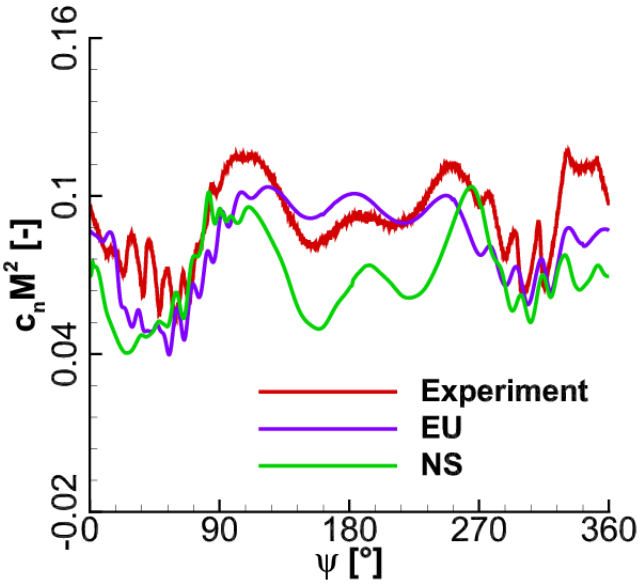

(e) Loads - **FLOWer**

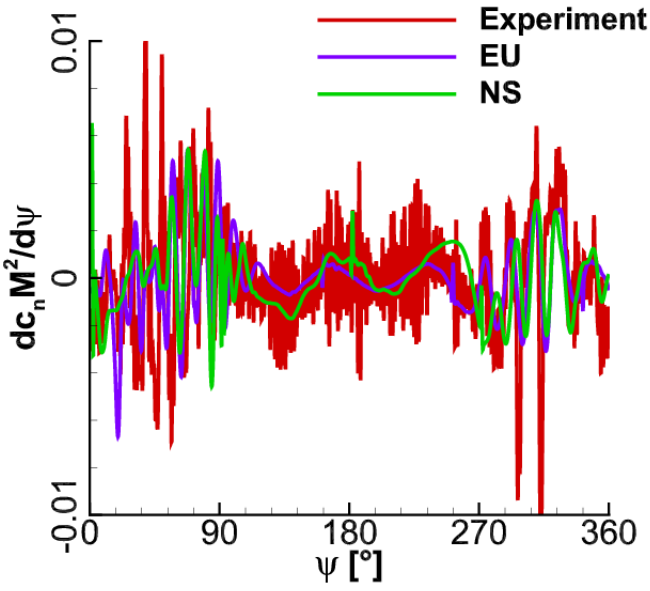

(f) Derivatives - **FLOWer**

Figure 3.6: Loads and derivatives of the **7AD** blade for variable methods at $r/R = 0.825$

3.2.3 ERATO

The **ERATO** blade was the first blade ever developed that has a forward-backward swept tip [10]. It also consists of three different airfoils. It was specifically designed to reduce BVI-noise. The blade design and planform parameters are displayed in figures 3.7(a) and 3.7(c). The noise carpet is presented in figure 3.7(b). In contrast to the other rotors, the **ERATO** only has one large BVI hotspot on the advancing side. In addition, the noise level at the peak is lower than for the other rotors by 2 to 3 dB. Two small peaks are observed at $(x = 1, y = -2)$ and $(x = 0, y = -2)$. The same peaks can be observed for the **7AD** in figure 3.4(b). Yet, the noise level for the **ERATO** peaks is up to 6 dB lower.

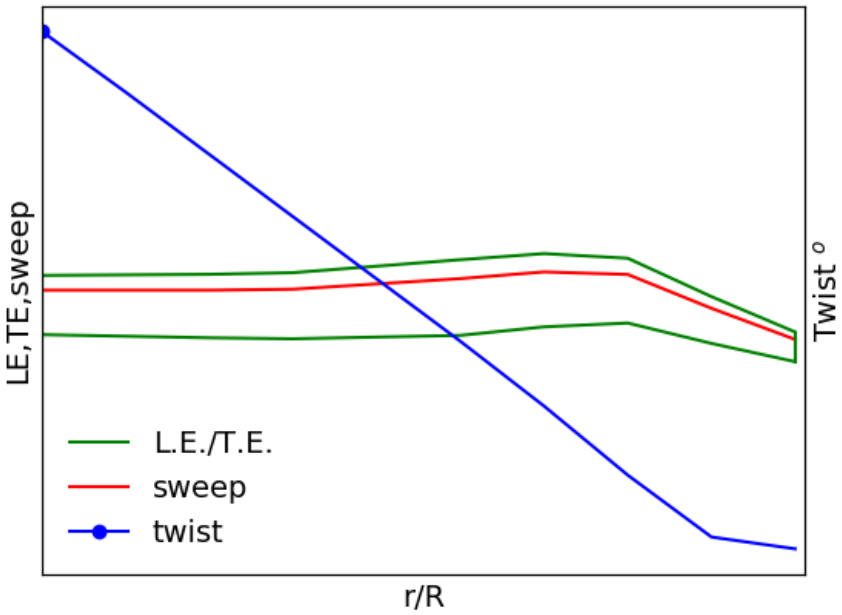

(a) Planform parameters **ERATO**, intentionally without units

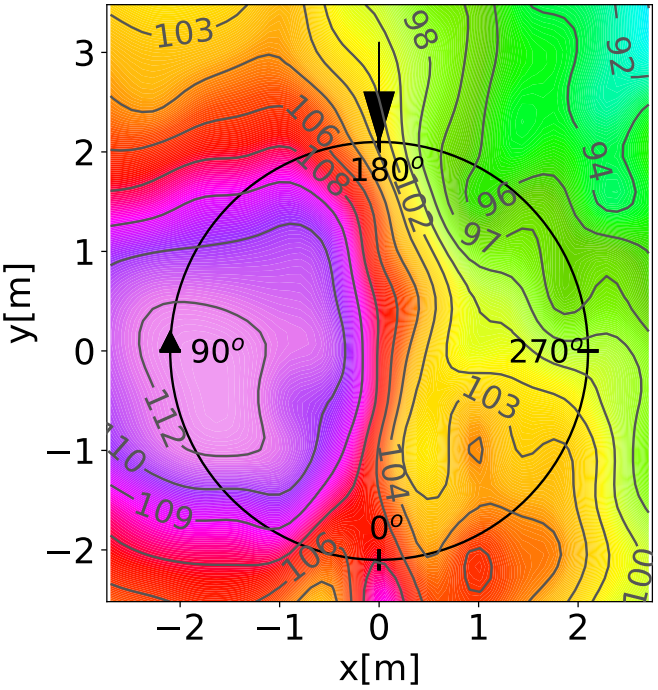

(b) SPL - **ERATO** experiment

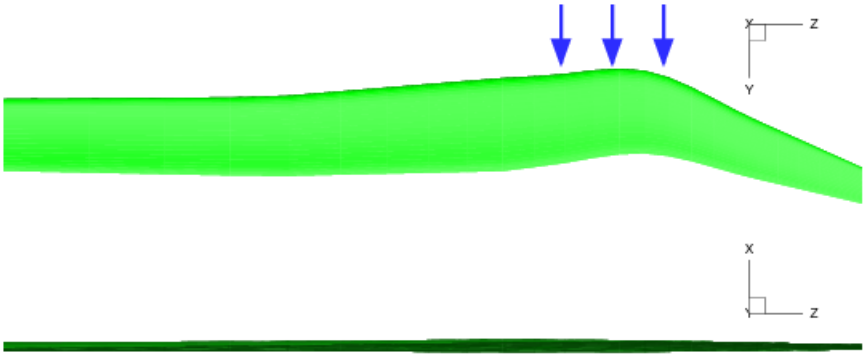

(c) Blade design **ERATO**

Figure 3.7: Planform and SPL $[dB]$ of the **ERATO** experiment

In table 3.5, the trim results from the investigated methods and the experiment are displayed for **ERATO**. In figure A.2(b) in the appendix, an additional diagram for the trim angles is depicted.

METAR shows large differences for all pitch angles. This wrong prediction is one reason for the low noise generation in figure 3.8(a). On the one hand, **METAR** is able to match the location of the peak well just like for the **HARTII**. On the other hand, it is not able to predict the smaller peaks of the rotor blade from the retreating side.

MESIR matches the collective and sine portion pitch better, but underpredicts the cosine portion. In figure 3.8(b), **MESIR** matches the location of the main peak, yet overpredicts the noise level by 2 dB and simulates a second peak at $(x = -1, y = -2)$. This occurs through the false predicted trim angles.

The results from **UPM-METAR** are presented in figure 3.8(c). The noise level exceeds the experiment by 3 dB and the secondary hotspots are not captured at all, yet the center of the peak matches the experiment well.

Compared to the other three methods, **UPM-BET** is able to match the collective pitch, but not the cyclic pitches. Therefore, **UPM-BET** also overpredicts the noise level, displayed in figure 3.8(d). Yet, it is able to simulate one the smaller peaks of the experiment, with a small offset at $(x = 0, y = -2)$.

The **CFD** simulations, **EU** and **NS**, also calculate the cyclic pitches wrong, yet **NS** is able to match the collective pitch well. As already seen for the **HARTII** and **7AD**, the noise generated is too low. This behaviour is seen in figures 3.8(e) and 3.8(f). Additionally, both simulations show a wrong prediction for the location of the hotspot. Yet, they are able to simulate one of the secondary peaks at $(x = 0, y = -2)$.

ERATO			
Methods	$\theta_0[°]$	$\theta_C[°]$	$\theta_S[°]$
Experiment	7.48	2.84	−1.31
METAR	7.90	2.07	−1.68
MESIR	7.72	1.93	−1.33
UPM-METAR	7.90	2.07	−1.68
UPM-BET	7.47	2.11	−0.89
EU	7.33	1.92	−0.84
NS	7.45	2.24	−1.19

Table 3.5: Trim results of the **ERATO** simulations

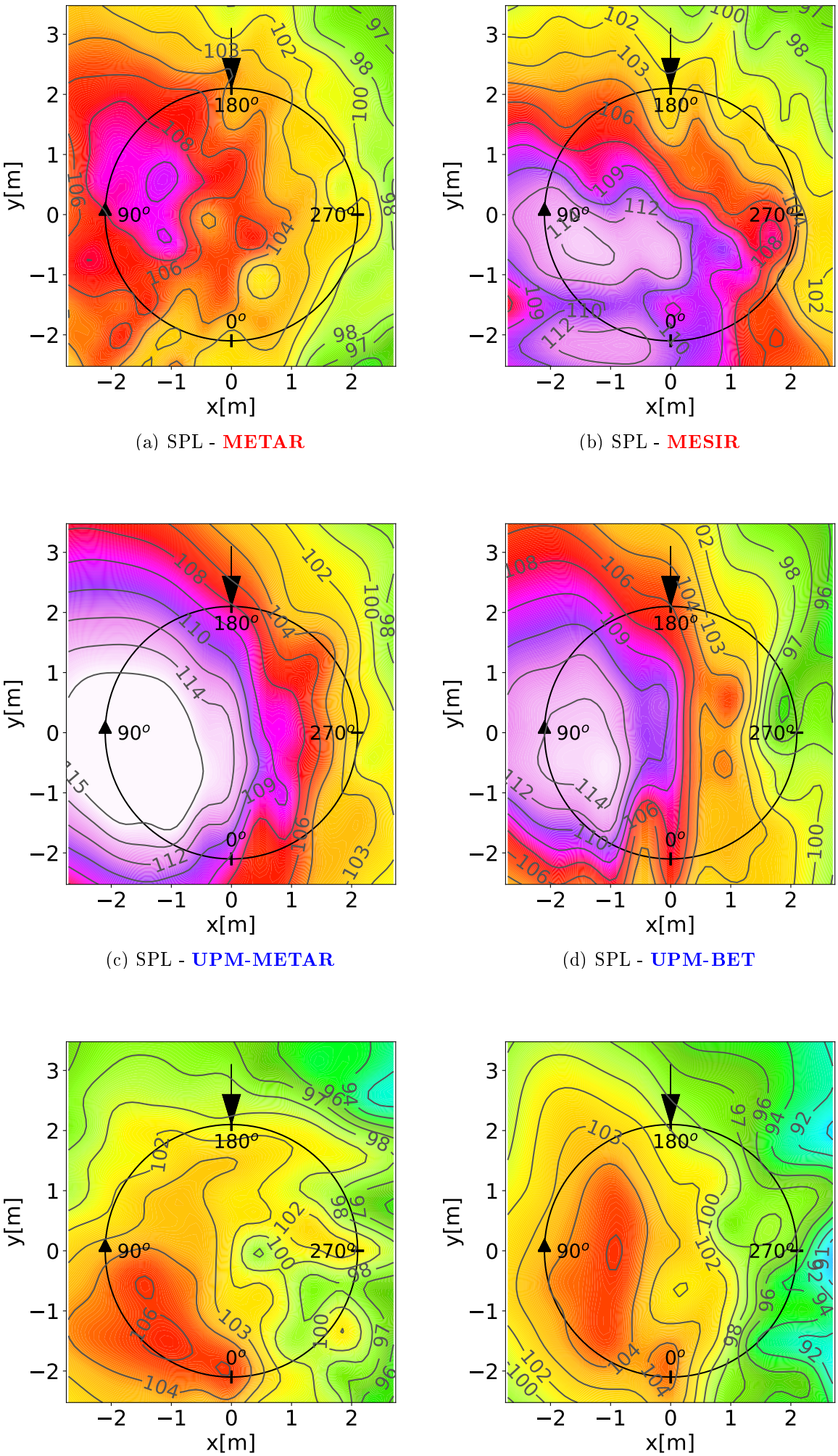

(a) SPL - **METAR**

(b) SPL - **MESIR**

(c) SPL - **UPM-METAR**

(d) SPL - **UPM-BET**

(e) SPL - **EU**

(f) SPL - **NS**

Figure 3.8: SPL [dB] plots for the **ERATO** blade

In figure 3.9, the airloads and their temporal derivatives for the **ERATO** blade are presented. The location of the radial cut is at $r/R = 0.85$ of the blade geometry.

In figure 3.9(a), **METAR** shows a good representation of the experiment, although it underpredicts the loads on the advancing side of the blade and small offsets at the front and retreating side of the blade. Like the blades before, **METAR** simulates the wiggles too far behind the main peaks of the experiment, seen in figure 3.9(b). The retreating side is well captured, except some fluctuations occurring too early. The lower tip Mach number on the advancing side and the later occurring oscillations are the reason why there is an offset in location and noise level in the carpet plot.

MESIR matches the experiment well with a small offset. One difference between **METAR** and **MESIR** is near the front of the rotor at $\psi = 180°$, where **MESIR** is able to simulate the small rise in airloads. Another difference between the methods is the number of fluctuations along the curve, where **MESIR** shows less wiggles with higher amplitudes. In addition, **MESIR** predicts one high amplitude offset near $\psi = 0°$. As seen in figure 3.8(b), the noise generated, is too high compared to the experiment. This rise in noise is also observed in figure 3.9(b), where larger amplitudes than the experiment are observed. The location of the fluctuations is determined correctly for the retreating side, yet the amplitudes are predicted too high. As already seen for the other blades, from $\psi = 270°$ to $\psi = 90°$ an oscillation with high frequency and amplitude is observed. Hence, two peaks are predicted at $(x = -2, y = 0)$ and $(x = -2, y = 1)$.

In figure 3.9(c), the airloads of **UPM-METAR** are displayed. The advancing side is captured well, but the front does not match and the retreating side is overpredicted. Although the number of fluctuations on the retreating sidfe matches the experiment, they occur later and smaller amplitudes are generated. In figure 3.9(d), the temporal derivatives are identified. Most of the fluctuations are predicted correctly in terms of location, but the amplitude is too small and one oscillation occurs at $\psi = 0°$. Through this first wiggle and the following, the pressure increases on the blades and thus the noise level increases, seen in the noise carpet in figure 3.8(c).

UPM-BET underpredicts the airloads on the advancing side and shows a big offset at the front side. On the retreating side, it overpredicts the loads, yet overall it shows the same amount of oscillations like the experiment. The derivatives, in figure 3.9(d), show a close match with the experiment on the advancing side. Like **UPM-METAR**, it predicts the fluctuations on the retreating side well with one large offset near $\psi = 360°$. On the retreating side more oscillations than the experiment occur with smaller amplitudes, hence the noise level in that area the same as the experiment.

Both, **EU** and **NS**, show fluctuations with small amplitudes, seen in figure 3.9(e). The contour of the curves of both methods match the experiment, however the loads are generated too low. On the advancing side at $\psi = 100°$ and on the retreating side at $\psi = 300°$ they match the experiment with small offsets. In figure 3.9(f), both simulations show a similar behaviour on the advancing and retreating side. The number and location of oscillations is captured well, but the amplitudes are predicted too low. The small amplitudes are the reason why the noise is lower than the experiment. The single wiggle from **EU** near $\psi = 0°$ is accountable for the wrong location of the peaks location in figure 3.8(e).

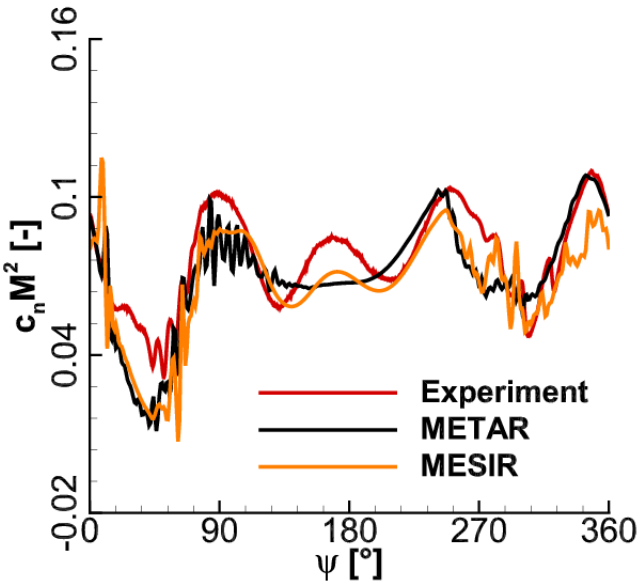

(a) Loads - **HOST**

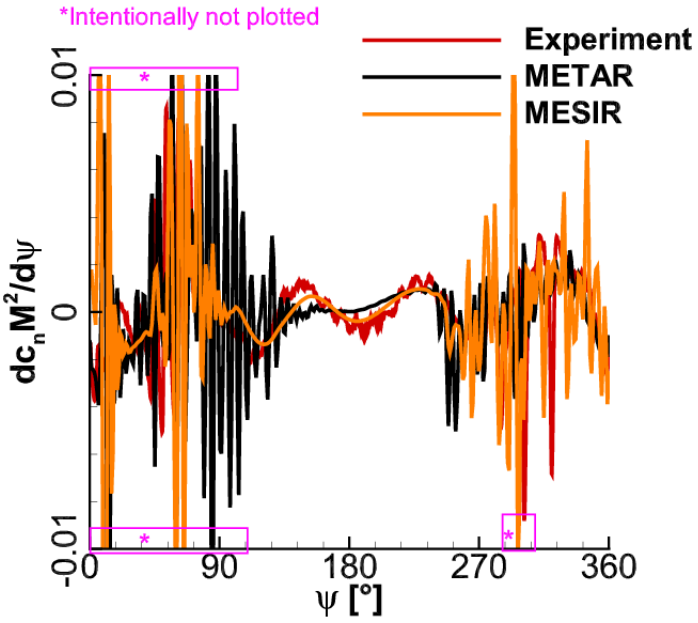

(b) Derivatives - **HOST**

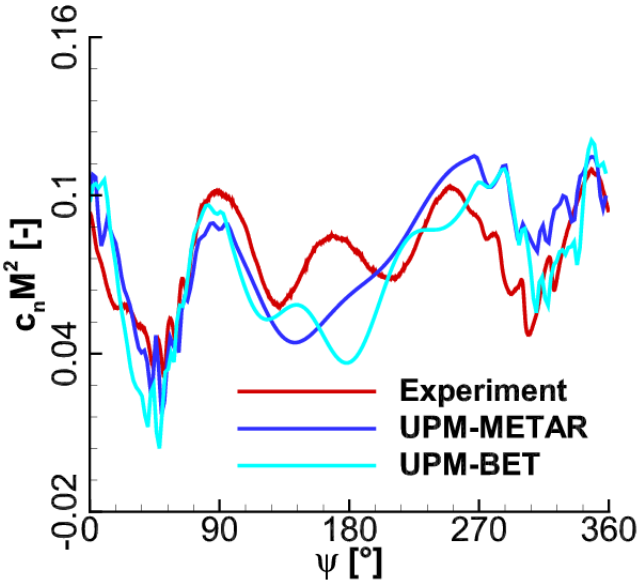

(c) Loads - **UPM**

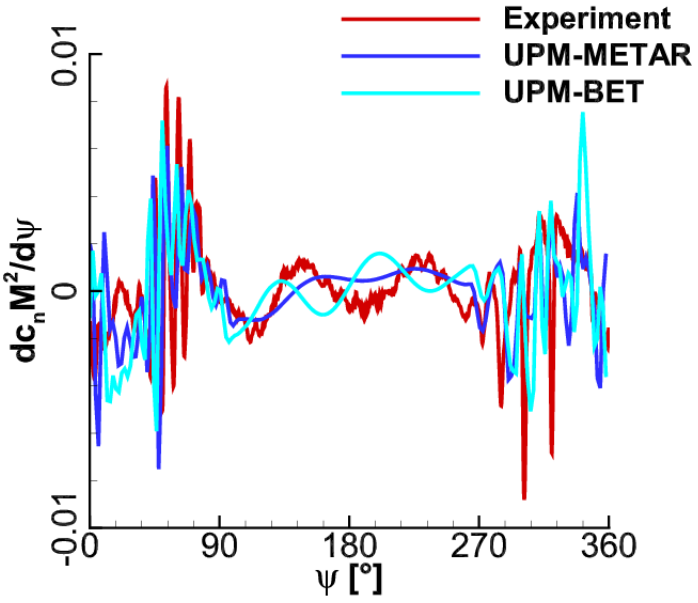

(d) Derivatives - **UPM**

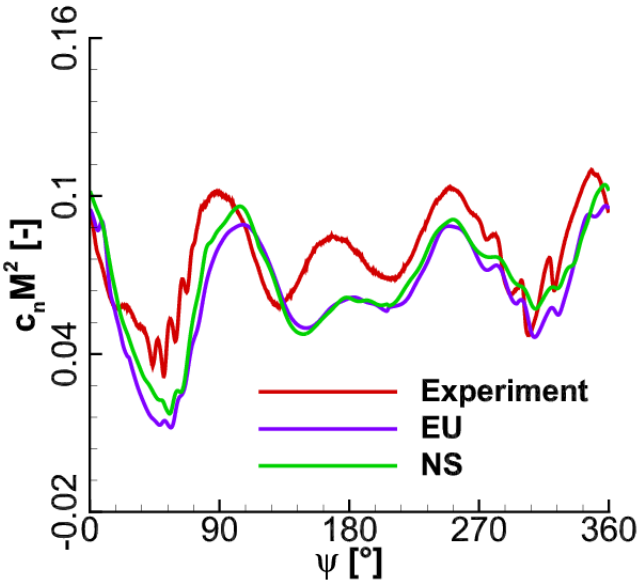

(e) Loads - **FLOWer**

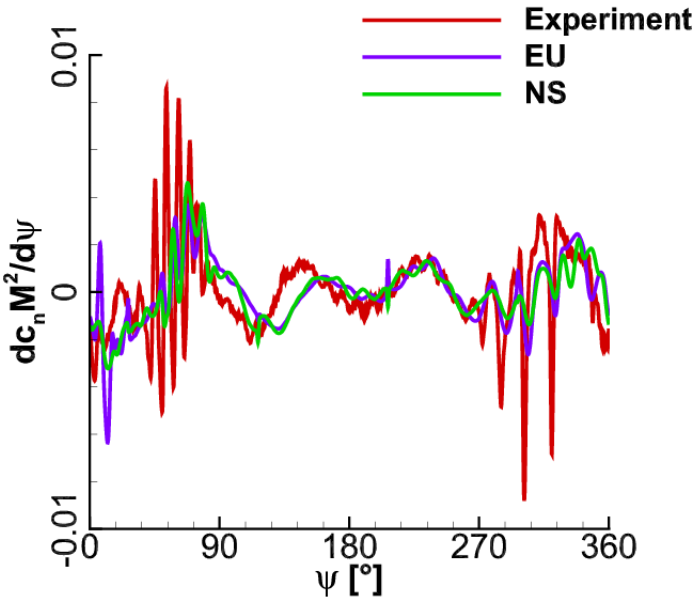

(f) Derivatives - **FLOWer**

Figure 3.9: Loads and derivatives of the **ERATO** blade for variable methods at $r/R = 0.85$

3.3 Review of the Accuracy and Costs for Variable Fidelity Methods

To perform a parameterization and optimization with variable fidelity methods, it is also important to take the required computational resources into account. In figure 3.10, the average amount of time, required for the different methods, is displayed. The time axis is presented in computer hours on a logarithmic scale. The simulation conducted with **NS** is considered as the high fidelity one based on earlier simulations with **CFD** [27]. Therefore, it is seen as a reference and the others are compared with it via a percentage of time needed for them. As already mentioned, **CFD** takes most of the time. The difference between **CFD** and the free wake models are more than two orders of magnitude. Although **EU** is considered mid-high fidelity it takes even more time than the **NS**. The reason is that **EU** needs more iterations to trim the rotor than **NS**.

Although the amount of time for the free wake models **MESIR** and **UPM** is very close, the noise carpets show large differences. Reasons for this behaviour is the neglection of the fuselage and the representation of the rotor as a line for **METAR** and **MESIR**. **UPM** works with panels and thus represents the surface of the blade. Thus, it is more suited to capture the tip vortices and their interactions. The time needed for **CFD** simulations is very high and they do not represent the experiments well enough with the given resolution. Although the number of grid cells could be increased to capture the specific elements, the required computational resources would increase even more.

In table 3.6, the results of the methods of each blade are compared in terms of the respective noise carpets. Important aspects for comparison are the matching of number, isolation and location of hotspots. The capturing of the noise level is an additional aspect. **METAR** predicts coarse representations of the experiments and is not able to capture specific characteristics like second peaks or the noise level as the experiment. **MESIR** shows the largest offsets compared to the experiments. Only for the **HARTII** blade, it is able to give a fair representation.

It seems that the results from **UPM-METAR** are dependent on the blade model. For the **HARTII** blade, it produces the best results of all methods and the carpets of the **7AD** and **ERATO** are coarse presentations of the experiments. **UPM-BET** produces results with at least two characteristics for the investigated blades.

Both **CFD** methods make well predictions for the **HARTII** blade, but not for the other two blades.

The conclusion of figure 3.10 and table 3.6 is that **CFD** simulations are not suitable for parameterizations over large parameter spaces, as mentioned before and by Kowarsch et al [12]. In contrast, **METAR** is very well suited to do first investigations on planform parameters to get an impression what changes affect the emitted noise and if specific changes are even possible. **MESIR** is not suitable, because of the relatively large amount of time it requires. Both **UPM** combinations can be used to perform a parametric study on planform parameters. **CFD** may be used to confirm the output from the mid-fidelity methods. This however is only possible if the number of grid cells is increased and the stepsize is reduced.

Considering the results, the parametric study is performed with both methods from **HOST** and **UPM** respectively.

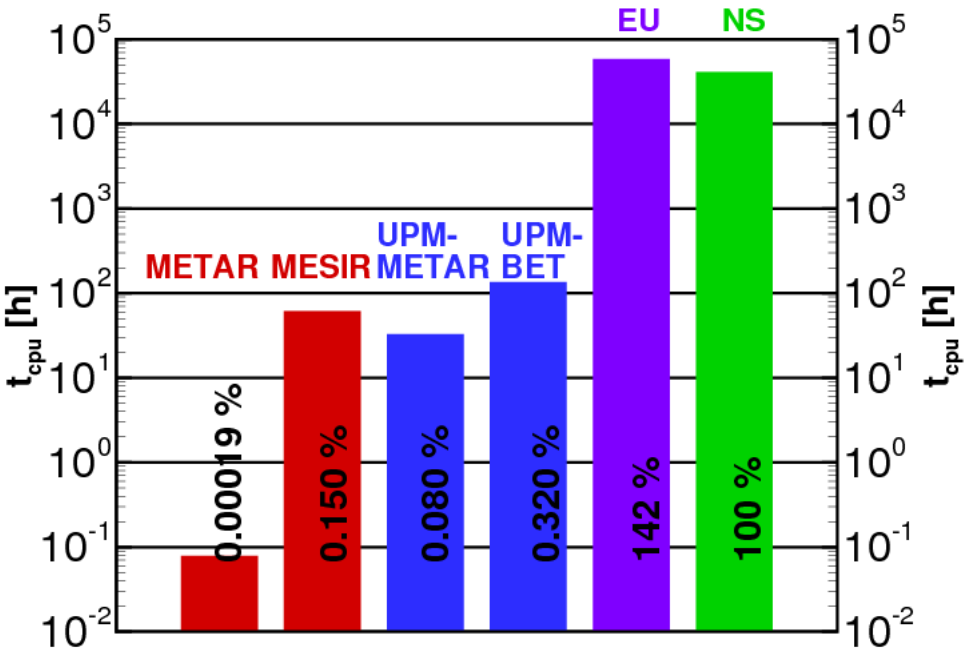

Figure 3.10: Average logarithmic scaled time needed for different methods in computational hours

Methods	HARTII	7AD	ERATO
METAR	⊙	⊖	⊙
MESIR	⊙	⊖	⊖
UPM-METAR	⊕⊕	⊙	⊕
UPM-BET	⊕	⊕	⊕
EU	⊕	⊙	⊙
NS	⊕	⊙	⊙

Table 3.6: Comparison of noise carpets of all rotor blades and all methods, requirements are: number, location and isolation of hotspots and noise level, legend: ⊖ - none is fulfilled, ⊙- one is fulfilled, ⊕- two are fulfilled, ⊕⊕- three are fulfilled

Chapter 4

Results of the Parametric Study

In the following chapter, the setup and the results of the parametric study are presented and analyzed. The results of the most promising rotors are displayed as before, via noise carpets, airloads and temporal derivatives. Furthermore, there are landscapes plots given, which are used to identify the best case for each parameter and the planform of the blade for the respective method. In addition, wake visualizations for **UPM-BET** are displayed in the appendix in figure A.13 for all parameters and the **7AD** baseline cases, to identify how the emitted vortices are affected.

4.1 Baseline of the 7AD Rotor Blade with reduced RPM

The baseline rotor is chosen to be the **7AD** blade. Additionally, the RPM is reduced to the same number as for the **ERATO** blade: 946 [36]. Due to the lower RPM the tip speed is decreased, thus the emitted noise is decreased by 2 dB in the maximum A-weighted SPL [36]. The flight condition is the same as for the **ERATO** blade, see table 3.2.

In figure 4.1, the noise carpets of the individual methods for the **7AD** with reduced RPM are depicted. In the appendix, in figure A.3, their difference noise plots are displayed, to identify how each method predicts the noise compared to the **7AD** case presented in chapter 3.

METAR, displayed in figure 4.1(a), predicts one hotspot at $\psi = 90°$ with a noise reduction of 4 to 6 dB. At $\psi = 0°$, it seems that there is one more hotspot predicted that may be the second peak generated by BVI. Compared to the **7AD** baseline, in figure 3.5(a), the overall noise level and the spread are reduced.

Although **MESIR**, presented in figure 4.1(b), shows no reduction in the maximum occurring SPL, it predicts one main hotspot. In the lower right corner more noise compared to its baseline case is generated. Near $(x = 0, y = -2)$, it may be possible that the second peak of BVI may be observed. Unlike **METAR**, **MESIR** still predicts a large area of high noise.

The noise carpet of **UPM-METAR**, in figure 4.1(c), predicts a reduction in noise near $\psi = 90°$ up to 3 dB. From $\psi = 270°$ to $\psi = 45°$, more noise compared to its baseline case is generated. At $(x = 1, y = -2)$, the second hotspot of BVI can be observed.

The noise carpet of **UPM-BET**, depicted in figure 4.1(d), predicts a similar noise carpet as its baseline case, in figure 3.5(d). The noise level in the peak has not been decreased. Small changes are identified around $\psi = 0°$, where three smaller peaks are predicted. Comparing the wakes in figures A.13(a) and A.13(b), the vortices are set off above the rotor disc by small amounts. Hence, the interactions between blades and vortices have been reduced.

Although the simulations differ from each other, the simulations performed with **HOST** show

either a reduction in the overall noise level or in the peaks. The simulations performed with **UPM** show no significant reduction in noise level, but an increased noise level in different areas. **UPM-BET** was not able to reach the noise level of the **7AD** blade from chapter 3.2.2. Hence, it may be possible that this simulation is a good representation of the **7AD** with reduced RPM, with the 2 dB noise reduction [36].

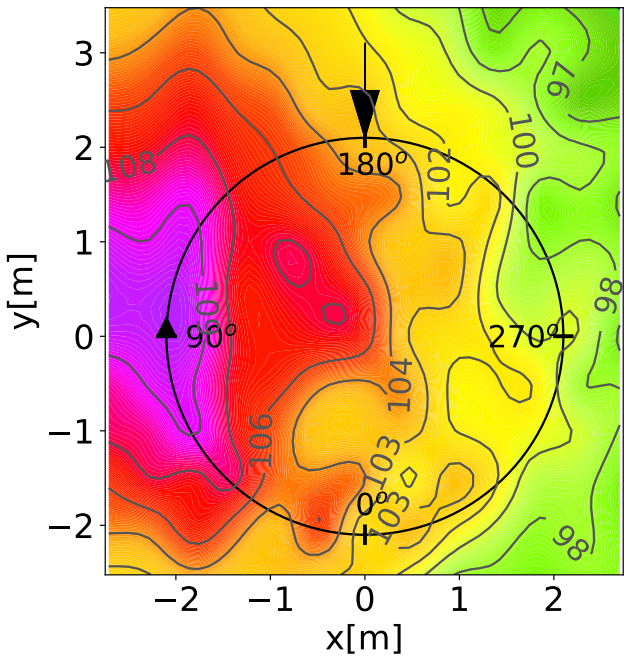

(a) SPL - **METAR**

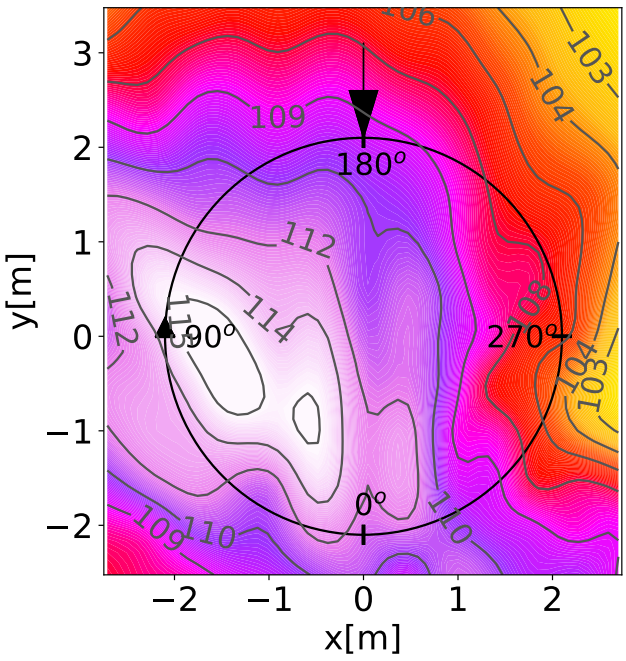

(b) SPL - **MESIR**

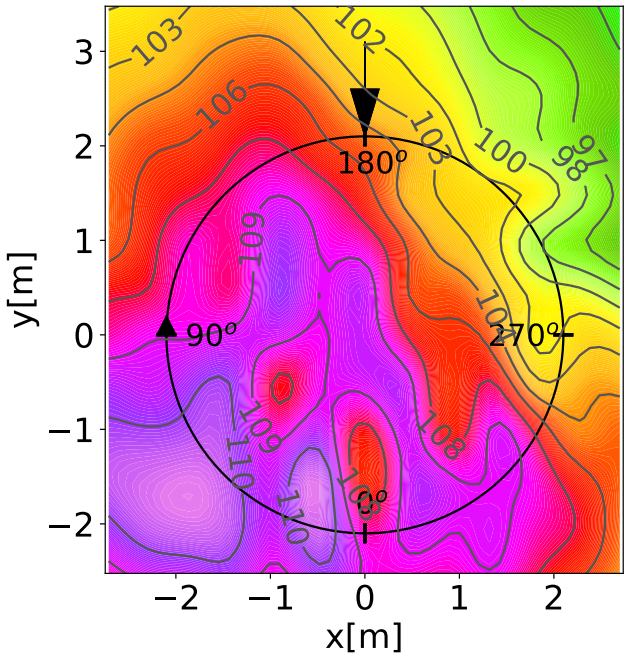

(c) SPL - **UPM-METAR**

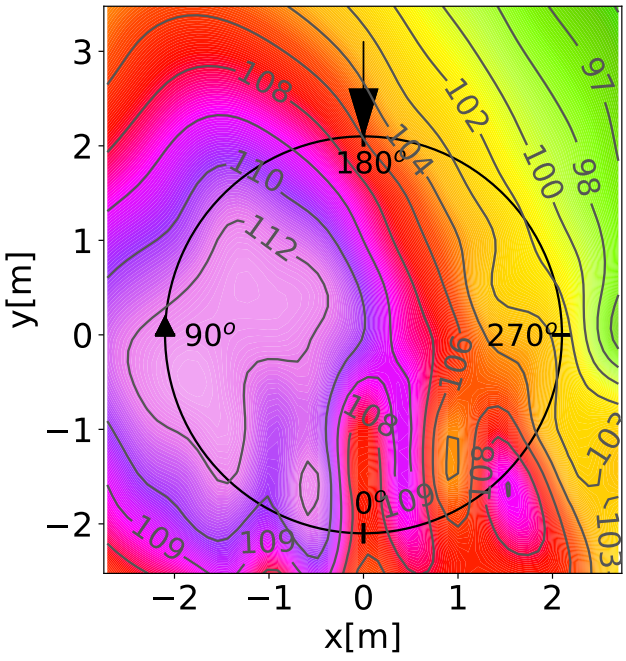

(d) SPL . **UPM-BET**

Figure 4.1: 7AD with reduced RPM - SPL [dB] of the different methods

In figure 4.2, the loads and temporal derivatives of the used methods are presented. Unlike before they are displayed as disc plots to show the airloads over the whole rotor plane. The legends for the plots are displayed above. The unit N/m stands for a line load across the rotor blade and is equivalent to lift. The unit N/m° stands for the temporal derivative of the line load derived with the time equivalent degrees. The red lines symbolize the area where most thrust is generated. The difference plots for the airloads are depicted in the appendix in figure A.4

The airloads generated by **METAR** are displayed in figure 4.2(a) and predict oscillations on the advancing side of the blade from $\psi = 45°$ to $\psi = 135°$. Peaks are observed near $\psi = 200°$, $\psi = 270°$ and $\psi = 330°$. In figure 4.2(b), the derivatives are depicted. Oscillations with large amplitudes are identified on the advancing side of the blade between $\psi = 0°$ and $\psi = 135°$. The wiggles between $\psi = 45°$ and $\psi = 100\circ$ are responsible for the noise level in the hotspot and the oscillations near $\psi = 0°$ are accountable for the noise artefact in the noise carpet near $(x = 0, y = -2)$.

In figure 4.2(c), the loads predicted by **MESIR** show peaks at $\psi = 0°$, $\psi = 100°$ and $\psi = 270°$. Between these peaks on the advancing and retreating side of the blade between $\psi = 270°$ and $\psi = 90°$, oscillations are observed. These wiggles are better captured in figure 4.2(d). Due to the high amplitudes on the advancing side, the noise level is still very high. The wiggles on the retreating side are the second hotspot of BVI. Due to the continuous fluctuation and the directivity of the sound, it seems no second hotspot is generated, but a large carpet with high amount of noise.

The airload peaks in figure 4.2(e), for **UPM-METAR**, are predicted mainly on the retreating side of the blade at $\psi = 270°$ and $\psi = 330°$. Between the peaks, near $\psi = 300°$, oscillations are identified. On the advancing side even more oscillations are observed. These fluctuations at $\psi = 45°$ can also be observed in figure 4.2(f). The wiggles are focused around three distinct locations: $\psi = 315°$, $\psi = 0°$, $\psi = 45°$. These fluctuations are accountable for the noise peaks in figure 4.1(c).

The airloads of **UPM-BET**, displayed in figure 4.2(g), show no peaks as the simulations before. On the advancing and retreating side wiggles are identified, yet no high amount of load. The contour of **UPM-BET** is close to **UPM-METAR**, yet less loads are generated. Comparing the derivatives of both **UPM** simulations, it can be observed that **UPM-BET** predicts the same amount of fluctuations, yet with higher amplitudes on the advancing side at $\psi = 45°$ and $\psi = 0°$. Hence the noise level is higher. The wiggles on the retreating side are smaller, thus a distinct second and third peak can be identified.

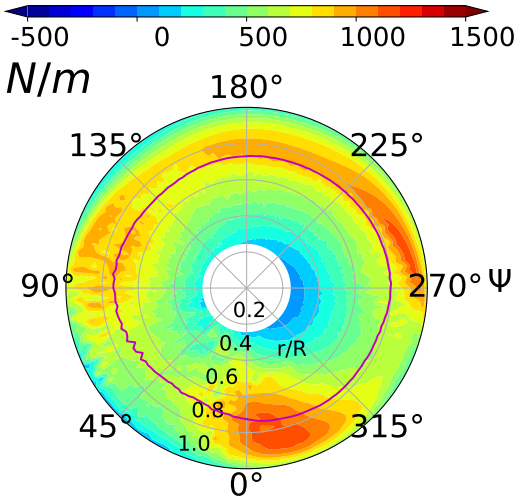

(a) Loads - **METAR**

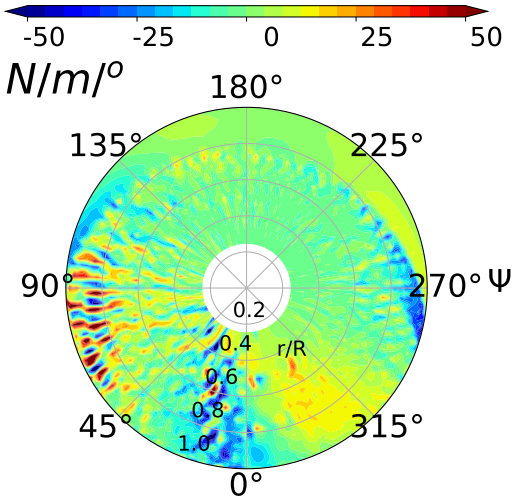

(b) Derivatives - **METAR**

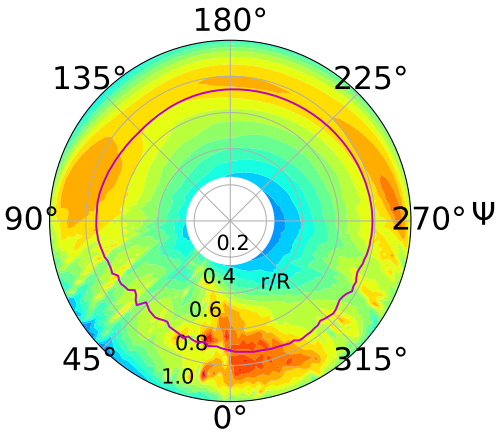

(c) Loads - **MESIR**

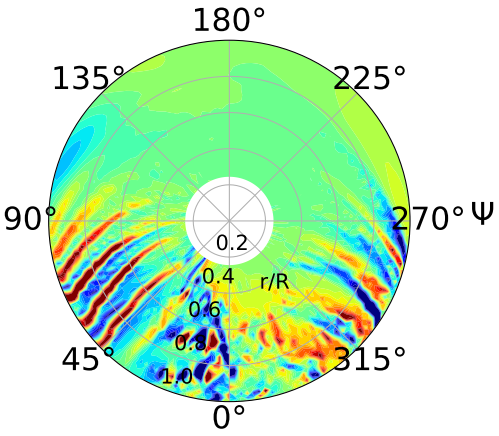

(d) Derivatives - **MESIR**

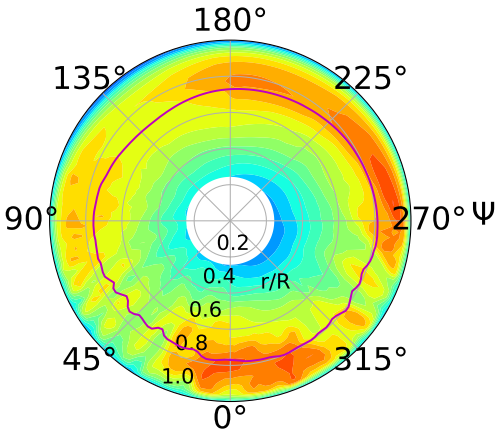

(e) Loads - **UPM-METAR**

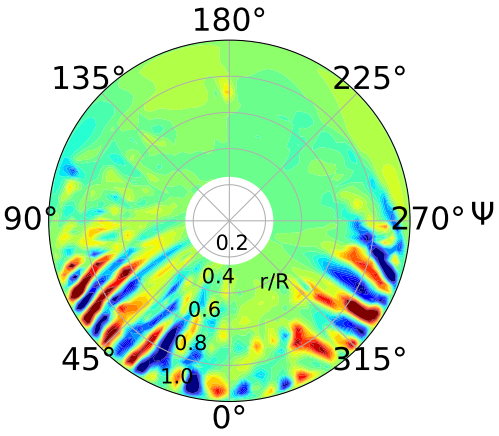

(f) Derivatives - **UPM-METAR**

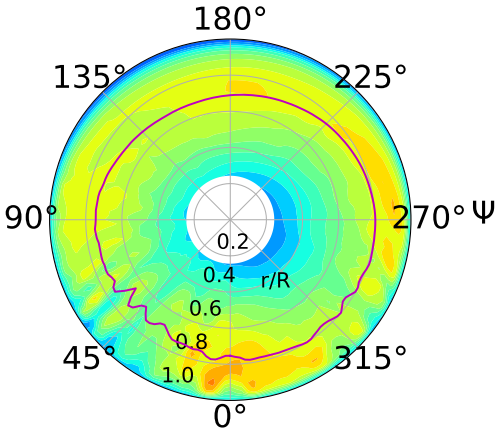

(g) Loads - **UPM-BET**

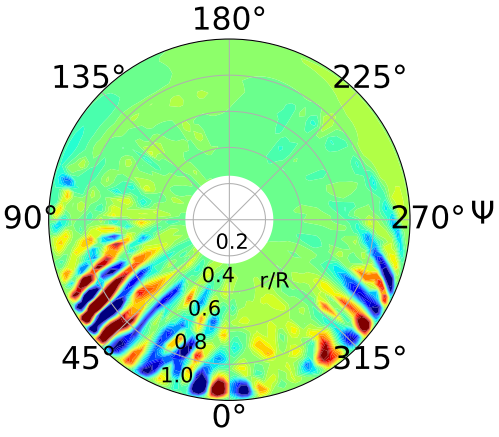

(h) Derivatives - **UPM-BET**

Figure 4.2: 7AD with reduced RPM - Loads and derivatives of the different methods

4.2 Test Setup of the Parameterization

In figure 4.3, the baseline parameters of the **7AD** are shown over the normed radius. The chord length at the tip of the blade is fixed. The location, where the change in chord length takes place is marked and will be varied. The location of anhedral is fixed at the blade tip, yet its point of change will be varied. The amount and the location of sweep-1 and twist-1 will be changed. Sweep-2 and twist-2 are fixed by position, yet their amount will be varied.

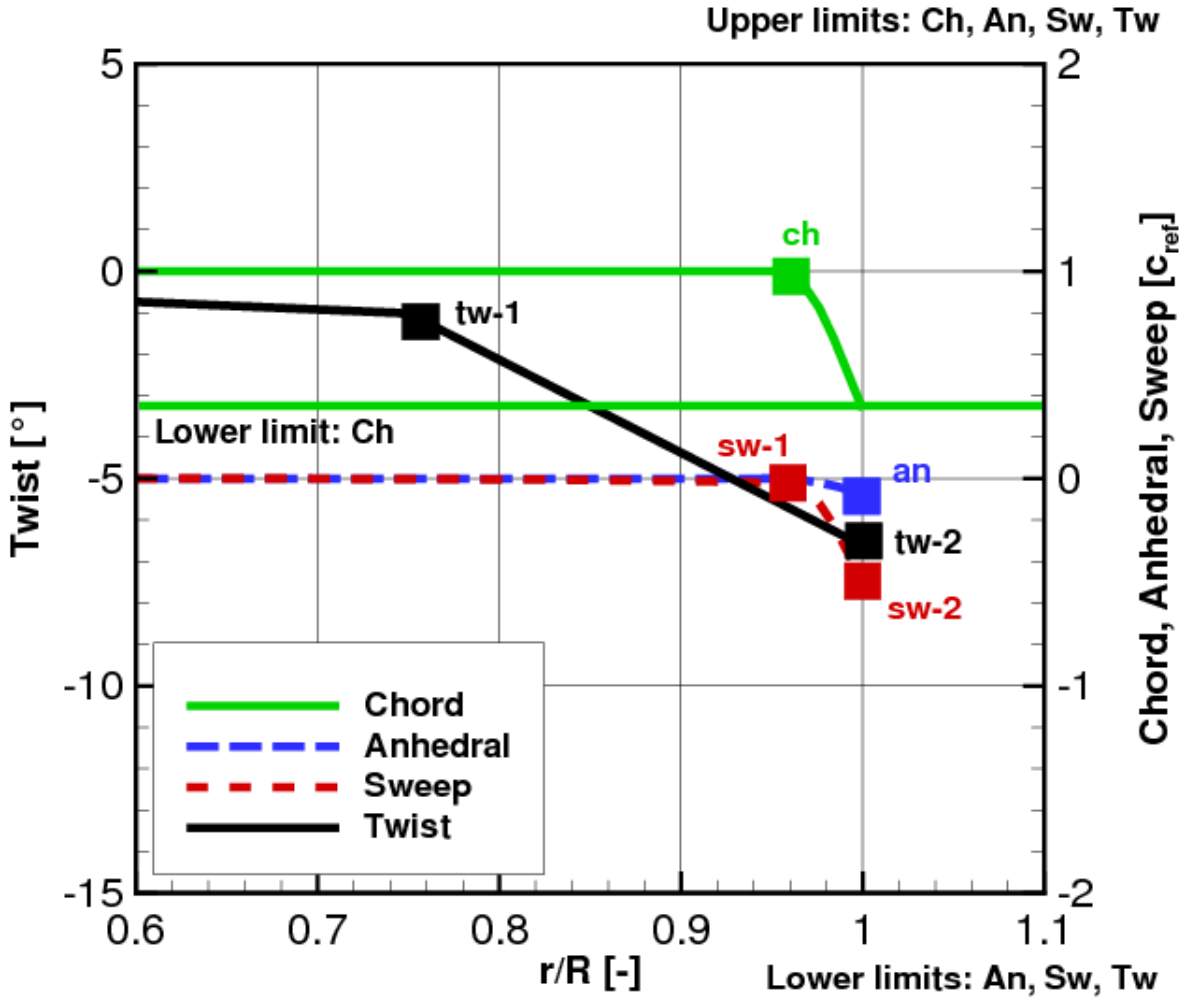

Figure 4.3: Definition of the **7AD** baseline rotor and control points for planform parameters

In table 4.1, the parameters for the baseline at the different locations and the ranges for the parametric study are depicted. The ranges have been set relatively large, so that the effect of each change, be it big or small, can be analyzed. The Ogee tip, mentioned by Brocklehurst and Barakos [11], has a small chord length at the tip, hence the chord length is modified over a large blade span. The effect of anhedral can be seen on airplanes, thus the effect of a winglet should be tried. Two sweep settings are taken to possibly derive the **ERATO** or BlueEdge^{TM} blade [36]. These blades did show that double sweep has a positive effect on the emitted noise. Twist has a great impact on performance, yet if twist is able to reduce noise effectively has to be investigated.

	7AD		Parameterization			
Parameters	Reference	r/R	Lower Bound	Upper Bound	$(r/R)_{min}$	$(r/R)_{max}$
Chord length	0.33	0.93	0.33	2.0	0.6	1.0
Anhedral	−0.07	0.95	−2.0	2.0	0.6	1.0
Sweep-1	0.06	0.97	−2.0	2.0	0.6	1.0
Sweep-2	0.50	1.0	−2.0	2.0	1.0	-
Twist-1	−2.6	0.75	−15.0	5.0	0.6	1.0
Twist-2	−8.2	1.0	−15.0	5.0	1.0	-

Table 4.1: 7AD baseline, minimum and maximum parameters with respective locations along the blade

In table 4.2, the grid sizes for the methods and parameters are displayed. It is a full factorial grid, which means that the displayed number is taken by the power of numbers of parameters. A parameterization with **METAR** on chord variation, for example, investigates 100 different blade shapes, because difference chord lengths and their locations along the blade are simulated. Because of the long time that is required for **MESIR**,**UPM-METAR** and **UPM-BET**, the number of simulations is lower. The amount of simulations for each direction for sweep and twist is smaller, because the number of simulations increases even more with more directions.

Parameters^{directions}	**METAR**	**MESIR**	**UPM-METAR**	**UPM-BET**
Chord^2	10(100)	7(49)	7(49)	5(25)
Anhedral^2	10(100)	7(49)	7(49)	5(25)
Sweep^3	5(125)	4(64)	4(64)	3(27)
Twist^3	5(125)	4(64)	4(64)	3(27)

Table 4.2: Full factorial for different methods and parameters

4.3 Analysis of Parametric Results on Aeroacoustics with Variable Fidelity Methods

In the following section, the characteristics of the planform parameters with the used methods are discussed. For the analysis, each parameter is presented individually with each method. Landscapes of maximum noise are used to identify the effect each parameter has on the emitted noise. Surrogate models are used to interpolate the space between the configurations. The blacked out areas mark invalid rotor design that could not be trimmed. The blue and dark blue areas stand for the minimum amount of noise reached in the different simulations. The purple dots represent all the configurations. The magenta diamond represents the best configuration for the respective method. The baselines of the **7AD** with reduced RPM, in figure 4.1, represent the reference with 1.0 for the respective methods. Everything below 1.0 is a decrease and everything above 1.0 is an increase in emitted noise. Furthermore delta-noise carpets, delta-airloads, temporal derivatives of airloads and the blade planforms of the best simulations are presented. The term best is referred to the minimal occurring SPL peak. The distribution for the color is for all plots the same.

4.3.1 Chord Length

Behaviour of Simulations and Identifying the best Designs

In figure 4.4, the results of the chord parameterization with the four used methods are displayed. The respective best designs are depicted below.

In figure 4.4(a), the results for **METAR** are given. First, it is mentionable that most of the simulations with a reference chord length of more than 1.5 did fail. Secondly, most of the simulations below a chord length of 1.5 were successful. These simulations show that a decrease in chord length also reduces the emitted noise, especially a short chord length closer to the blade root at $r/R = 0.64$ is reducing the noise by about 3%.

MESIR, displayed in figure 4.4(b), shows a similar behaviour like **METAR**. Larger chord lengths increase the emitted noise and are too unstable to be simulated. Smaller ones reduce the noise and are successful. Both **HOST**-based methods also predict a similar blade planform as their optimum.

UPM-METAR, depicted in figure 4.4(e), also predicts failed simulations with a chord length over 1.5. The behaviour is like the one seen for **METAR**, because both use the same trim as their basis. If **METAR** fails to trim a blade design, **UPM-METAR** will fail too, yet the configurations of these methods must not be the same because of the number of simulations for each direction. The best planform is predicted at $r/R = 0.73$ and a chord length of 0.61 at that location.

UPM-BET is unable to simulate blades with a small chord length beginning closer to the root of the blade. Unlike the other methods, it is able to simulate larger planforms with an increase in noise of 3%. Although the behaviour is alike the others, the best planform is found at $r/R = 0.9$ with a chord length of 0.33.

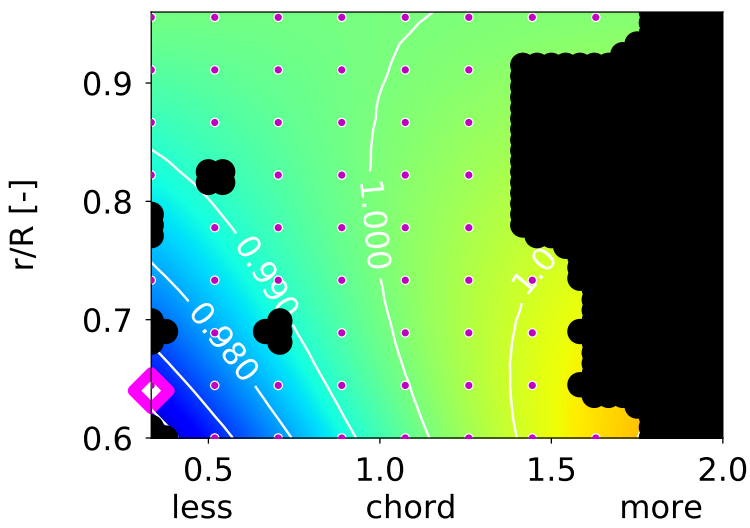

(a) **METAR**

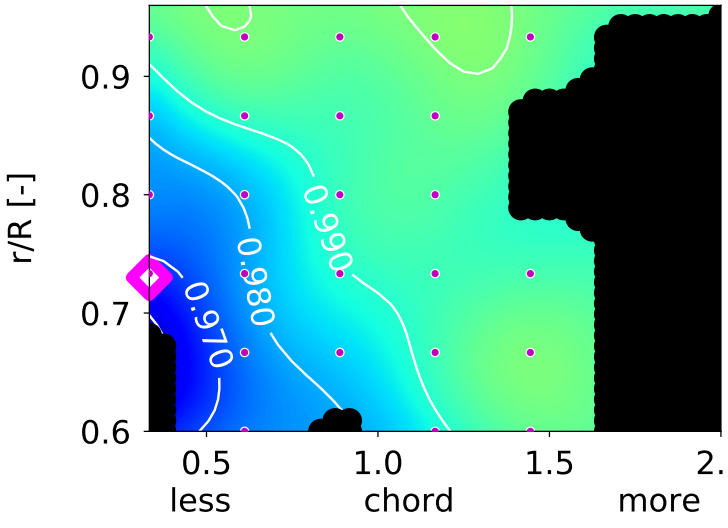

(b) **MESIR**

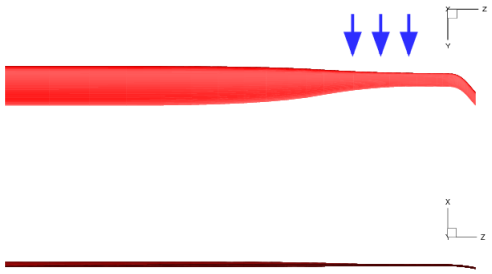

(c) **METAR** - blade design

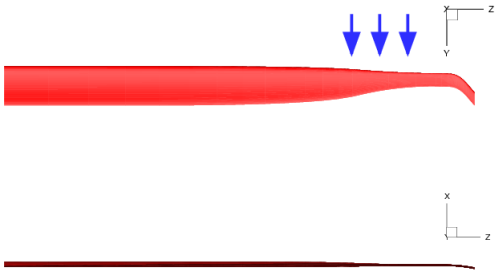

(d) **MESIR** - blade design

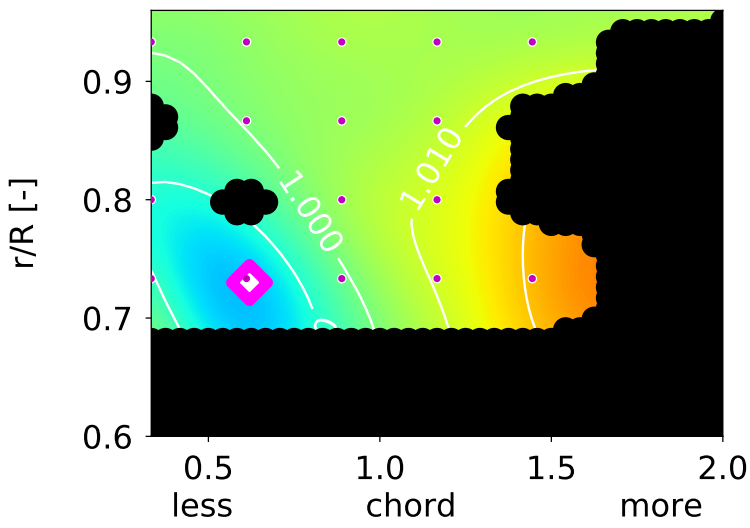

(e) **UPM-METAR**

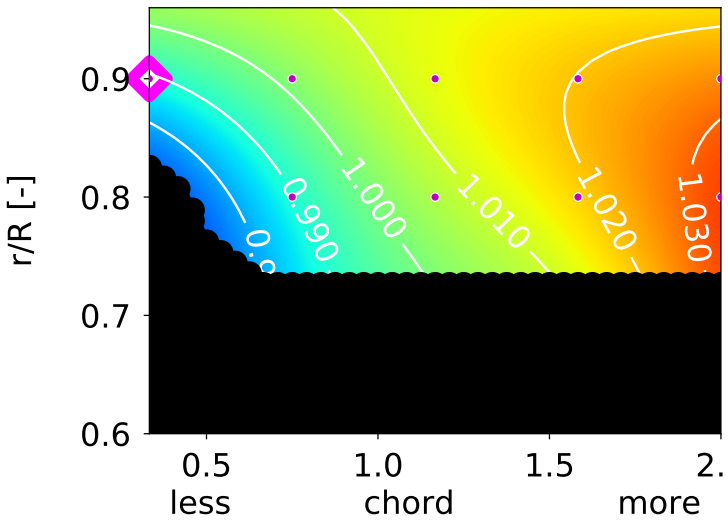

(f) **UPM-BET**

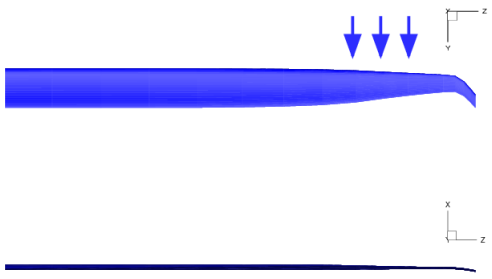

(g) **UPM-METAR** - blade design

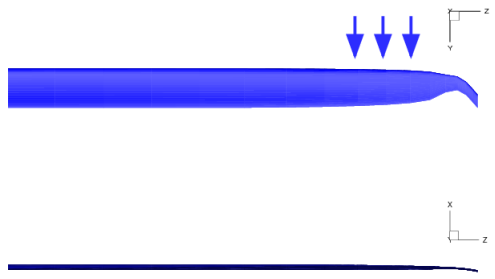

(h) **UPM-BET** - blade design

Figure 4.4: Normed radius over chord length range and blade planforms for different methods

Aeroacoustic Analysis of the best Designs

In figure 4.5, the difference plots for the best designs of the chord study are displayed. The difference is made between the absolute values of SPL of the best design and the carpet plots in figure 4.1 for the respective methods. The blue and dark blue areas represent areas of noise reduction, where red areas represent an increase in noise. The white areas represent minimal changes in either direction. The absolute plots are shown in the appendix, in figure A.5.

In figure 4.5(a), a significant reduction in noise in the peak is predicted by **METAR**. The peak near $\psi = 90°$ shows a reduction of about 5 dB. The overall noise level shows a reduction of about 1 to 3 dB. A minimal increase in noise can be observed on the retreating side near $\psi = 330°$ outside the rotor disc.

MESIR, depicted in figure 4.5(b), predicts an overall reduction in noise level of about 5 to 7 dB, compared to its baseline. The planforms of **METAR** and **MESIR** are similar, yet **MESIR** predicts a larger reduction in noise level. But, the maximum noise level of the baseline case of **MESIR** was larger than the baseline of **METAR**. The difference in noise level in the respective peaks between these blade designs is about 3 dB, seen in figures A.5(a) and A.5(b).

UPM-METAR predicts a reduction in noise up to 10 dB in the lower right corner, seen in figure 4.5(c). An overall reduction of about 5 to 7 dB and no increase in noise level can be observed. The noise level in the peak has not been reduced significantly, seen in figure A.5(c).

In figure 4.5(d), **UPM-BET** shows an overall reduction of about 1 to 3 dB, compared to its baseline. Especially the smaller peaks on the retreating side near $\psi = 0°$ are reduced. In figure A.5(d), a smaller peak on the retreating side at $\psi = 300°$ is identified.

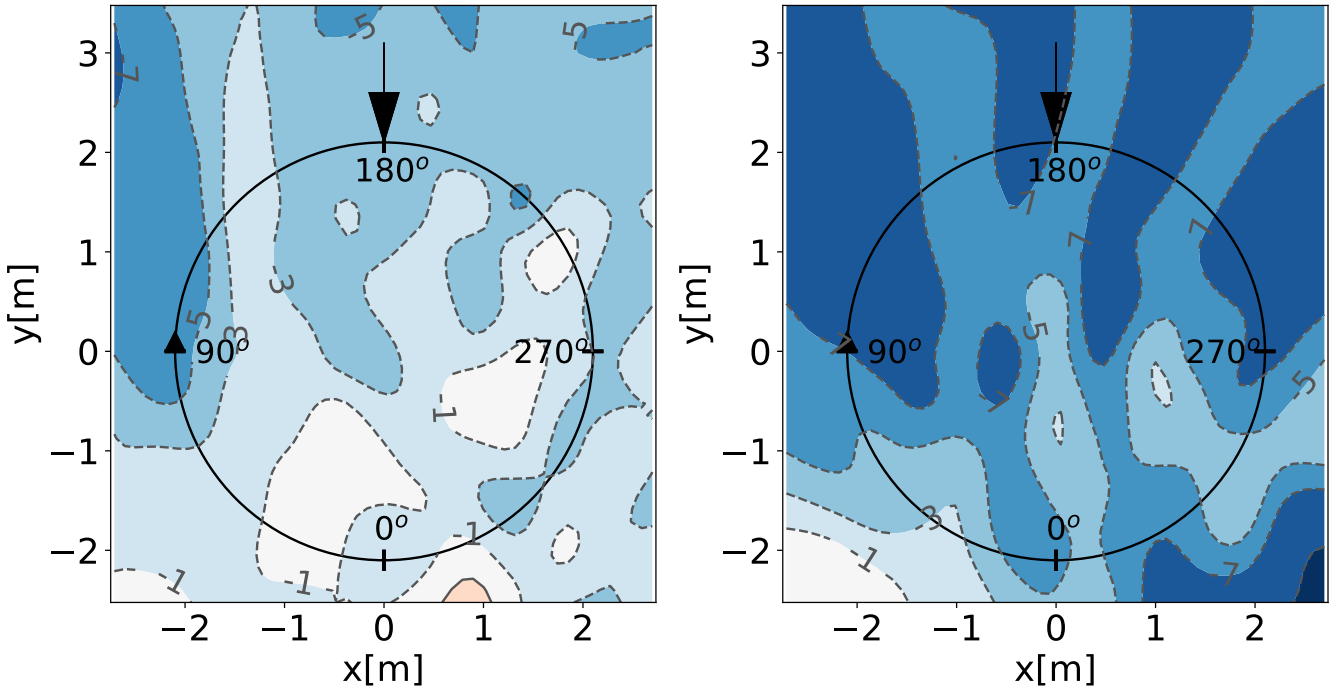

(a) ΔSPL - **METAR**

(b) ΔSPL - **MESIR**

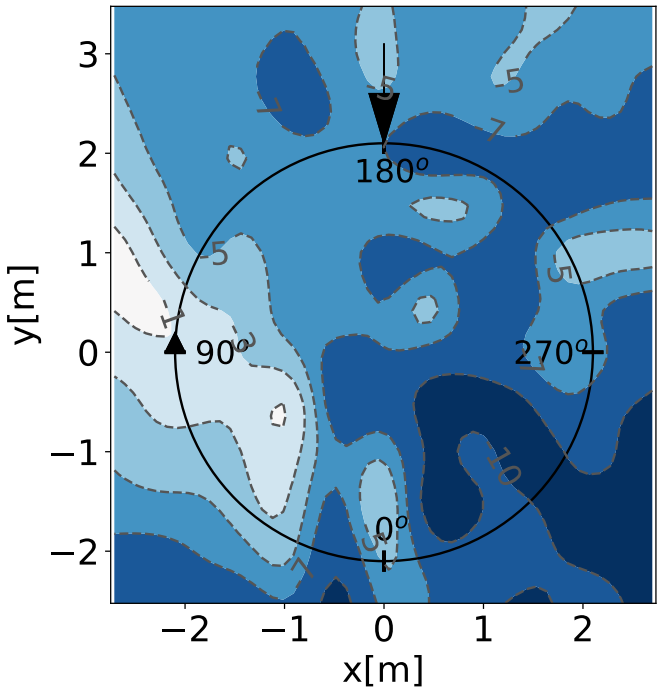

(c) ΔSPL - **UPM-METAR**

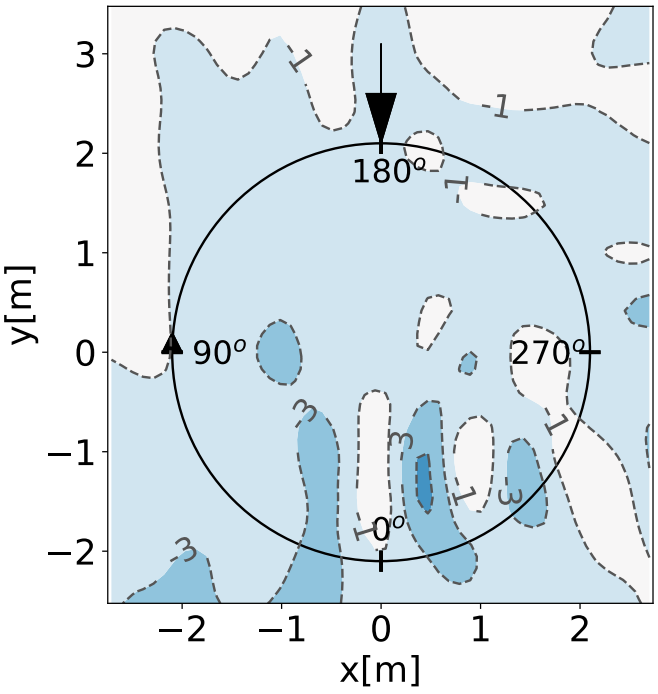

(d) ΔSPL - **UPM-BET**

Figure 4.5: Difference SPL [dB] for chord length parameterization

Airload Analysis of the best Designs

In figure 4.6, the delta-airloads and the temporal derivatives of the absolute values are displayed for the best designs. The absolute airloads are presented in the appendix in figure A.6.

The difference in loads predicted by **METAR**, depicted in figure 4.6(a) show an increase in airloads near the blade root. Near the tip, there is a decrease in airloads on both, the advancing and retreating side of the blade. Between $\psi = 0°$ and $\psi = 90°$ a change in oscillations can be observed and the loss in lift is smaller. Due to the smaller chord length less lift is produced. In figure 4.6(b), the derivatives for **METAR** are displayed. Compared to its baseline, less and weaker oscillations are observed, especially on the advancing side of the blade. The weaker wiggles are accountable for the noise reduction, seen in figure 4.5(a).

The airloads from **MESIR**, depicted in figure 4.6(c), show a change in oscillations on the advancing side at $\psi = 90°$ and the retreating side at $\psi = 270°$. Near the root more and near the tip less lift is generated. This behaviour has been observed for **METAR** too. Both methods predict a similar best design, yet **MESIR** shows a larger change in oscillations than **METAR**. In figure 4.6(d), the derivative loads are displayed. Although the blade planform between both simulations is similar, **MESIR** predicts stronger oscillations on the advancing side than **METAR**. The wake behind the rotor at $\psi = 0°$ is also stronger and shows the same behaviour like the baseline calculation. This high number of fluctuations behind the rotor and on the advancing side are accountable for the amount of spread around the peak, observed in the noise carpet in figure A.5(b). The wiggles on the retreating side at $\psi = 300°$ are smaller than the baseline, hence the noise in this area has been reduced significantly.

The best design predicted by **UPM-METAR** has a larger area then the **HOST** predicted designs. Hence, the loss in lift at the tip, seen in figure 4.6(e), is lower and the gain in lift near the root is also lower. Yet, the same effect as for **MESIR**, a change in fluctuations around $\psi = 45°$, is observed. In figure 4.6(f), less oscillations on the advancing side at $\psi = 45°$ and retreating side at $\psi = 315°$, are identified. Due to the smaller number and the lower amplitude, the noise level is decreased significantly.

In figure 4.6(g), the difference in airloads compared to the baseline case, predicted by **UPM-BET**, is presented. Instead of reducing the lift through the smaller tip, an overall increase in lift is predicted. In addition, a difference in oscillations on the advancing and retreating side can be observed. The effect of the changed wiggles is displayed in figure 4.6(h). Compared to its baseline case, weaker and less fluctuations are predicted. Due to the smaller wiggles the noise is reduced, what can be observed in figure 4.5(d). In addition, the wake is displayed in figure A.13(c). Compared to the baseline case, the vortices are larger, hence the interaction between blades and vortices has been reduced. Due to the larger area at the tip compared to **UPM-METAR**, the oscillations are not weakened by the same amount.

In conclusion, it can be said that making the chord length at the tip smaller does have an effect on airloads and the emitted noise. By reducing the chord length closer to the blade root, the noise is lower, but the lift also decreases. Due to the reduction in lift, the possibility of stall increases. Therefore, a compromise has to be found between emitted noise and lift generation. Furthermore, the vortices are larger, what directly affects BVI.

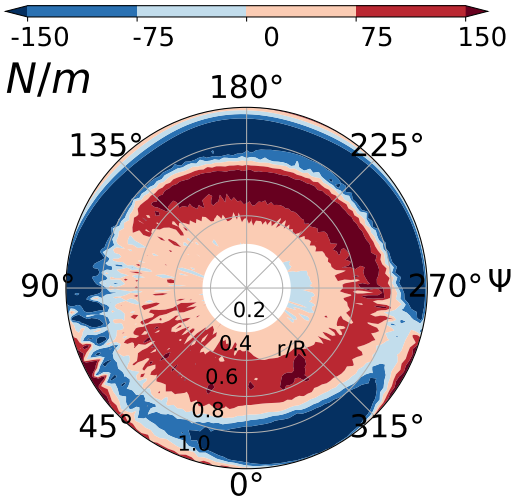

(a) ΔLoads - **METAR**

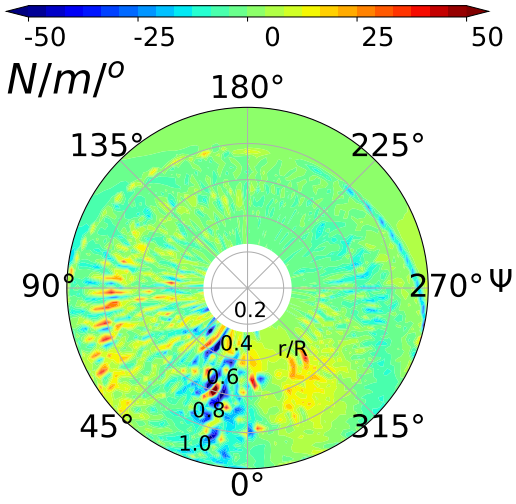

(b) Derivatives - **METAR**

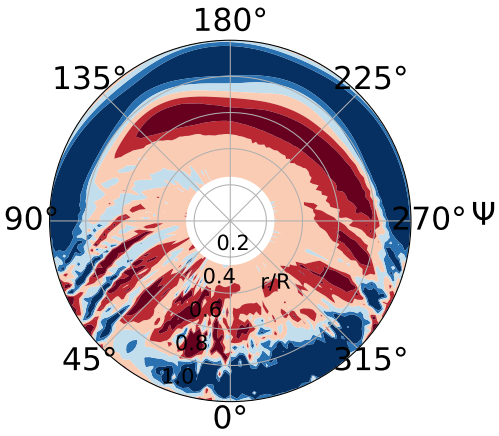

(c) ΔLoads - **MESIR**

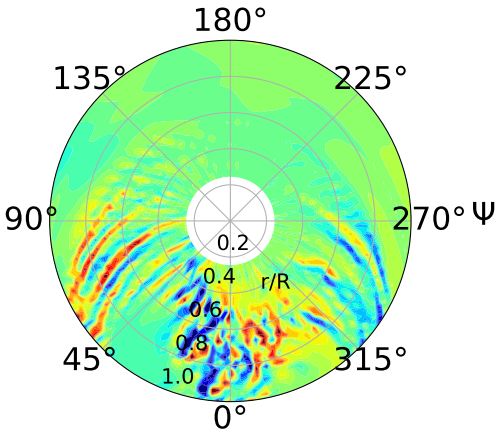

(d) Derivatives - **MESIR**

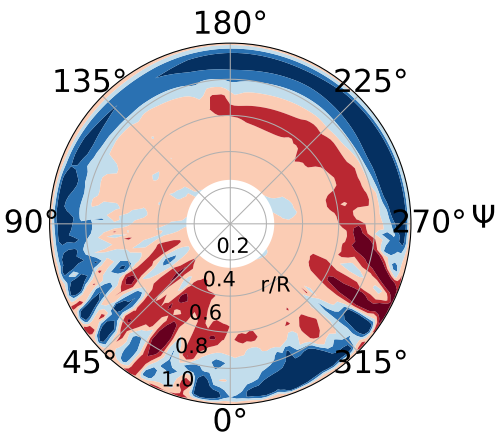

(e) ΔLoads - **UPM-METAR**

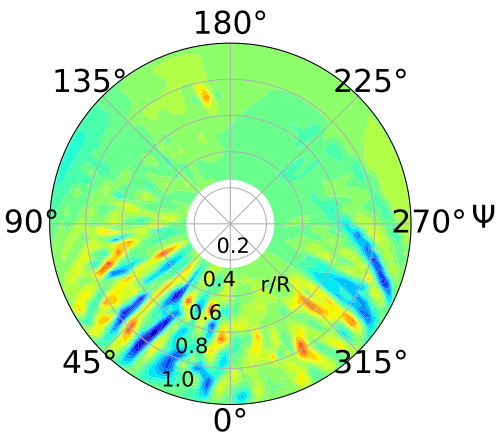

(f) Derivatives - **UPM-METAR**

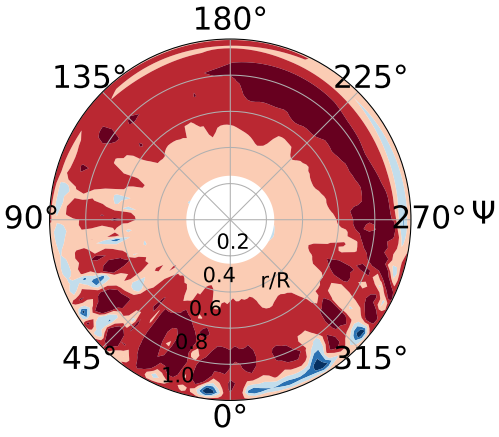

(g) ΔLoads - **UPM-BET**

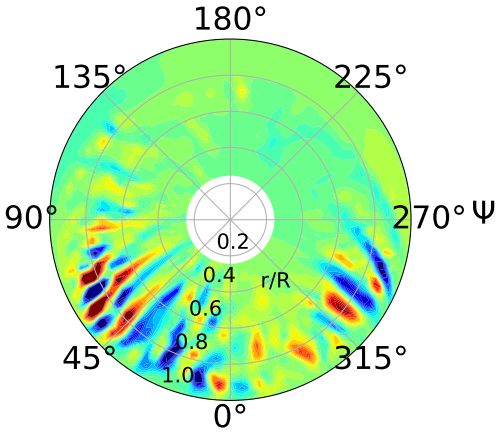

(h) Derivatives - **UPM-BET**

Figure 4.6: ΔLoads and derivatives for chord length parameterization

4.3.2 Anhedral

Behaviour of Simulations and Identifying the best Designs

In figure 4.7, the landscape plots and the planforms for the four used methods of the anhedral study are presented. The representation of the results is the same as for the chord study. It is mentionable that nearly all simulations were successful in contrast to the chord variation.

In figure 4.7(a), the variation for **METAR** is displayed. It predicts that an upwards directed tip is beneficial to reduce noise and it predicts that downwards directed tips are not suited for this. As already mentioned, the wake of the helicopter is pushed out of the plane slowly. Through an upwards directed tip, the vortices are set off above the rotor plane and lead to reduction of noise. In addition, it is possible that the vortices are weaker.

MESIR also predicts an upward directed blade tip for lower noise, yet the location of the planform change is different then for **METAR**, depicted in figure 4.7(b). In contrast to **METAR**, configurations with only a little downwards directed tip reduce the noise. Although **MESIR** overpredicted the noise compared to the other methods, its wake model is physically more accurate than **METAR**. Hence, it is possible that **MESIR** is capturing elements with a downwards directed tip to reduce noise, which **METAR** can not.

UPM-METAR, displayed in figure 4.7(e), shows that using any anhedral at the blade is increasing the noise, hence no optimum is displayed. In addition, no correlation with other methods can be observed. The structural model between **METAR** and **UPM-METAR** is the same, hence the differences between these methods are of aerodynamic origin.

UPM-BET, presented in figure 4.7(f), predicts an upward directed tip for lower noise. Unlike **METAR**, it predicts two spots of configurations that are beneficial to reduce noise. In addition, the amount of anhedral is lower compared to the results of the **HOST** simulations. Unlike the rest of the simulations, **UPM-BET** has difficulties to simulate configurations with a large upwards directed tip from $r/R = 0.7$ to 0.9. The wake of the design, displayed in figure 4.7(h), can be seen in the appendix in figure A.13(d). The vortices are set off above the rotor disc and they also increase in size behind the rotor. Hence the interaction between blades and vortices is directly affected.

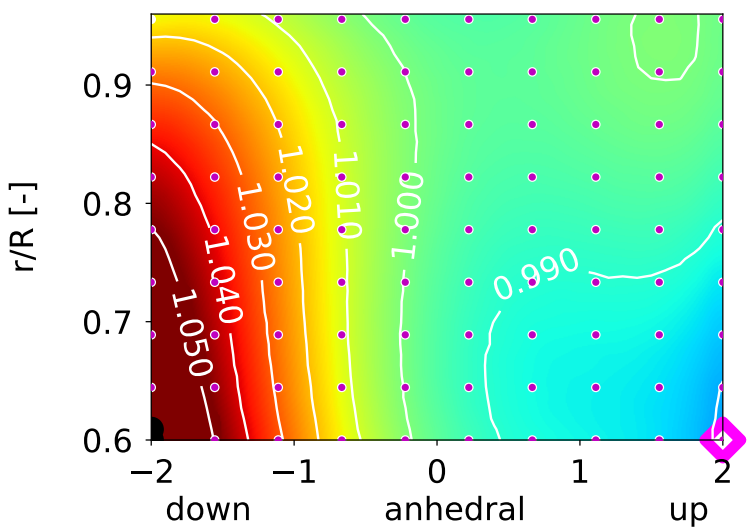

(a) **METAR**

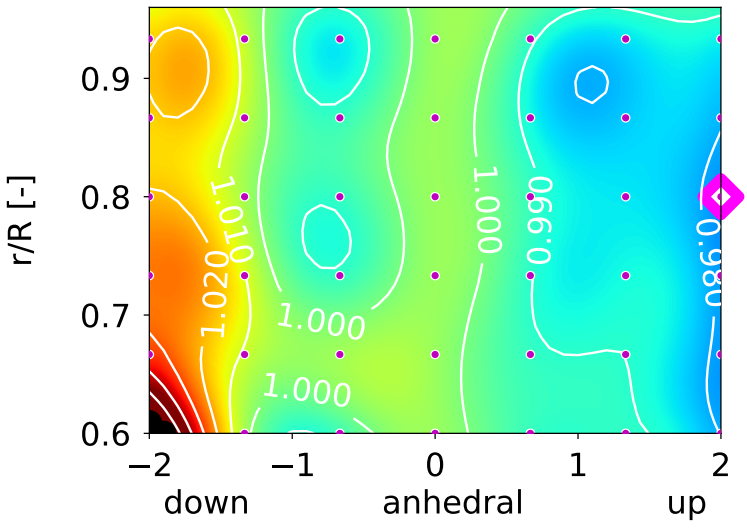

(b) **MESIR**

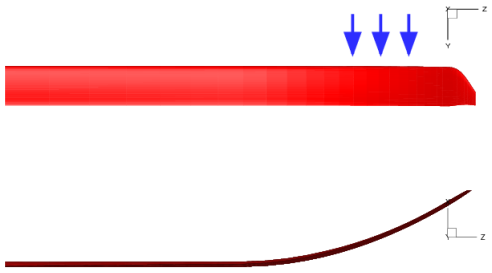

(c) **METAR** - blade

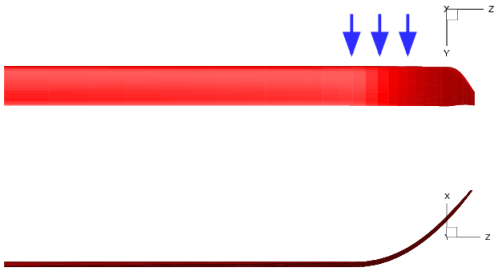

(d) **MESIR** - blade

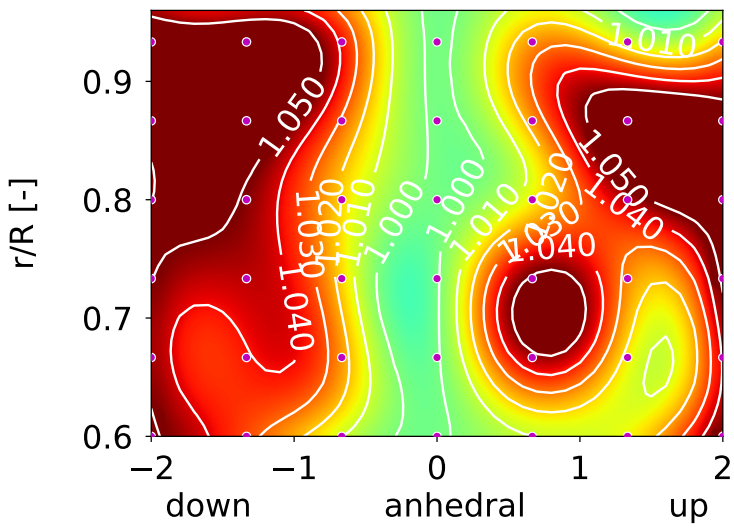

(e) **UPM-METAR**

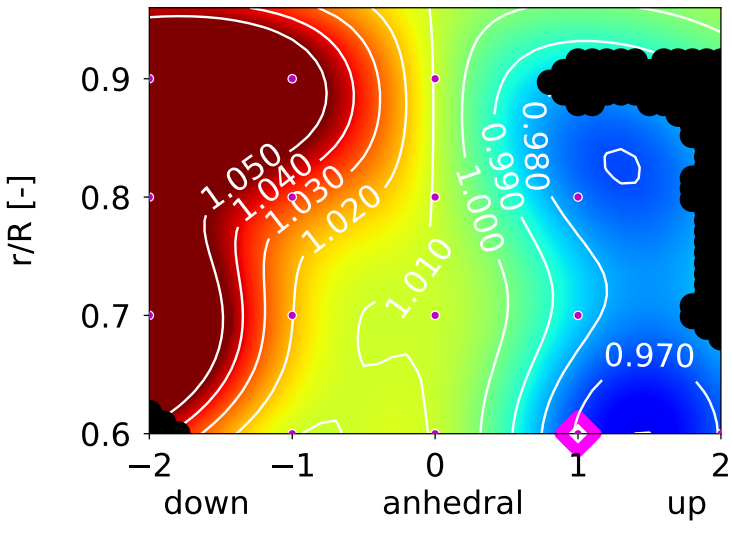

(f) **UPM-BET**

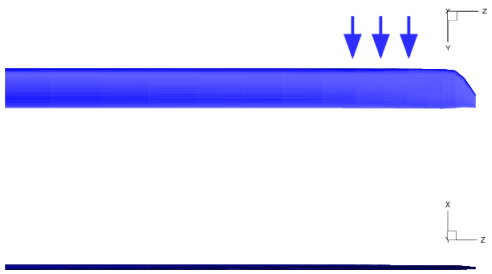

(g) **UPM-METAR** - blade

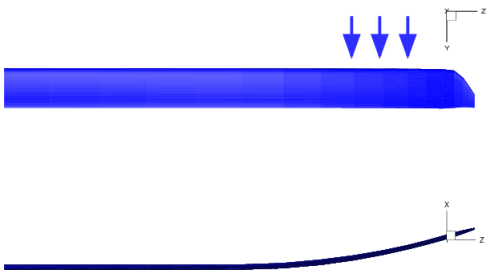

(h) **UPM-BET** - blade

Figure 4.7: Normed radius over anhedral range and blade planforms for different methods

Aeroacoustic Analysis of the best Designs

In figure 4.8 the delta noise carpets for the best configurations of the anhedral study are displayed. The absolute values are depicted in the appendix, in figure A.7

In figure 4.8(a), the difference plot from **METAR** is presented. An overall reduction compared to the baseline is observed. From $\psi = 90°$ to $\psi = 270°$ there is a reduction of 5 to 10 dB identified. On the retreating side from $\psi = 270°$ to $\psi = 45°$, there is a rise in emitted noise of about 1 to 7 dB.

MESIR, in figure 4.8(b), predicts a reduction in the overall noise level of about 3 to 7 dB, compared to its baseline. The most significant reduction of 7 dB is observed on the retreating side from $\psi = 180°$ to $\psi = 270°$. Near $\psi = 90°$, a small increase in emitted noise is observed. Hence, the noise in the peak has not been reduced significantly, but the noise outside the rotor disc. This leads to a shift of the peak to the lower left corner, seen in figure A.7(b).

Due to the minimal change in planform, the removal of the anhedral at the tip, **UPM-METAR** also predicts a minimal change in emitted noise, seen in figure 4.8(c). Less noise is generated near $\psi = 45°$ and more noise is generated around $\psi = 270°$. Inside the rotor disc, nearly no change is identified.

UPM-BET, depicted in figure 4.8(d), predicts an overall reduction in noise of about 3 to 5 dB. Some areas are identified where the noise is even larger reduced up to 7 dB. On the retreating side near $\psi = 300°$, outside the rotor disc a small increase of noise is observed.

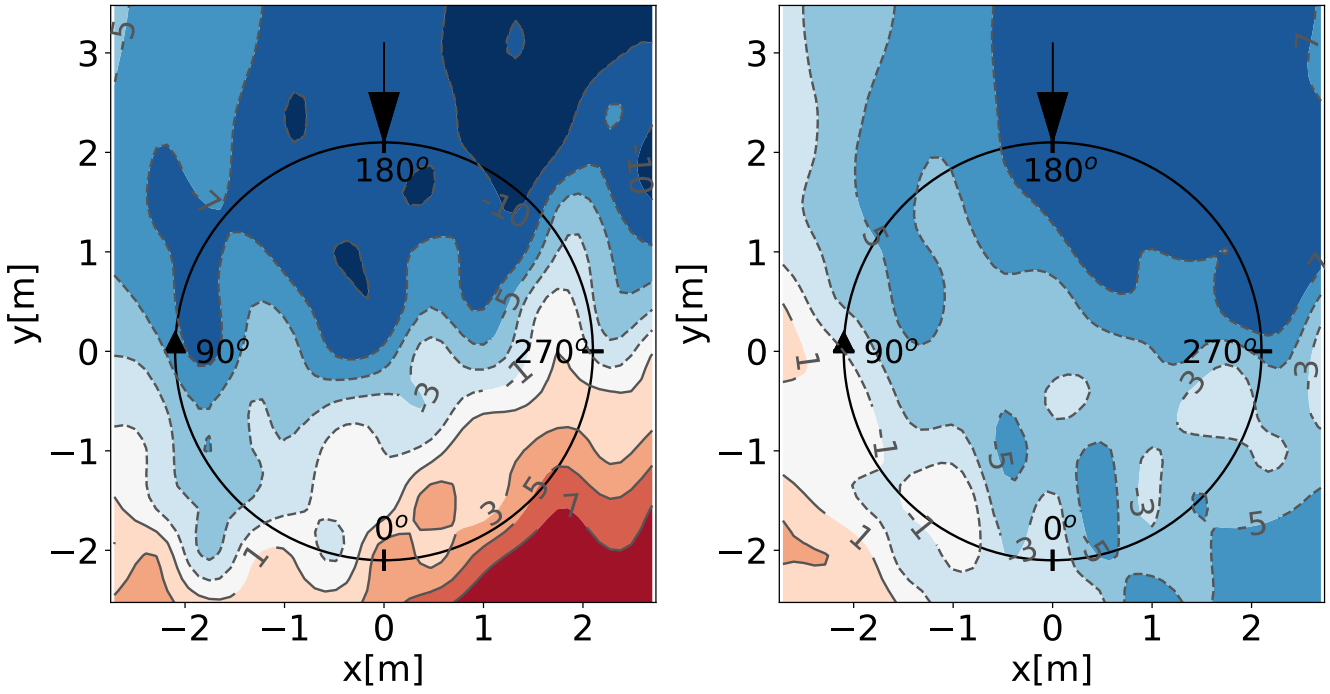

(a) ΔSPL - **METAR**

(b) ΔSPL - **MESIR**

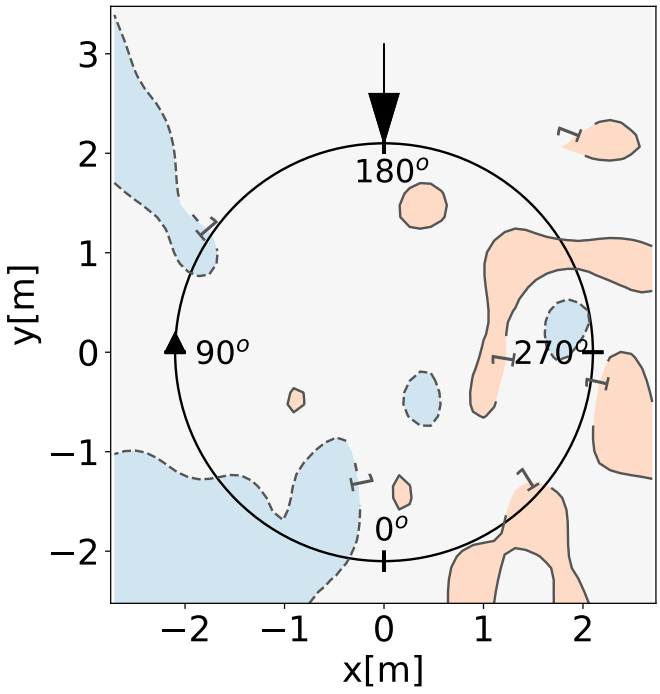

(c) ΔSPL - **UPM-METAR**

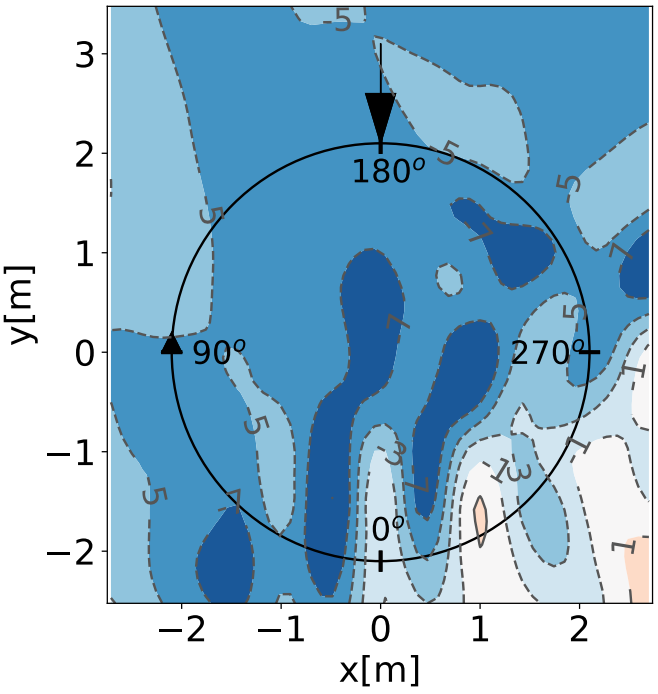

(d) ΔSPL - **UPM-BET**

Figure 4.8: Difference SPL [dB] for anhedral parameterization

Airload Analysis of the best Designs

In figure 4.9, the difference airloads and temporal derivatives of the used methods for the best anhedral results are presented. The absolute values of the loads are displayed in the appendix in figure A.8

In figure 4.9(a), for **METAR**, a decrease in airloads on the advancing side is observed. Furthermore, a change in oscillations is identified from $\psi = 0°$ to $\psi = 90°$. On the retreating side, there is an increase in airloads, except for $\psi = 225°$ near the tip and $\psi = 330°$. The wiggles are also seen in figure 4.9(b), where the derivatives are displayed. Although the fluctuations are stronger compared to the baseline case, they occur between $r/R = 0.8$ and $r/R = 1.0$ near the blade tip. These fluctuations are accountable for the higher noise outside the rotor plane in the noise carpet. Through the directivity of noise and the translatory speed of the helicopter, the peaks are not inside the rotor disc. At the front, nearly no amplitudes are identified, hence the noise outside the rotor disc is much lower.

MESIR predicts a change in wiggles on both, the advancing and retreating side, seen in figure 4.9(c). In addition, the oscillations near $\psi = 0°$ also experience a change in amplitude. At the front of the rotor disc, changes of the airload along the blade are observed. In figure 4.9(d), the fluctuations and their changed amplitudes are observed from $\psi = 270°$ to $\psi = 90°$. Due to the number of wiggles on the advancing side around $\psi = 45°$ and their respective strength, the noise does not experience a significant reduction in that area. At the front near $\psi = 180°$, no wiggles are identified, hence the noise is reduced significantly.

UPM-METAR, depicted in figure 4.9(e), predicts less lift along the blade with small areas of lift gain. Additionally, small changes in oscillations can be observed on the advancing and retreating side of the blade. Due to the small change in planform, only small changes are observed in figure 4.9(f). Hence, the generated noise does not change significantly.

In figure 4.9(g), the difference airloads of **UPM-BET** are displayed. At the front near the tip and from $\psi = 270°$ to $\psi = 90°$, an overall increase in lift can be observed. In addition, a change in fluctuations around $\psi = 45°$ and $\psi = 90°$ is identified. The fluctuations are observed in figure 4.9(h). The amplitudes are lower and focused near the tip of the blade, compared to the baseline case. Due to the reduced number of oscillations near the root of the blade and at the front, the overall reduction in the noise carpet is explained.

Due to an upwards directed tip, the wiggles are focused near the tip of the blade. Furthermore, the vortices are set off above the rotor plane, so that the interaction between blades and vortices is reduced. In most cases the noise is reduced significantly, but its on cost of lift changes.

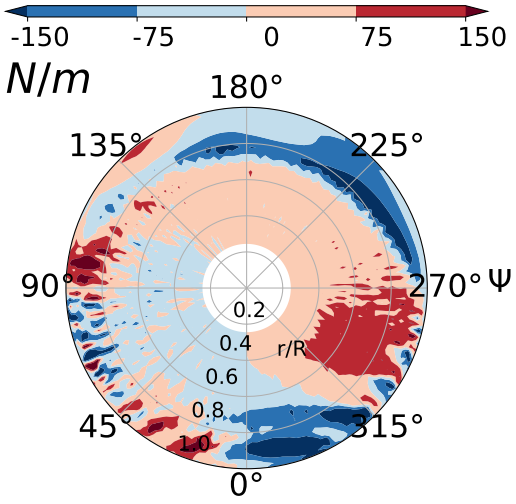

(a) ΔLoads - **METAR**

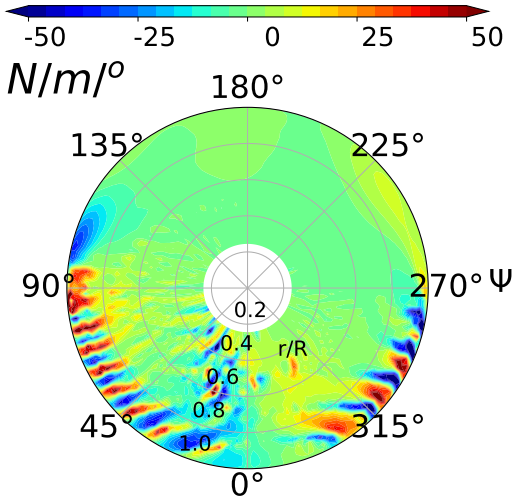

(b) Derivatives - **METAR**

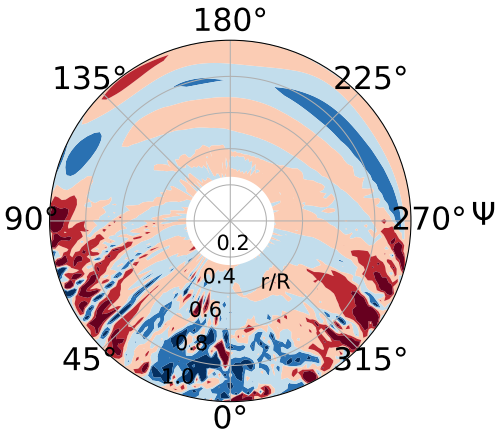

(c) ΔLoads - **MESIR**

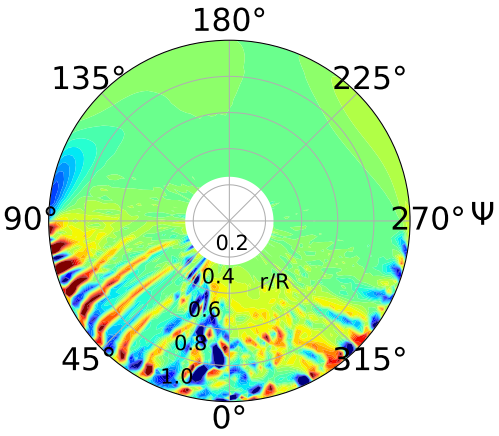

(d) Derivatives - **MESIR**

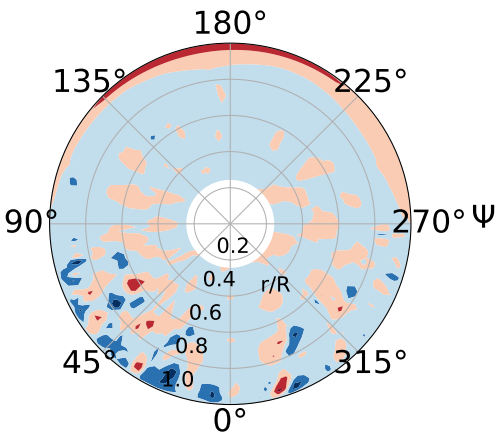

(e) ΔLoads - **UPM-METAR**

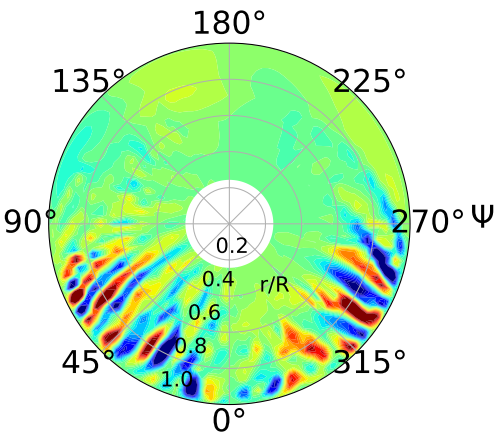

(f) Derivatives - **UPM-METAR**

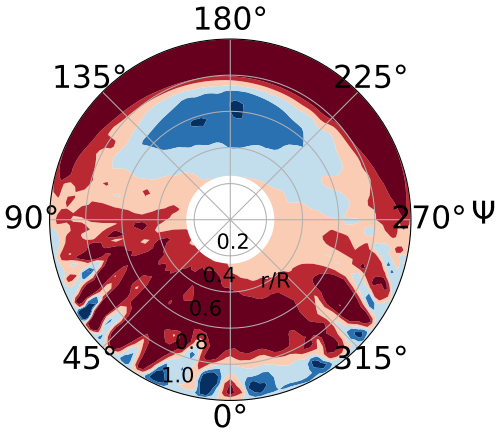

(g) ΔLoads - **UPM-BET**

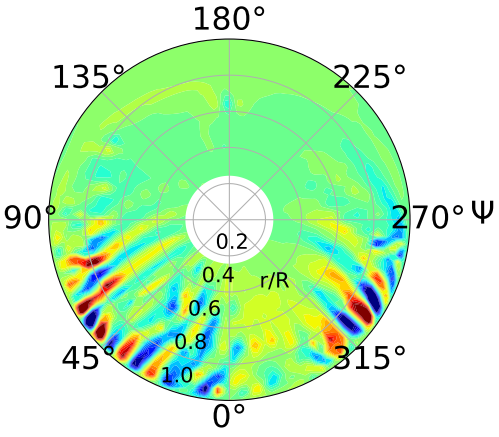

(h) Derivatives - **UPM-BET**

Figure 4.9: ΔLoads and derivatives for anhedral parameterization

4.3.3 Sweep

Behaviour of Simulations and Identifying the best Designs

In figure 4.10, the results of the sweep study are displayed. The number of variables is three, hence the behaviour of sweep along the blade at $r/R = 0.7$ and $r/R = 0.9$ is displayed for each method. The planforms of the blades and the optimums for each method are presented in figure 4.11. Note: Sweep-1 is the amount of sweep at r/R and sweep-2 is the amount of sweep at the blade tip.

In figure 4.10(a) and 4.10(b), the results for **METAR**, at the specific locations, are depicted. A backward swept blade is predicted as a beneficial solution for noise reduction. Some of the configurations do fail, especially when a forward swept blade is investigated. In figure 4.11(a) the optimum for **METAR** at $r/R = 0.6$ is displayed. Observing the behaviour of the plot, an area with a forward-backward swept blade is identified near $(x = -1, y = 2)$, where the noise is low. This would result in the well known **ERATO** blade.

The slices for **MESIR**, depicted in figures 4.10(c) and 4.10(d), are made in areas where no configurations are investigated directly, hence no dots for the specific designs are displayed. Areas with pure forward swept configurations are successfully simulated and seem useful for noise reduction. In figure 4.11(b), the optimum for **MESIR** is displayed at $r/R = 0.73$. The blade design is much like **METAR**, yet the location for the change in planform is later. A direct comparison of the blade designs show that **MESIR** predicts a more smooth transition, compared to **METAR**. It also predicts an area where a double swept blade configuration is reducing the noise.

The results of **UPM-METAR** are presented in figures 4.10(e) and 4.10(f). Unlike **METAR**, **UPM-METAR** predicts the best case solutions with a combination of sweep, be it forward-backward or backward-forward. In figure 4.11(e), the best design for **UPM-METAR** is depicted. The best planform of the successful configurations is found for a backward-forward swept blade configuration at $r/R = 0.87$. The optimum calculated by the surrogate models, predict a forward-backward swept blade as best design, yet these can not be trimmed with **METAR**.

UPM-BET, displayed in figure 4.10(g) and 4.10(g), also predicts a combination of backward-forward sept blades as best cases. Unlike **UPM-METAR**, no beneficial configurations with an **ERATO** like design seem beneficial for noise reduction. The aero-elastic effects may be to large that trimming is successful. The best case at $r/R = 0.8$, seen in figure 4.11(f), is similar to the design of **UPM-METAR**, yet the location of the change in planform is earlier.

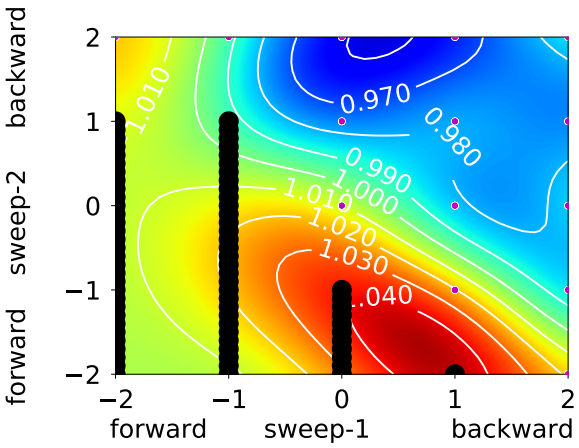

(a) **METAR** - $r/R = 0.7$

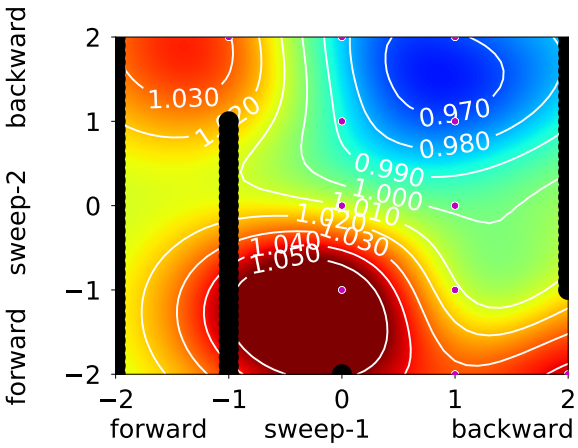

(b) **METAR** - $r/R = 0.9$

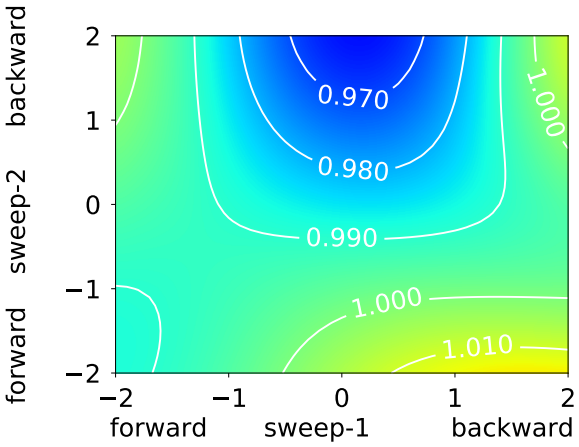

(c) **MESIR** - $r/R = 0.7$

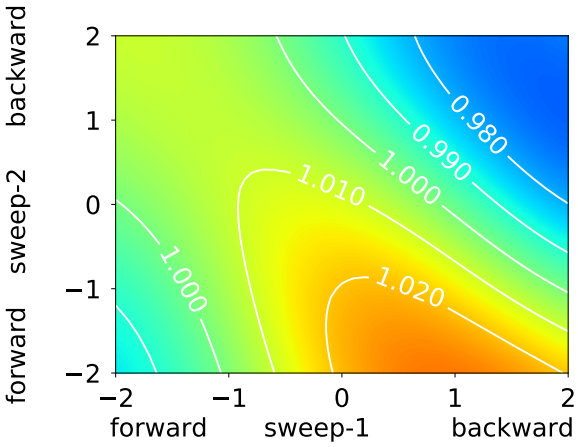

(d) **MESIR** - $r/R = 0.9$

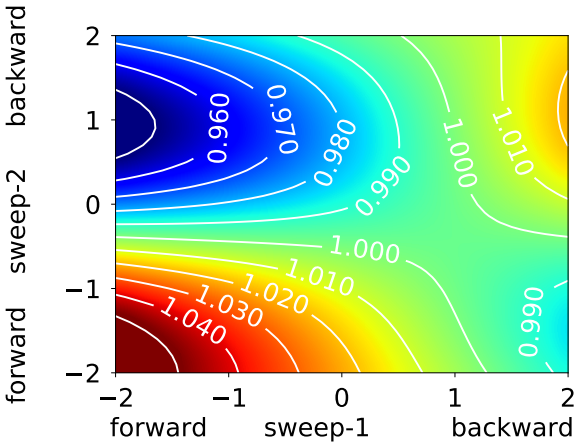

(e) **UPM-METAR** - $r/R = 0.7$

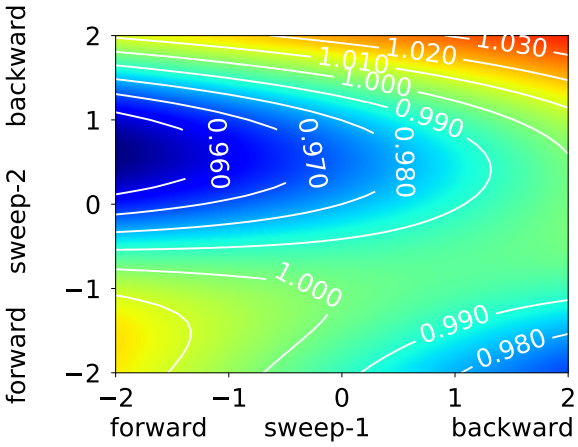

(f) **UPM-METAR** - $r/R = 0.9$

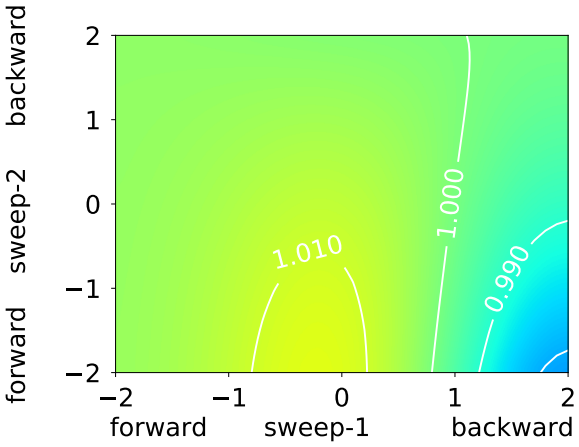

(g) **UPM-BET** - $r/R = 0.7$

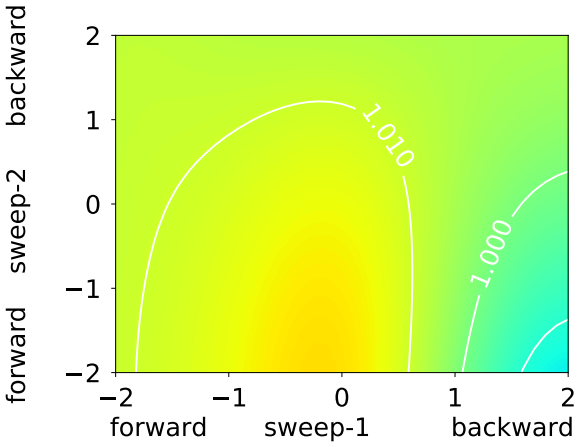

(h) **UPM-BET** - $r/R = 0.9$

Figure 4.10: Sweep displayment at different normed radii for different methods

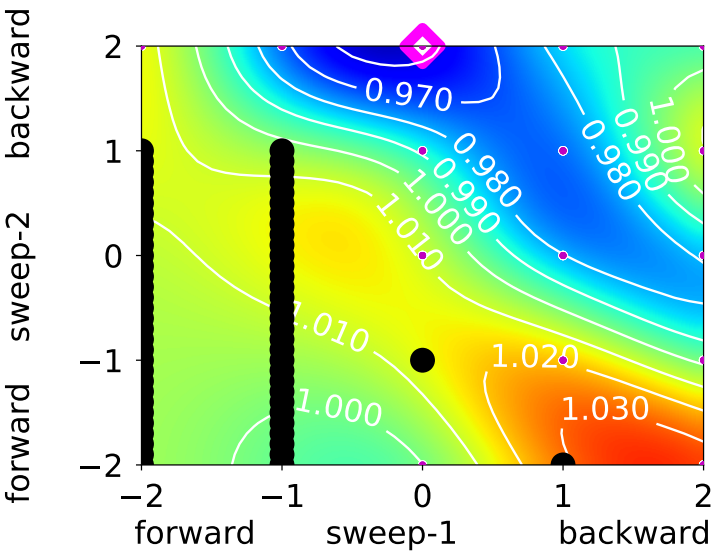

(a) **METAR** - $r/R = 0.60$

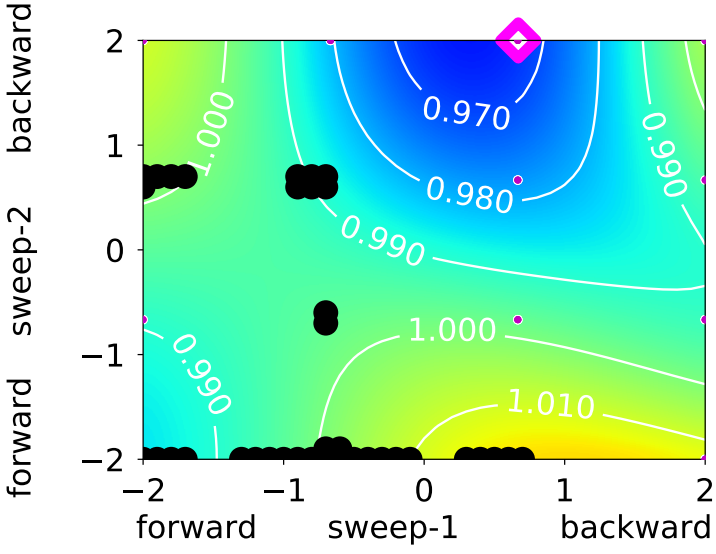

(b) **MESIR** - $r/R = 0.73$

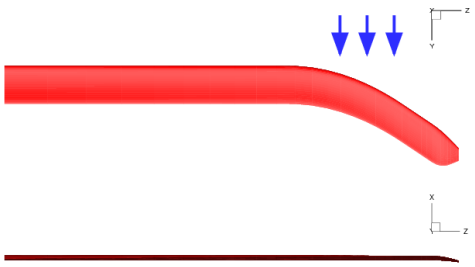

(c) **METAR** - blade

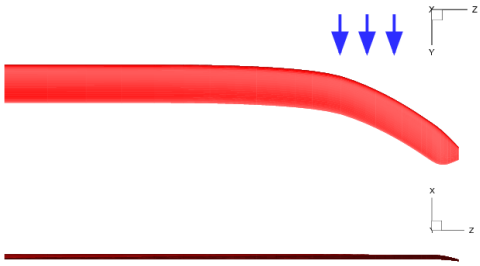

(d) **MESIR** - blade

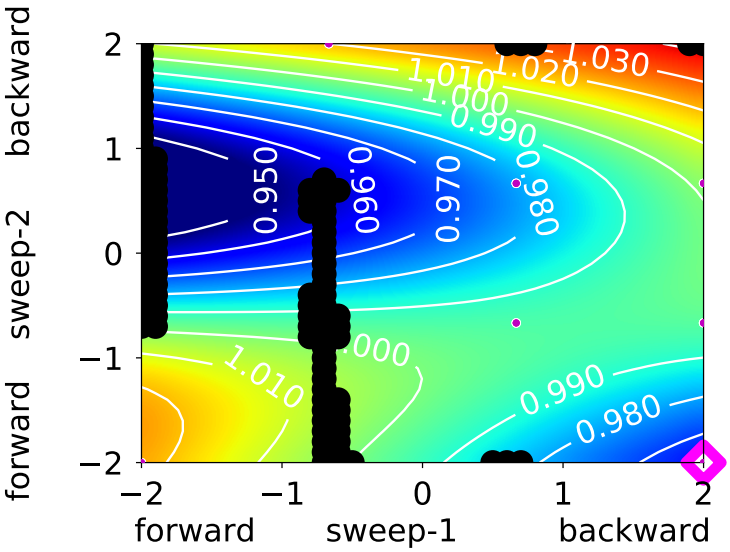

(e) **UPM-METAR** - $r/R = 0.87$

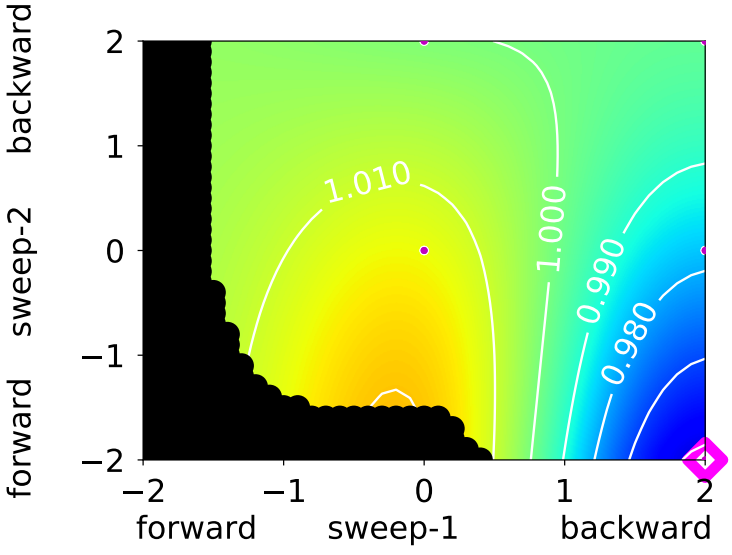

(f) **UPM-BET** - $r/R = 0.80$

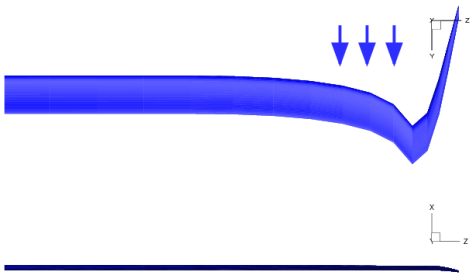

(g) **UPM-METAR** - blade

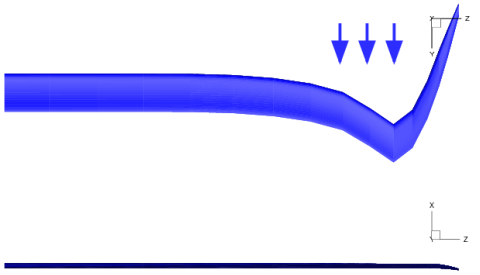

(h) **UPM-BET** - blade

Figure 4.11: Best designs - sweep settings and planforms for different methods

Aeroacoustic Analysis of the best Designs

In figure 4.12 the delta noise carpets for the optimal designs of the sweep study are displayed. In the appendix, in figure A.9, the absolute values are depicted.

METAR, depicted in figure 4.12(a), predicts an overall noise reduction of about 1 to 3 dB. The noise in the peak has not been reduced by a significant amount. Outside the rotor disc from $\psi = 90°$ to $\psi = 270°$ the noise has been reduced by about 3 dB. In addition, small areas inside the disc are observed, where more noise is generated.

MESIR, displayed in figure 4.12(b) predicts an overall reduction in noise level of 1 to 3 dB. A significant reduction of 5 dB is predicted inside the rotor disc near $\psi = 45°$. An increase in noise is observed outside the disc at $(x = -2, y = -2)$. The planforms of **METAR** and **MESIR** are similar. The noise reduction by both methods is similar too, with small differences inside and outside the rotor plane.

Figure 4.12(c) shows the results of the best design from **UPM-METAR**. An overall reduction of noise of about 3 to 7 dB is achieved. On the retreating side and inside the rotor disc, areas of 10 dB are identified. Yet, the noise near $\psi = 90°$ show just minimal changes and even a small increase in emitted noise, hence the noise in the peak has not been reduced significantly.

UPM-BET predicts an overall noise reduction of about 3 to 7 dB and up to 10 dB outside the rotor disc on the retreating side of the blade, seen in figure 4.12(d). Due to the similar design between the **UPM** methods the amount of noise reduction is also similar. Yet, the minimal reduction for **UPM-BET** is 3 dB and no increase in noise is observed. Due to the sweeping, the vortices that are depicted in figure A.13(e) are larger and set off above the rotor plane, compared to the baseline case in figure A.13(b). In addition, it is possible that the vortices are split, but this can not be observed in the wake figures.

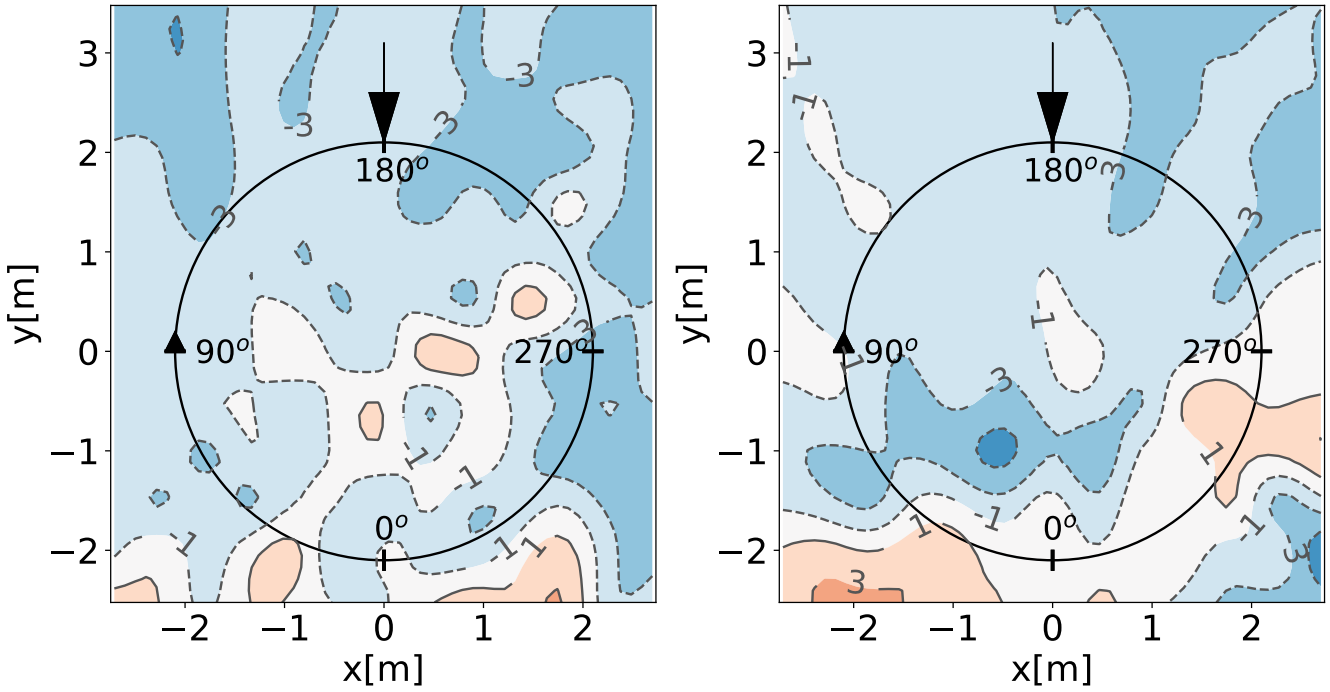

(a) ΔSPL - **METAR**

(b) ΔSPL - **MESIR**

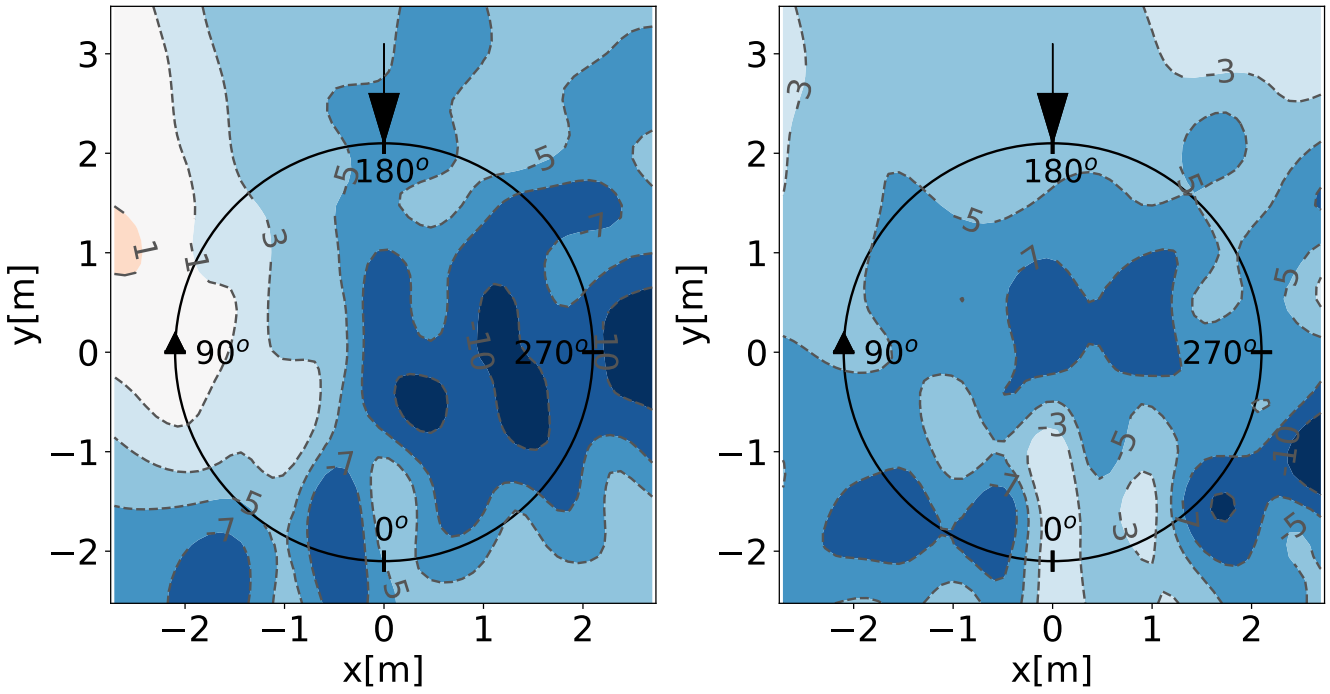

(c) ΔSPL - **UPM-METAR**

(d) ΔSPL - **UPM-BET**

Figure 4.12: Difference SPL [dB] for sweep parameterization

Airload Analysis of the best Designs

In figure 4.13, the difference airloads and temporal derivatives of the best planforms of the sweep study, are presented. The absolute values of the airloads are displayed in the appendix in figure A.10.

METAR, depicted in figure 4.13(a), predicts less lift near the tip of the blade, except near $\psi = 45°$ on the advancing side and $\psi = 300°$ on the retreating side. Near the root of the blade, especially on the advancing side more lift is generated. In addition, a change in oscillations can be observed there. In figure 4.13(b), the derivatives for **METAR** are displayed. Near $\psi = 0°$ and from $\psi = 45°$ to $\psi = 120°$, fluctuations with high frequencies and lower amplitudes are predicted. Due to the low amplitudes, the noise reduction is achieved. On the retreating side, near $\psi = 270°$, small amounts of oscillations with low amplitudes are identified. Due to the translatory flying speed and the directivity of the sound, the small increase in noise outside the rotor disc is explained.

In figure 4.13(c), the difference airloads for **MESIR** are presented. Due to the similar planform with **METAR**, their changes in airloads are similar too. Less lift is generated near the tip of the blade, especially at the front from $\psi = 90°$ to $\psi = 270°$. From $\psi = 270°$ to $\psi = 90°$ a change in oscillations is observed, especially on the advancing side of the blade. As seen for **METAR**, more lift is generated near the root of the blade. Although the blade planforms and difference airloads between **MESIR** and **METAR** are alike, the temporal airloads for **MESIR** are different, seen in figure 4.13(d). More fluctuations with higher amplitudes are generated on the advancing and retreating side of the blade and around $\psi = 0°$. Although more wiggles with larger amplitudes are generated the reduction of noise is similar to **METAR**. Yet, the oscillations near $\psi = 0°$ are accountable for the increase in noise on the retreating side of the blade.

Due to the strong sweeping, the airloads for **UPM-METAR**, displayed in figure 4.13(e), are reduced near the tip between $r/R = 0.8$ and $r/R = 1.0$ blade location. Close to the root of the blade more lift is generated. A change in oscillations is observed around $\psi = 45°$ on the advancing side and $\psi = 300°$ on the retreating side of the blade. This change is also observed in figure 4.13(f). The amplitude of the wiggles is smaller compared to the baseline case and the number has been decreased too. Hence, the noise is reduced by significant amounts.

In figure 4.13(g), the differences in airloads are presented for **UPM-BET**. An increase in lift is observed from the blade root to $r/R = 0.8$ of the blade. At the tip, a loss in lift is identified. The derivatives in figure 4.13(h) show differences to its baseline case. First, less and weaker wiggles are simulated on the advancing and retreating side of the blade. Hence, less noise is generated in these areas. The correlation between the **UPM** designs is best observed in the derivative plots. Only small changes in number and strength of fluctuations are identified. In addition, the amount of noise that it reduced, predicted by both methods is similar too.

As already seen for the **ERATO** and BlueEdge^{TM} blade, sweeping does have a positive effect on noise reduction [36] [10]. Due to single backwards sweeping the noise can be reduced. Yet a double backward-forward sweeping is more effective in reducing the noise. The number of oscillations and their amplitudes are reduced. Observing the planforms of the blades and their airloads, it seems that sweeping has the same effect like varying the chord length of the blade at the tip. Hence, this parameter also needs a compromise between loss in lift and noise reduction.

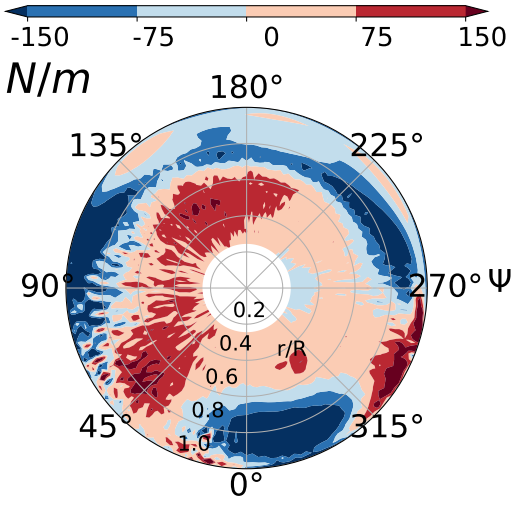

(a) ΔLoads - **METAR**

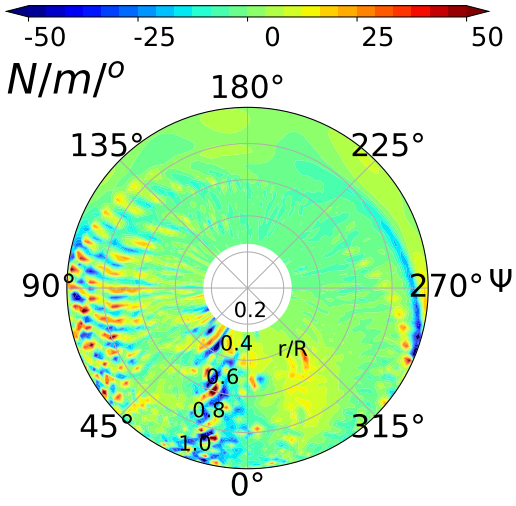

(b) Derivatives - **METAR**

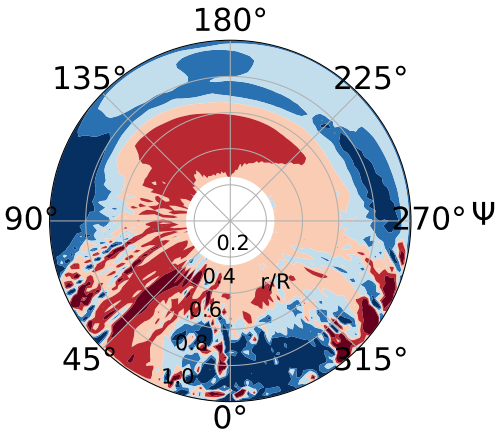

(c) ΔLoads - **MESIR**

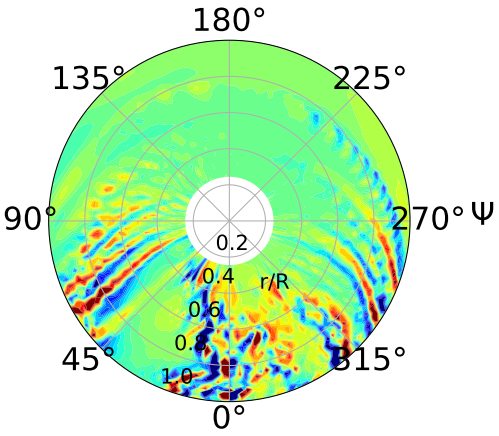

(d) Derivatives - **MESIR**

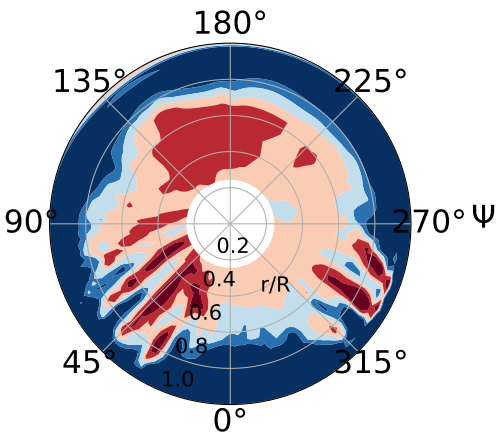

(e) ΔLoads - **UPM-METAR**

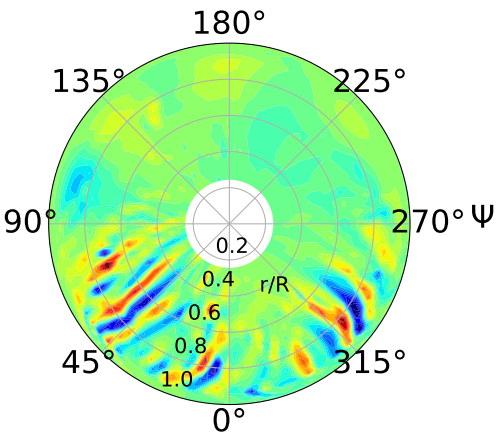

(f) Derivatives - **UPM-METAR**

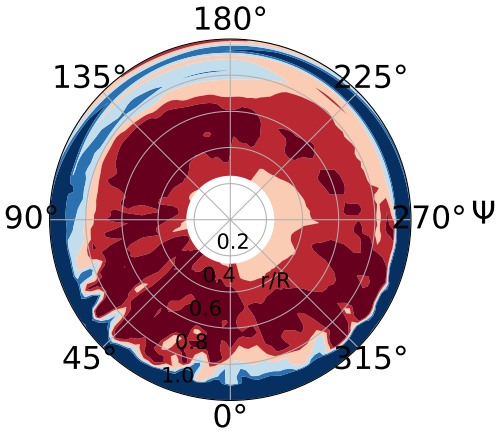

(g) ΔLoads - **UPM-BET**

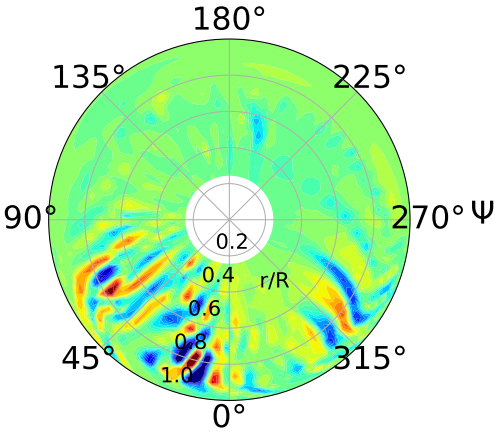

(h) Derivatives - **UPM-BET**

Figure 4.13: ΔLoads and derivatives for sweep parameterization

4.3.4 Twist

Behaviour of Simulations and Identifying the best Designs

In figure 4.14, the results for the twist study are depicted. As already done for sweep, the behaviour along the blade geometry r/R for the used methods will be described first and afterwards the optimal settings. Instead of showing the respective blade planforms, the twist distribution for the best designs is depicted in figure 4.15(e) along the blade compared to the baseline case. Note: Twist-1 is the amount of twist at the specific location r/R on the blade and twist-2 is the change at the blade tip.

METAR, displayed in figures 4.14(a) and 4.14(b), predicts that a combination of positive and negative twist along the blade is not beneficial for noise reduction. It predicts a rise up in noise by about 5% and more. A blade with pure positive twist is not beneficial either, yet no twist at all seems to have a noise reducing effect. The largest effects are identified in the centers of the plots, near $-5°$, for both twist settings and both blade slices at $r/R = 0.7$ and $r/R = 0.9$. The best case, presented in figure 4.15(a), has a twist of $-5°$ at the tip and $-5°$ at $r/R = 0.80$.

MESIR shows a similar result, yet more noise is reduced with a large amount of twist until the tip of the blade, seen in figures 4.14(c) and 4.14(d). Additionally, it predicts that twist does not have the same noise reducing capabilities like the other planform parameters. A reduction of about 2% is the best reduction that can be observed. The best design, depicted in figure 4.15(b), shows that both twist settings with $-15°$ beginning at $r/R = 0.73$ have the best noise reduction results.

UPM-METAR, depicted in figures 4.14(e) and 4.14(f), shows similar results like **METAR** and **MESIR**. Noise can be reduced by using moderate twisting like **METAR** or high amounts of twist closer to the blade root like **MESIR**. In contrast to the other two methods, it predicts that the amount of twist-1 of $-10°$ near the blade tip at $r/R = 0.9$ is not useful to reduce the emitted noise. The best design, presented in figure 4.15(c), has a twist of $-8°$ at $r/R = 0.86$ on the blade and of $-2°$ at the tip. Up to 1 to 2% of noise can be reduced.

UPM-BET, displayed in figures 4.14(g) and 4.14(h), show that changing twist-1 closer to the blade tip increases the emitted noise. An early change for this parameter however, decreases the noise, which is seen in the optimum in figure 4.15(d). The amount of twist is constant over the blade length with $-5°$, beginning at $r/R = 0.6$ blade geometry.

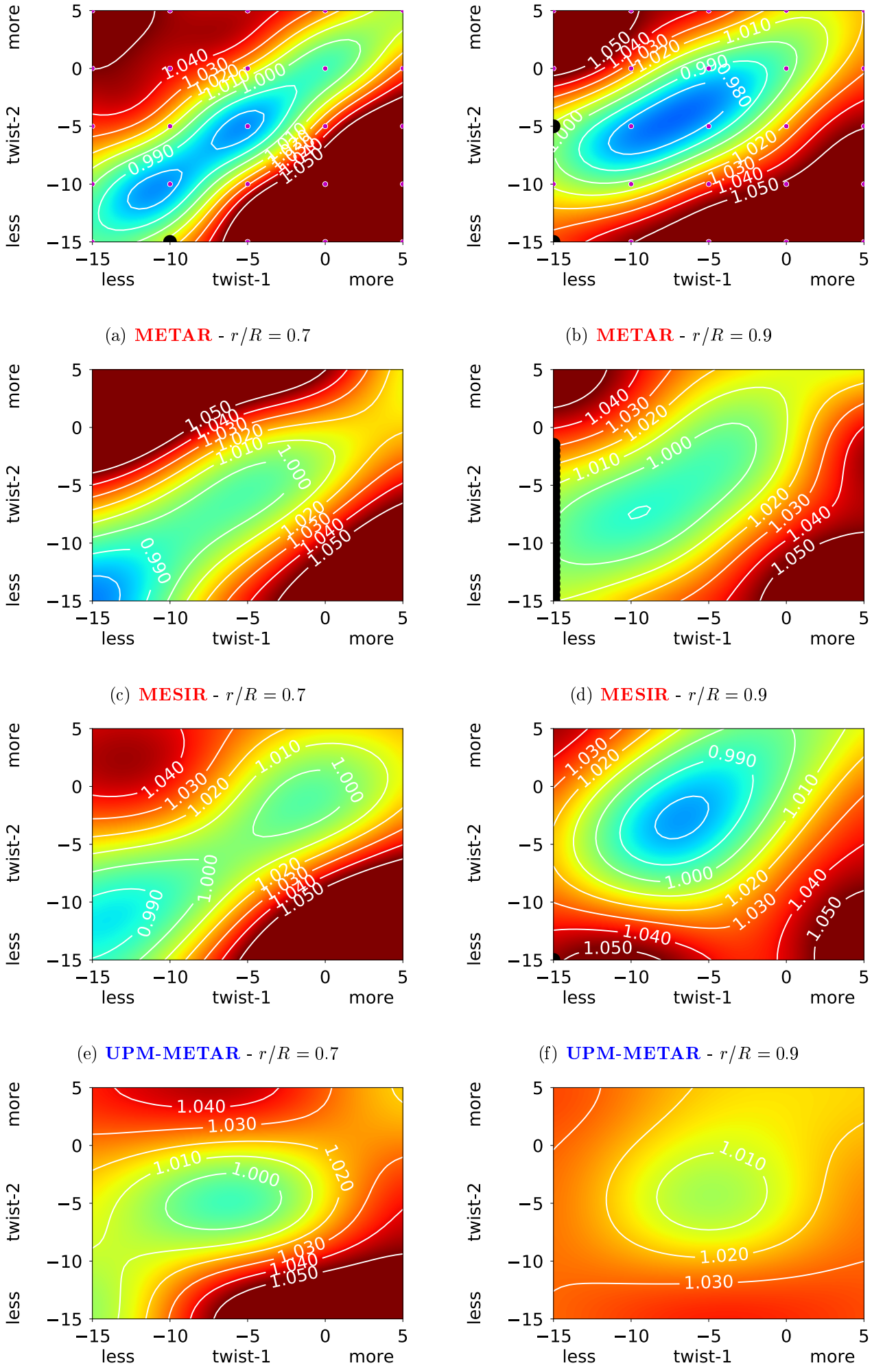

(a) **METAR** - $r/R = 0.7$

(b) **METAR** - $r/R = 0.9$

(c) **MESIR** - $r/R = 0.7$

(d) **MESIR** - $r/R = 0.9$

(e) **UPM-METAR** - $r/R = 0.7$

(f) **UPM-METAR** - $r/R = 0.9$

(g) **UPM-BET** - $r/R = 0.7$

(h) **UPM-BET** - $r/R = 0.9$

Figure 4.14: Twist displayment at different normed radii for different methods

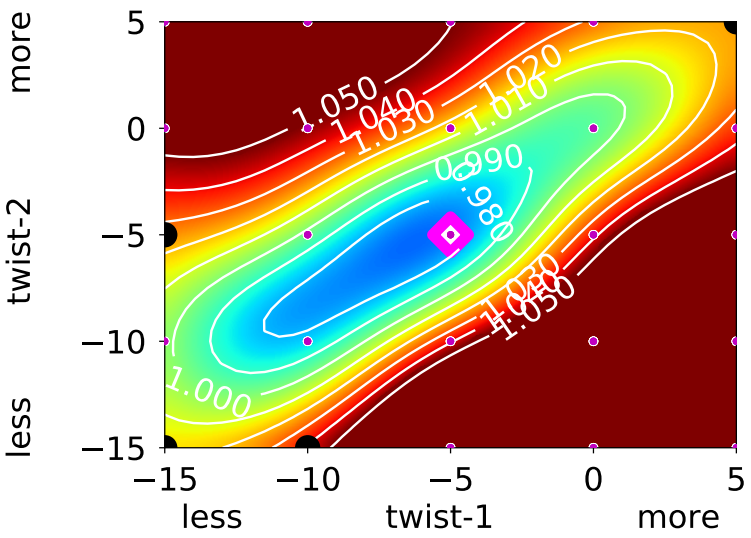

(a) **METAR** - $r/R = 0.80$

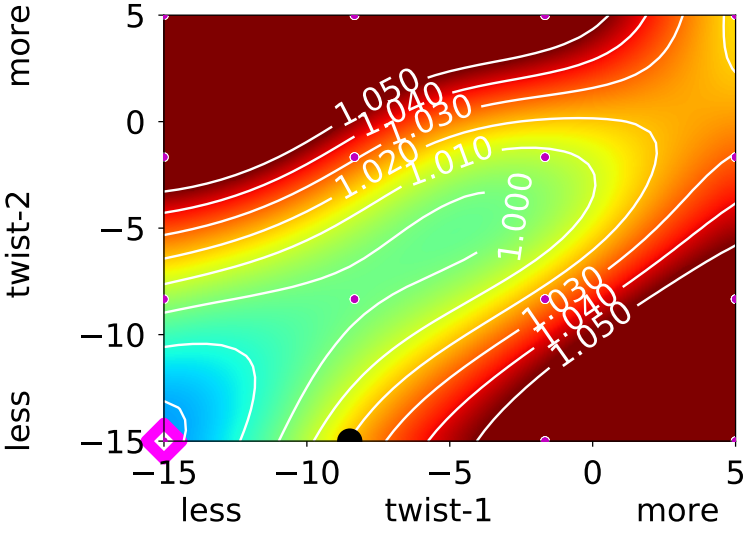

(b) **MESIR** - $r/R = 0.73$

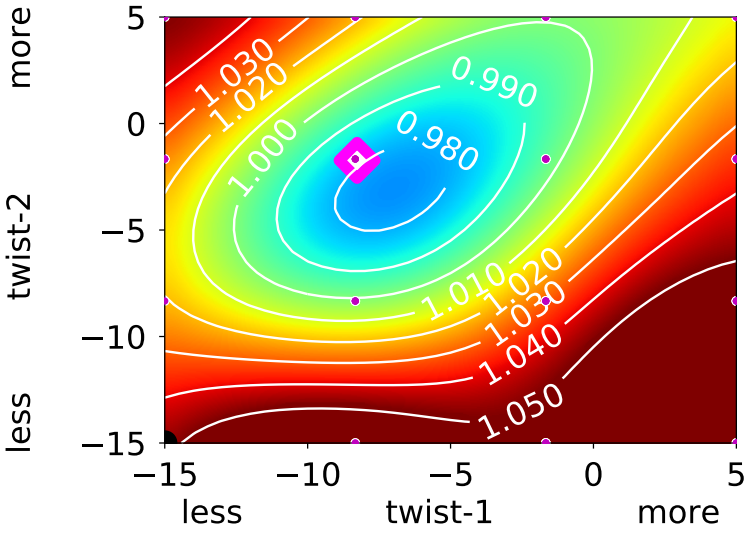

(c) **UPM-METAR** - $r/R = 0.86$

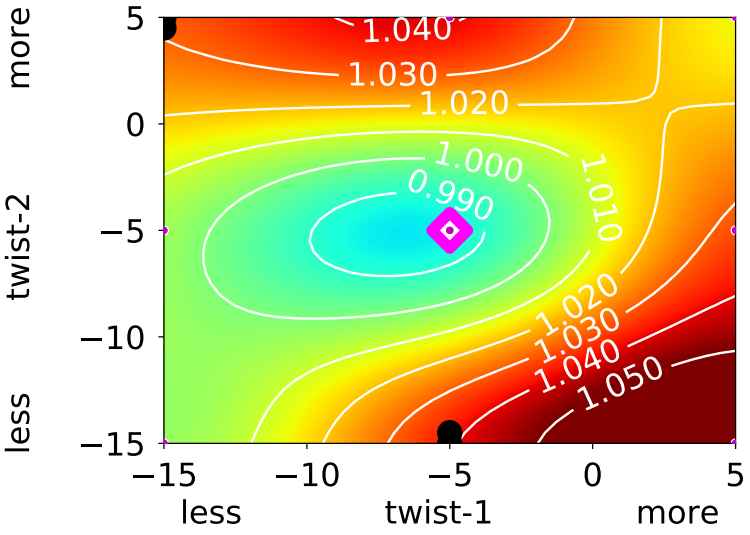

(d) **UPM-BET** - $r/R = 0.60$

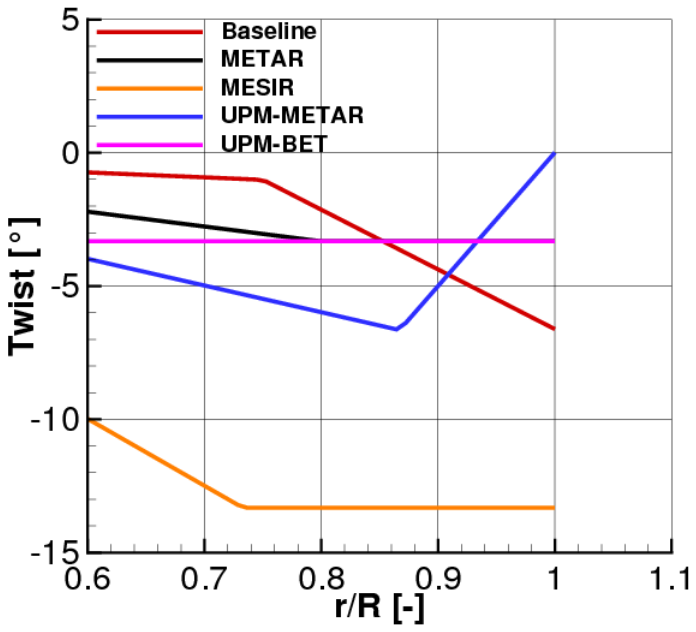

(e) Twist distribution for different optimum

Figure 4.15: Best designs - twist settings and planforms for different methods

Aeroacoustic Analysis of the best Designs

In figure 4.16, the delta noise carpets of the best rotors for the twist study are presented. Their absolute values are depicted in the appendix, in figure A.11.

The difference noise carpet of **METAR** is seen in figure 4.16(a). A noise reduction of 1 to 3 dB is observed on the advancing side of the blade. Inside the rotor disc no change and on the retreating side near $\psi = 300°$ a little increase in noise is predicted.

MESIR, displayed in figure 4.16(b), predicts an overall reduction in noise level of about 3 to 7 dB. The largest reduction is observed at the front from $\psi = 90°$ to $\psi = 270°$. From $\psi = 0°$ to $\psi = 90°$ a small increase in noise is identified. Hence, the noise in the peak is not reduced significantly and it experiences a shift to the lower left corner, seen in figure A.11(b).

UPM-METAR, presented in figure 4.16(c), predicts a constant change in the noise level from $\psi = 270°$ to $\psi = 90°$. Inside the rotor disc, a reduction of up to 3 dB is observed. At the front, a small decrease in the noise level is seen. Outside the rotor disc near $\psi = 300°$ a reduction of up to 5 dB can be seen. This leads to the noise carpet in the appendix, figure A.11(c), where three to four noise peaks from $\psi = 330°$ to $\psi = 90°$ can be observed.

The overall noise level predicted by **UPM-BET**, depicted in figure 4.16(d), is reduced by an amount of 3 to 5 dB, compared to its baseline case. The main reduction up to 7 dB is observed in the center of the rotor disc. From $\psi = 0°$ to $\psi = 270°$ the noise has also been reduced by 1 to 3 dB. On the retreating side, from $\psi = 270°$ to $\psi = 0°$ outside the rotor disc an increase in noise of up to 5 dB is identified. Hence, two to three hotspots with a high amount of spread are observed in the absolute noise carpet in A.11(d).

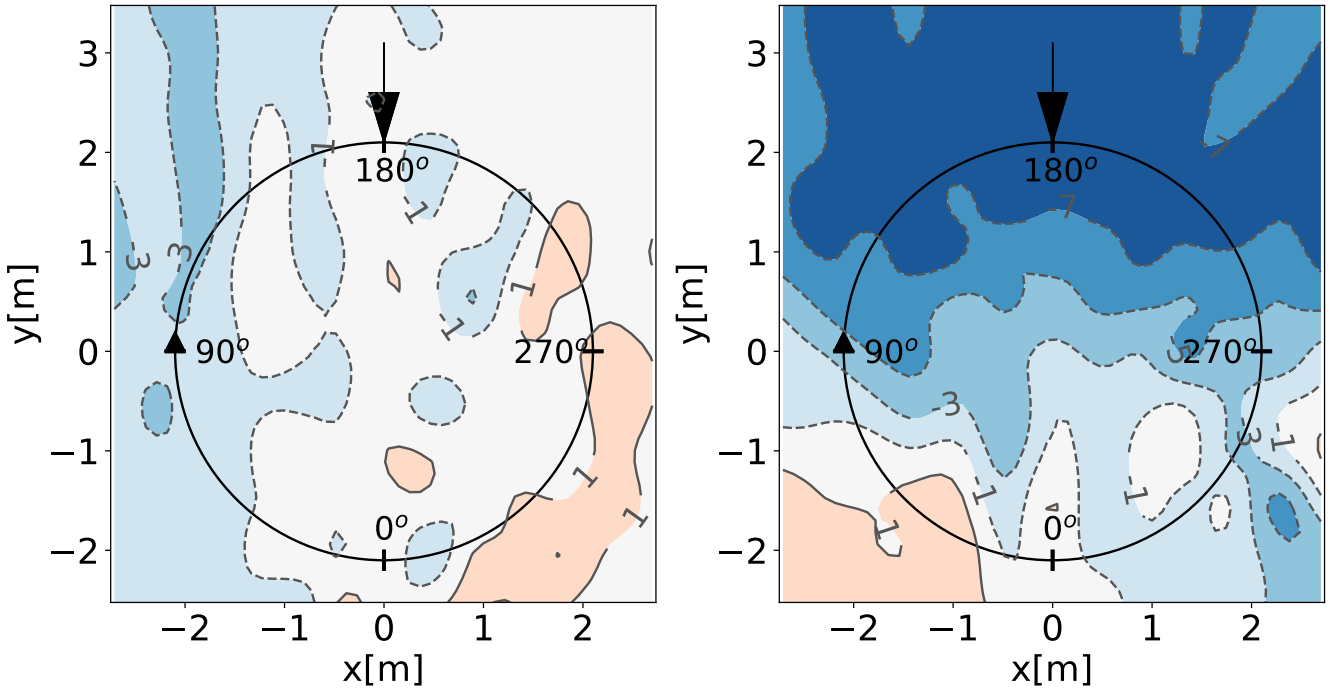

(a) ΔSPL - **METAR**

(b) ΔSPL - **MESIR**

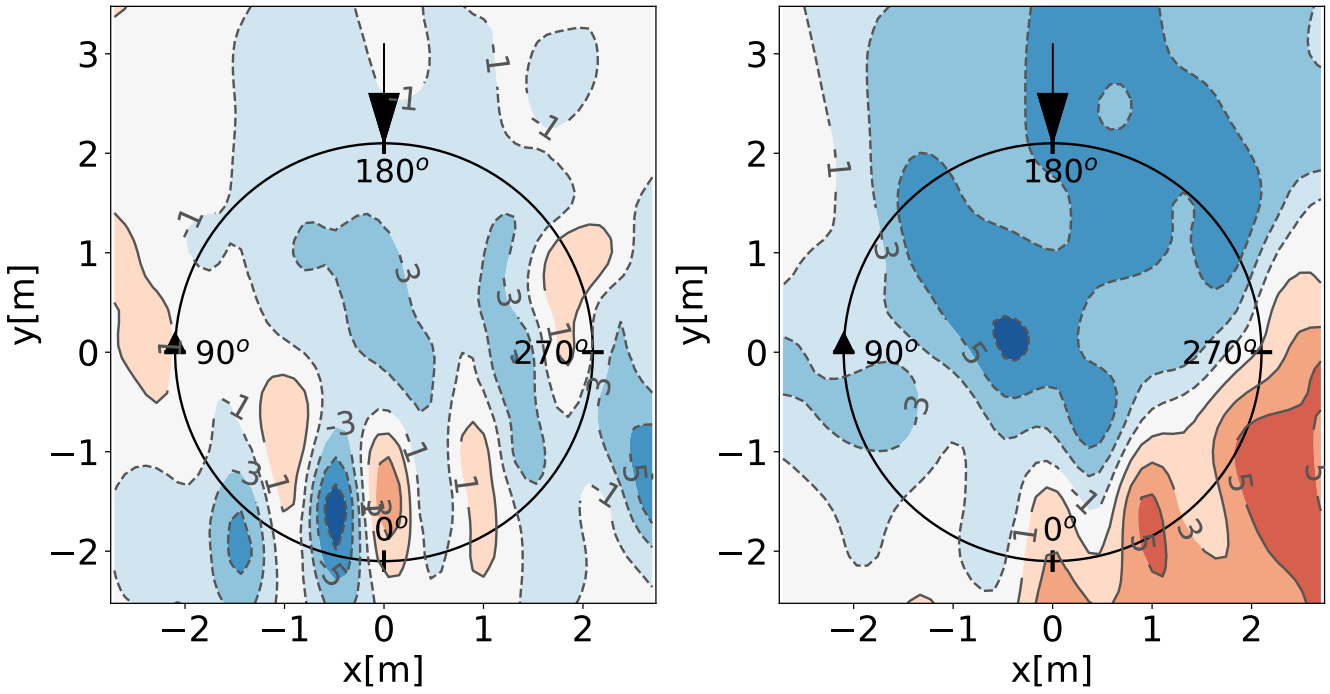

(c) ΔSPL - **UPM-METAR**

(d) ΔSPL - **UPM-BET**

Figure 4.16: Difference SPL [dB] for twist parameterization

Airload Analysis of the best Designs

In figure 4.17, the difference loads and their derivatives are displayed for the best twist results. The absolute airload values are presented in the appendix in figure A.12.

The difference loads for **METAR**, seen in figure 4.17(a), show a large increase in airloads near the tip of the blade on both the advancing and retreating side. Inside the rotor disc, especially near $\psi = 90°$ and at the front, the airloads have been reduced. A change in oscillations can be observed near $\psi = 90°$. Comparing the derivatives, displayed in figure 4.17(b) and the baseline case, the number and amplitudes of oscillations only changed by a small amount. On the front side even more wiggles can be identified. Hence, the noise has not been reduced on the retreating side of the blade, what is observed in the difference noise carpet.

The loads of **MESIR**, depicted in figure 4.17(c), show a large decrease from $\psi = 90°$ to $\psi = 270°$ at the blade tip. Additionally, around $\psi = 0°$ less lift is generated. Yet, more lift is generated near the blade root and a change in oscillations on the advancing and retreating side of the blade near $\psi = 60°$ and $\psi = 300°$ is observed. The number of wiggles, displayed in figure 4.17(d), is smaller compared to the baseline case. Hence, the noise is reduced too. In addition, no oscillations are seen at the front, thus the high noise reduction is achieved. The fluctuations on the retreating and advancing side of the blade from $\psi = 270°$ to $\psi = 90°$ and the directivity of the sound are responsible for the increase in noise in the lower left corner.

UPM-METAR, presented in figure 4.17(e), predicts an increase in airload at the tip of the blade from $r/ = 0.9$ to $r/R = 1.0$. Along the blade and closer to the root, less lift is generated. In addition, a change in oscillations is observed around $\psi = 45°$ and $\psi = 300°$. These changes and even larger and more wiggles, compared to the baseline case are identified in figure 4.17(f). Although the number of fluctuations is increased on the advancing side, their amplitudes have been lowered. Due to the large amount of wiggles, the noise is increased by a small amount. On the retreating side the number of wiggles has been reduced, hence the noise reduction up to 5 dB is achieved.

In figure 4.17(g), which displays the difference loads for **UPM-BET**, a large increase in loads is observed near the blade tip. Less lift is generated near the root of the blade, especially on the advancing side of the blade. A change in oscillations is identified on the advancing and retreating side of the blade near $\psi = 60°$ and $\psi = 300°$. The oscillations are also identified in figure 4.17(h), where the derivatives are displayed. Compared to the baseline case, the amplitudes of the oscillations on the advancing side have been lowered and on the retreating side increased. The large number of fluctuations with small amplitudes from $\psi = 0°$ to $\psi = 135°$ is accountable for noise reduction in that area. However, due to the high amplitudes on the retreating side and the directivity of sound, the noise experiences a significant increase in the lower right corner. Hence, the carpet of maximum noise shows a high spread from $\psi = 300°$ to $\psi = 120°$.

Summarizing the results, changing the twist of the blade reduces the emitted noise. Yet, an increase in noise level is also observed for different methods in different areas. The wake, depicted in figure A.13(f) that displays the wake of **UPM-BET**, shows no significant changes, compared to the baseline case. In addition, no changes as seen for the other parameters can be observed either. Hence the wake is not affected and the noise is not reduced by amounts as seen for the other parameters.

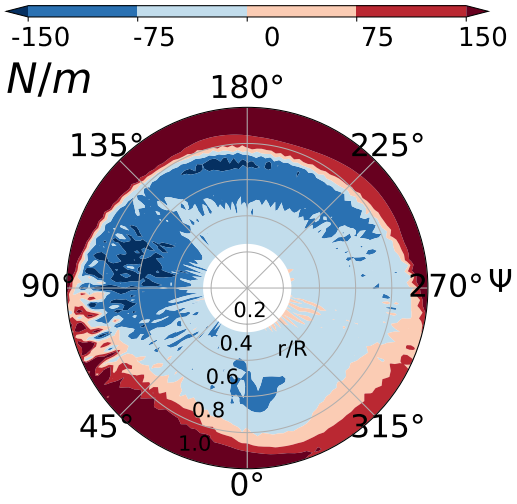

(a) ΔLoads - **METAR**

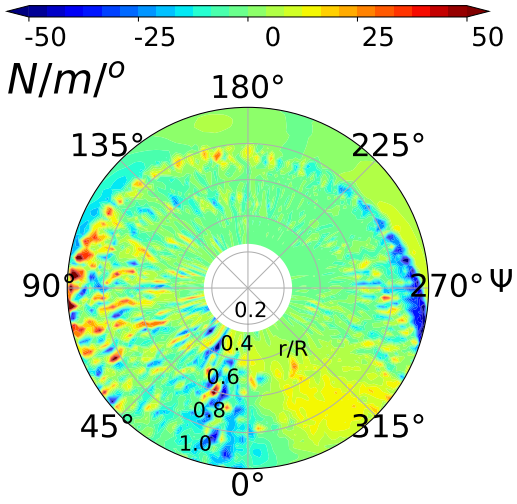

(b) Derivatives - **METAR**

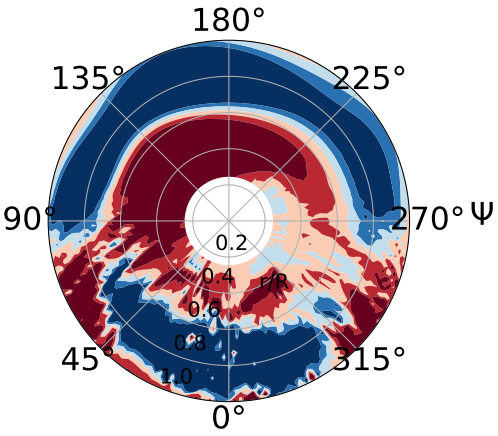

(c) ΔLoads - **MESIR**

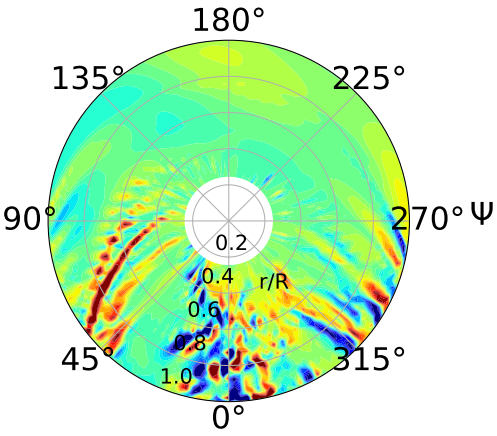

(d) Derivatives - **MESIR**

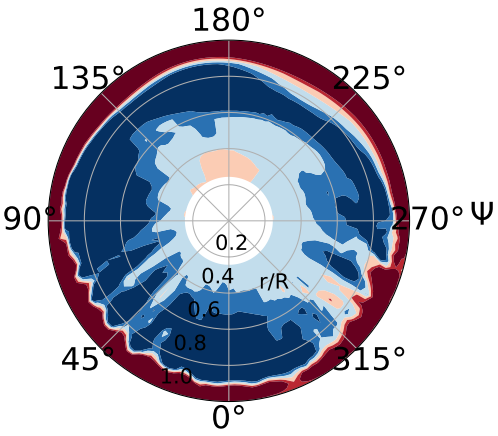

(e) ΔLoads - **UPM-METAR**

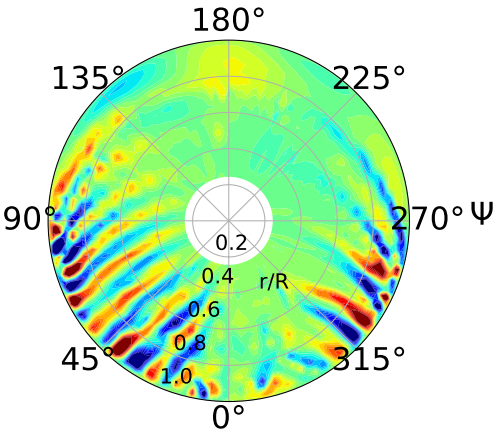

(f) Derivatives - **UPM-METAR**

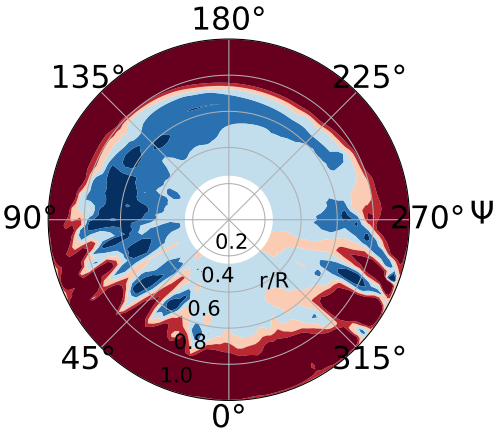

(g) ΔLoads - **UPM-BET**

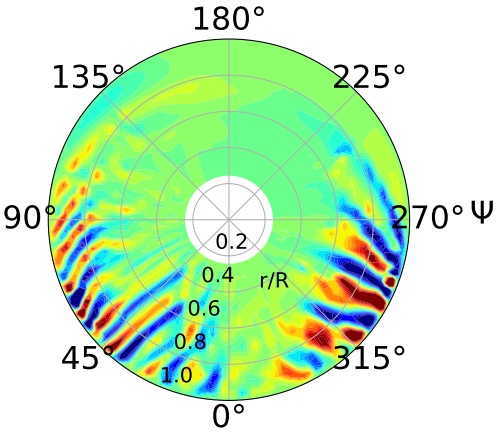

(h) Derivatives - **UPM-BET**

Figure 4.17: ΔLoads and derivatives for twist parameterization

4.4 Review of the Parametric Study

First, it is mentionable that each planform parameter has the capability of reducing BVI-noise. Although noise is reduced, different drawbacks were identified by changing the planform of the blade. As already seen in chapter 3 and in the results of the study of the parameters, the methods differ due to different aerodynamic models and blade discretizations.

Reducing the chord length along the blade is reducing the noise significantly. But, due to the short chord length, less area of the blade contributes to the generation of lift. Hence, less lift is generated at the tip and more is generated near the root of the blade, which leads to a decreased inertia and potential of stall.

Giving the blade some amount of upwards anhedral also reduces the emitted noise. Due to the upward directed tip, the oscillations are focused at the tip and the vortices are set off above the rotor plane, thus the interaction between blades and vortices is reduced.

Sweeping a blade already showed promising results for real helicopters. Comparing the noise carpets with chord and anhedral, sweep also shows beneficial reduction results. The results differ for each method, yet the noise in the peaks is reduced and also the noise outside the rotor disc. The methods used for this study predict two optimal planforms, a backward swept and a backward-forward swept blade. Sweeping the blade has similar drawbacks, like reducing the chord length at the tip. The airloads at the tip are lowered on the advancing side of the blade for the backward swept blades. For the double swept blades the airloads experience a reduction at the tips and an increase along the blade.

Changing the twist of the blade has the least effect on noise reduction in the peaks. Due to the change in twist, the airloads experience a significant change at the tip and along the blade. In addition more, but weaker oscillations occur on the advancing. On the retreating side more and stronger fluctuations occur. Hence, a high amount of spread around the peaks is the result.

Considering the results from chapter 3, the results obtained with **UPM-BET** show good representations of the already investigated rotor blades. In addition, the results for the **7AD** with reduced RPM show no areas with too large or too low amounts of noise. Hence, **UPM-BET** is to be considered as the method with which to perform further investigations and even optimizations on planform parameters.

Chapter 5

Summary and Conclusion

The goal for this thesis was to perform a parametric study on planform parameters with variable fidelity methods. The aim was to identify the influence of each parameter on emitted noise during descent flight state. In this flight state, the helicopter is emitting a high amount of noise caused by blade-vortex-interaction (BVI). It occurs due to the interaction of blades and earlier generated vortices. The vortices are not pushed out of the rotor plane immediately, nor do they convect as quickly as in level flight [14].

In chapter 2 the basics of aeroacoustics and the used Ffowcs-William Hawkings based aeroacoustic code are described. Afterwards, the different methods to calculate the trim, airloads and vortices that are necessary to compute the emitted noise, are presented and compared. The low fidelity methods are based on the blade element theory (BET) [21] and use a prescribed [5] and free wake model [4] to simulate the vortices. In addition, an unsteady panel method (UPM) with the BET is used with a free wake model and is considered as the mid fidelity method [26]. Furthermore, computational fluid dynamics (CFD) [2] utilizing a higher order scheme are used to compute the airloads and vortices. The trim and elastics of the blades are still computed with the BET. The blades are discretized along the quarter chord line when using the BET and as a surface when using panel or CFD methods. Due to the higher level of geometrical representation of the blade, better simulated noise is expected. Afterwards, the major planform parameters, chord length, anhedral, sweep and twist [31], are described and their effects on the aeroacoustics of a helicopter.

In chapter 3 the results of the described methods are compared with already investigated rotor blades: the HARTII, 7AD and ERATO. All methods use the BET to compute the trim of the blade. To compare the aerodynamics of the methods, the settings are the same for all simulations.

The BET in combination with the wake models is not able to give a good representation of the experiments. The more advanced the planform of the blades is, the more differences in terms of trim angles and noise carpets are observed.

The trimmed UPM simulations with prescribed wake as well as the BET, matches better the experiments. But, these are dependent on the blade design. For the HARTII blade good results are observed, yet the other blades show larger offsets in loads and noise carpets.

Although CFD is considered as a high fidelity method, the results are dependent on the number of grid cells and the time stepsize. The noise is predicted too low and the amplitudes for the oscillations in the respective airloads are too little. The trim results show the closest agreement to the measured trim angles compared to the other methods. Summarizing the CFD results, they show a coarse representation of the experiments.

Reviewing the results, the BET with its wake models and UPM in combination with the BET and the prescribed wake model are taken to perform the parametric study. Due to the high amount

of time needed, CFD simulations are not included in the study.

The parametric study, presented in chapter 4 is performed on the 7AD rotor blade with reduced revolutions per minute (RPM) and experimental flight settings of the ERATO blade. Due to the reduction in RPM a first reduction in noise is given.

For the study, the parameters are changed individually with different locations along the blade. The effect of each parameter has been investigated. The noise characteristics of each configuration are displayed via landscape plots. Additionally noise carpets, difference airloads and their derivatives are discussed for the best design, simulated by each method.

Reducing the chord length of the blade has a beneficial effect in reducing the noise. Especially when the smaller chord length is closer to the root of the blade, a significant reduction in noise is observed. A drawback of shortening the chord length along the blade is less lift production at the tip, thus a decreased inertia.

Anhedral has the capability to reduce BVI-noise too. Each method predicts a different blade design, yet nearly all have an upward directed tip in common. The strength and position of the vortices is near the tip of the blade, what is observed in the respective derivatives of the airloads. Due to reduced strength and an offset of the vortices, the oncoming blades may not hit the full vortex and therefore reduce BVI-noise.

Sweeping the blade showed different effects between the used methods. The wake models with the BET predict backward swept blades as best configurations. The noise is reduced, yet less lift is produced on the advancing side of the blades. The panel methods predict a backward-forward swept combination of the blade tip. Although the noise in the peaks and outside the rotor plane is reduced by a significant amount, the loss of lift at the tip is even higher compared to the backward swept blades.

The parameter twist reduces the noise, yet the reduction in the peaks is lower compared to the other parameters and the spread around the peaks is increased. By changing the twist, the strength of the oscillations is reduced but more occur. Due to the high number of fluctuations the spreading is explained and through the different twist at the tip the changed strength of the vortices.

The review of this study is that each planform parameter has the capability of reducing the emitted noise, yet twist shows the least promising results. Each parameter need to be changed carefully, because each change in planform affect the emitted vortices, the airloads and the trim of the rotor blade. For further investigation or even optimization, UPM coupled with the BET is recommended. Its results are the most promising and the needed resources are acceptable, compared to the different rotor blades and methods.

Yet, due to the contradictory results of the methods, further investigation and validation is necessary. Either windtunnel experiments or full blown CFD may be used to investigate specific blade designs taken from the parametric study. It is also possible to perform low and mid fidelity optimizations first. Afterwards, these results can be validated using high fidelity methods with a sufficient grid size or windtunnel experiments.

In this thesis, the parameter anhedral did show promising results. Hence, it may be beneficial to further investigate its influence on emitted noise. Eventually an advanced wing tip design like winglets is the future of low noise rotorcraft design.

Bibliography

[1] Jianping Yin, Martin Kuntz and Jan Delfs: Prediction of Acoustic Far Field with DLR's Acoustic Code APSIM. In: *APSIM manual for version 7.0* (2008)

[2] Aumann P. Bartelheimer et al.: Flower installation and use handbook, release 116. In: *Technical report, German Aerospace center (DLR)* (2008)

[3] Bernard Benoit, A.-M. Dequinm K. Kampa, W. von Grünhagen, P.-M. Basset and Gimonet: HOST, a Genereal Helicopter Simulation Tool for Germany and France. In: *American Helicopter Society 56th Annual Forum, Virignia Beach, Virginia* (2000)

[4] Bertrand Michea and Jacques Chauvin: *Etude des sillages de rotors d'helicoptere en vol d'avancement et de leur influence sur les performances du rotor*, Université Pierre et Marie Curie (Paris), Dissertation, 1992

[5] G. Arnaud, B. Benoit and F. Toulmay: Improvements to the Aerodynamic Model of the R85 Helicopter Rotor Code Validation and Applications. In: 28^{th} *ISl Applied Aerodynamics Symposium* (1991)

[6] Jianping Yin: DLR Free Wake Unsteady Panel Method (UPM) User Handbook for Application of the Rotors. In: *Report of the Institute of Aerodynamics and Flow Technology* (2011)

[7] G. Heilers: *Aerodynamische Mehrpunktoptimierung von Rotorblättern mit reibungsfreien Strömungssimulationen*, IAG Stuttgart, Mastersthesis, 2014

[8] Fredric H. Schmitz: The Challenges and Possibilities of a Truly Quiet Helicopter, 29th Alexander A Nikolsky Honorary Lecture. In: *Journal of the American Helicopter Society 61, 041001* (2016)

[9] Kenneth S Brentner and F.Farassat: Modeling aerodynamically generated sound of helicopter rotors. In: *Progress in Aerospace Sciences 39* (2003)

[10] Berend G. van der Wall, Christoph Kessler, Yves Delrieux, Philippe Beaumier, Marc, Gervais, Jean-Francois Hirsch, Kurt Pengel and Pascal Crozier: From ERATO Basic Research to the Blue Edge Rotor Blade. In: *AHS 72nd Annual Forum, West Palm Beach Florida* (2016)

[11] A. Brocklehurst and G.N. Barakos: A review of helicopter rotor blade tip shapes. In: *Progress in Aerospace science 56* (2012)

[12] Ulrich Kowarsch, Constantin Öhrle, Manuel Keßler: Aeroacoustic Simulation of a Complete H145 Helicopter in Descent Flight. In: *Journal of the American Helicopter Society 61, 042001* (2016)

[13] Marius Bebesel, Günther Polz and Eberhard Schöll: Aerodynamic and Aeroacoustic Layout of the ATR (Advanced Technology Rotor). In: *Presented at the American Helicopter Society 55th Annual Forum, Montreal, Canada* (1999)

[14] Jianping Yin, Berend G. van der Wall and Gunther A. Wilke: Investigation of a simplified aerodynamic modelling technique for noise predictions using FW-H propagation. (2016)

[15] J. Delfs: Lecture: Basic of Aeroacoustics. (2015)

[16] Kenneth S. Brentner, Anastasios S. Lyrintskis, Evangelos K. Koutsavdis: Comparison of Computational Aeroacoustic Prediction Methods for Transonic Rotor Noise. In: *Journal of Aircraft No.34* (1997)

[17] K. S. Brentner: Helicopter Rotor Noise Prediction: Background, Current Status and Future Direction. 1997. – Forschungsbericht

[18] J. Delfs: Lecture: Methoden der Aeroakustik. (2015)

[19] Christopher C Hennes and Kenneth S. Brentner: The Effect of Blade Deformation on Rotorcraft Acoustics. In: *31st European Rotorcraft Forum, Florecne, Italy* (2005)

[20] Donald L. Kunz: Comprehensive Rotorcraft Analysis: Past, Present and Future. In: *Structures, Structural Dynamics & Materials Conference, Austin, Texas* (2005)

[21] S. Drzewieki: Théorie générale de l'hélice. In: *Paris: Gauthier-Villars* (1920)

[22] Raymond W. Prouty: *Helicopter Performance, Stability, and Control.* R.E. Krieger Publishing Company, 1986

[23] Walter Bittner: *Flugmechanik der Hubschrauber.* Springer-Verlag Berlin Heidelberg, 2005

[24] Lothar Bertsch: Lecture: Fluglärm. (2015)

[25] *https://www.hindawi.com/journals/aav/2012/402130/fig2/.* 2017

[26] J.P.Yin and S.R.Ahmed: Treatment of unsteady rotor aerodynamics using a 3-d panel method. In: *Technical report, Deutsche Forschungsanstalt für Luft- und Raumfahrt Forschungsbereich Strömungsmechanik* (1994)

[27] Gunther Wilke: Comparison of Higher-Order CFD Modelling with an Unsteady Panel Method. In: *17th ONERA-DLR Aerospace Symposium, ONERA Modane-Avrieux Center* (2017)

[28] Antony Jameson, Wolfgang Schmidt and Eli Turkel: Numerical Solution of the Euler Equations by Finite Volume Methods Using Runge-Kutta Time-Stepping Schemes. In: *American Institute of Aeronautics and Astronautics Paper 1981 - 1259* (1981)

[29] Sanjiva K. Lele: Compact Finite Difference Schemes with Spectral-like Resolution. (1991)

[30] Markus Dietz, Walid Khier, Björn Knutzen: Numerical Simulations of a Full Helicopter Configuration Using Weak Fluid-Structure Coupling. In: *46th AIAA Aerospace Sciences Meeting and Exhibit, Reno, Nevada* (2008)

[31] Gunther Wilke: Variable Fidelity Optimization of Required Power of Rotor Blades: Investigation of Aerodynamic Modles and their Application. In: *38th European Rotorcraft Forum* (2012)

[32] A. Gessow: Effect of a Rotor-Blade Twist and Plan-Form Taper on Helicopter Hovering Performance / NACA Technical Notice 1542. In: *National Advisory Commitee for Aeronautics Collection* (1948)

[33] M. Hollands, M. Kessler and E.Krämer: Influende of An-/Dihedral and of Different Blade-Shapes on Performance and Aeroacoustics of an Isolated Rotor. In: *38th European Rotorcraft Forum* (2012)

[34] M. Imiela: *Mehrpunktoptimierung eines Hubschrauberrotors im Schwebe- und Vorwärtsflug unter Berücksichtigung der Fluid-Struktur-Wechselwirkung*, Institut für Aerodynamik und Strömungstechnik, DLR, Braunschweig, Dissertation, 2012

[35] Bereng G. van der Wall, Joon W. Lim, Marilyn J. Smith, Sung N. Jung, Joelle Bailly, James D. Baeder, D. Douglas Boyd, Jr.: An Assessment of Comprehensive Code Prediction State-of-the-Art Using the HART II International Workshop Data. In: *AHS International 68th Annual Forum & Technology Display, Ft. Worth, TX* (2012)

[36] W. R. Splettstoesser, K.-J. Schulz and H.Bucholz: ERATO Rotor Validation Test in DNW - Documentation and Representative Results / DLR - Institut für Entwurfsaerodynamik. 1999. – Forschungsbericht

Appendix A

Additional Visualizations

A.1 Trim Results of used Methods for different Rotor Blades

The following figures A.1, A.2(a) and A.2(b) below, display another visualization for the trim angles of the results for the different rotor blades, in chapter 3.

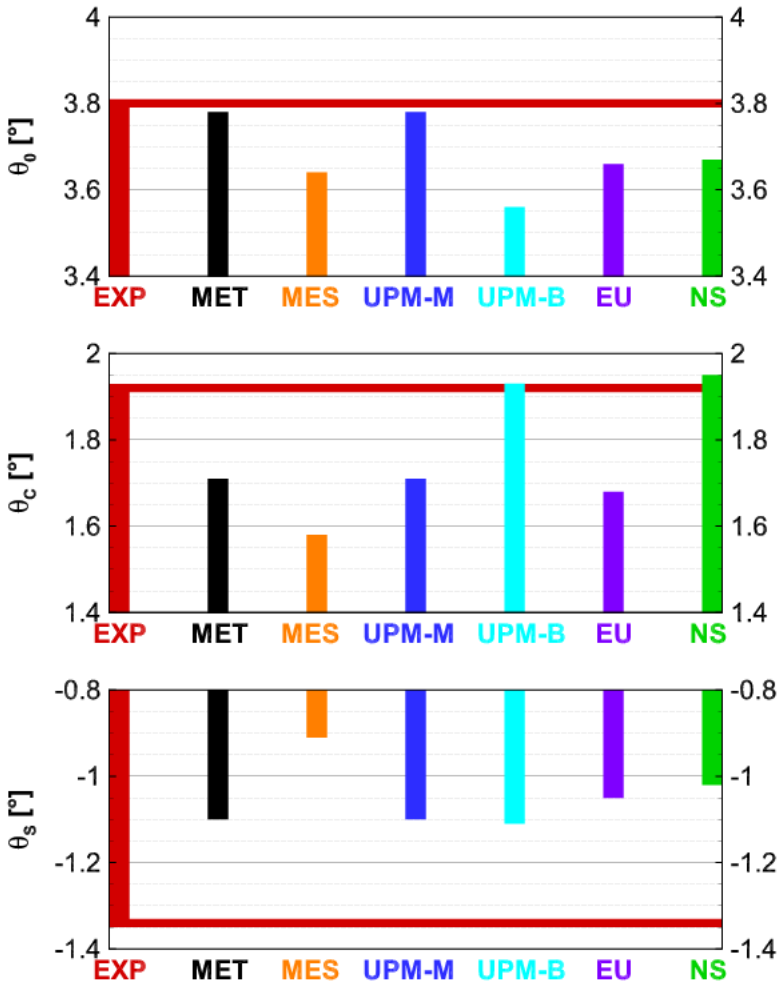

Figure A.1: HARTII trim diagram, legend: EXP - Experiment, MET - **METAR**, MES - **MESIR**, UPM-M - **UPM-METAR**, UPM-B - **UPM-BET**

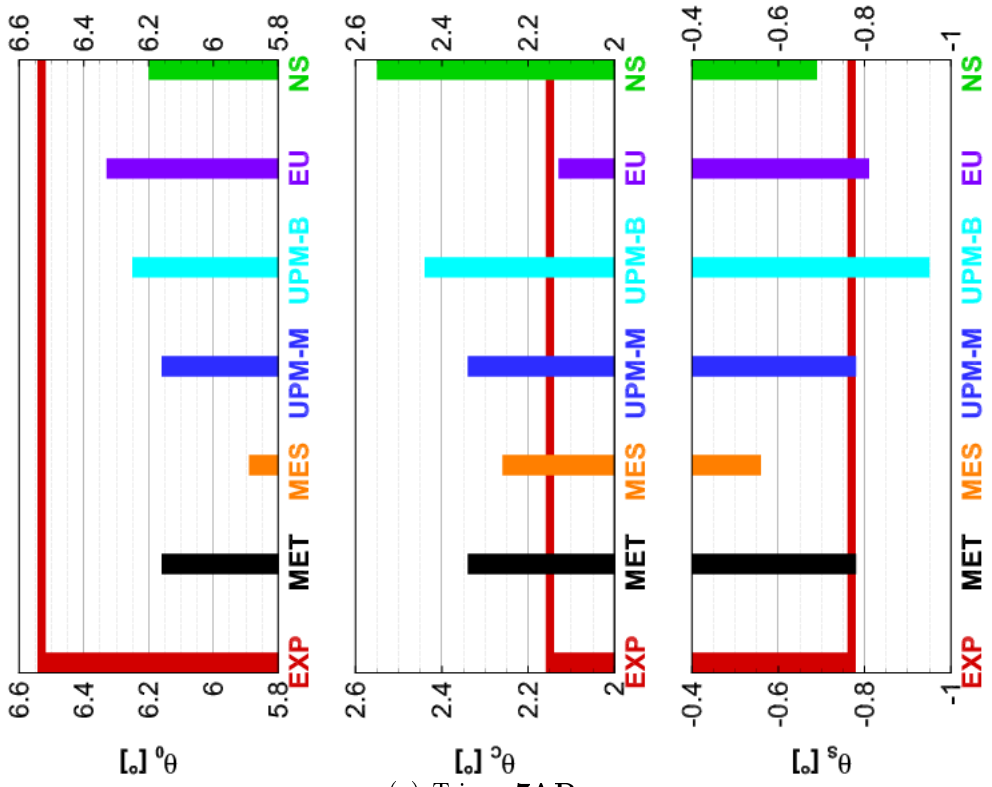

(a) Trim - **7AD**

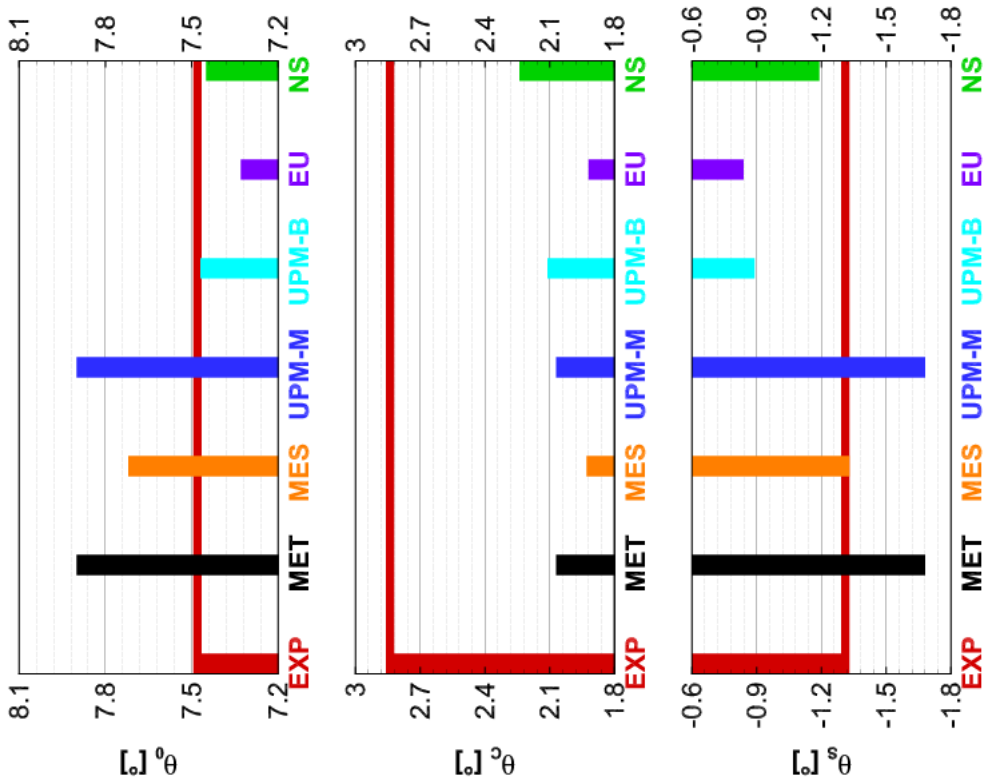

(b) Trim - **ERATO**

Figure A.2: Trim diagram **7AD** and **ERATO**, legend: EXP - Experiment, MET - **METAR**, MES - **MESIR**, UPM-M - **UPM-METAR**, UPM-B - **UPM-BET**

A.2 Difference Plots of the 7AD blade with reduced RPM

The folloing figure A.3, displays the difference SPL plots for the **7AD** with reduced RPM. Figure A.4, represents the respective difference loads for the different methods for the **7AD** with reduced RPM.

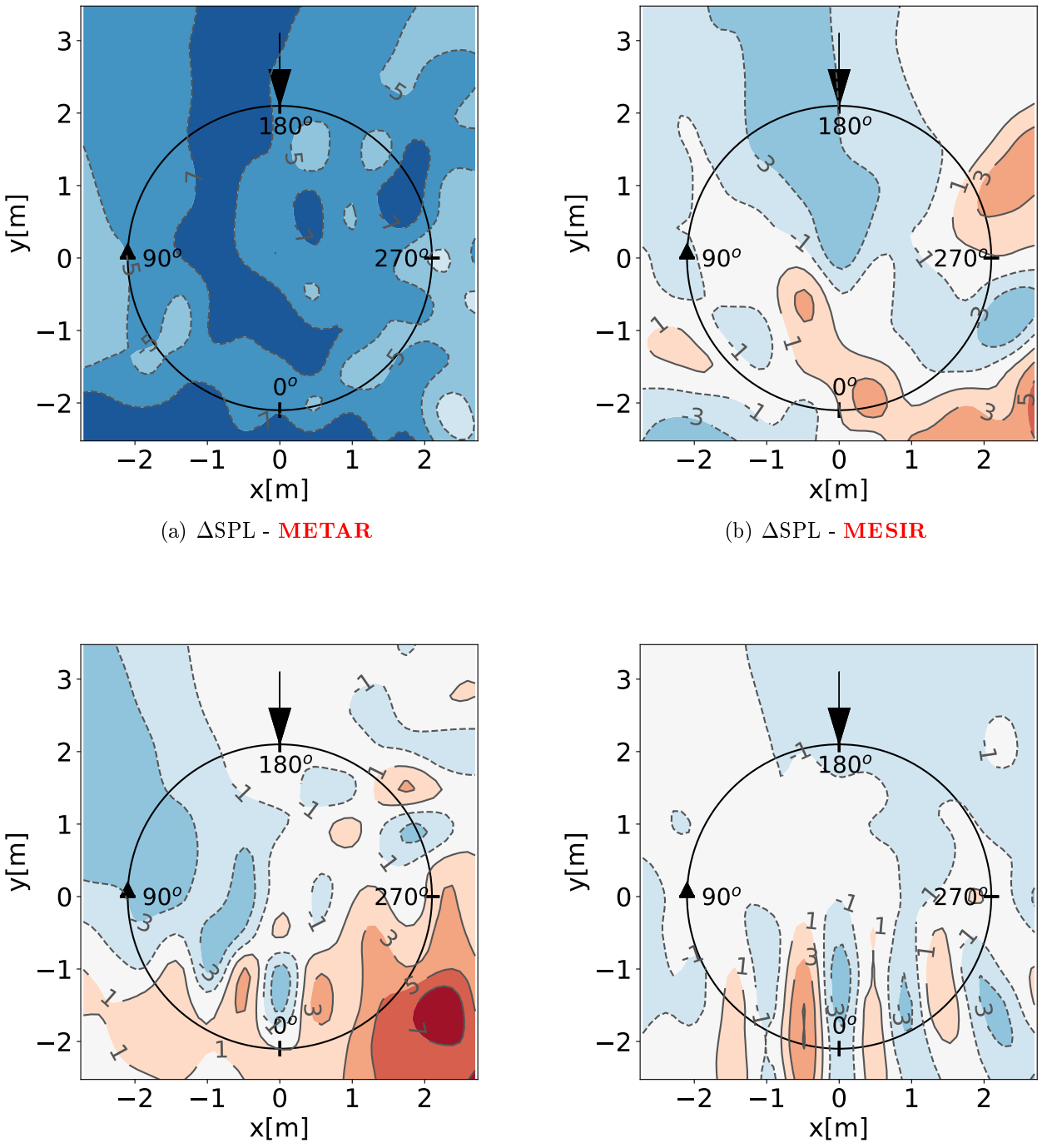

(a) ΔSPL - **METAR**

(b) ΔSPL - **MESIR**

(c) ΔSPL - **UPM-METAR**

(d) ΔSPL - **UPM-BET**

Figure A.3: ΔSPL [dB] for **7AD** with reduced RPM

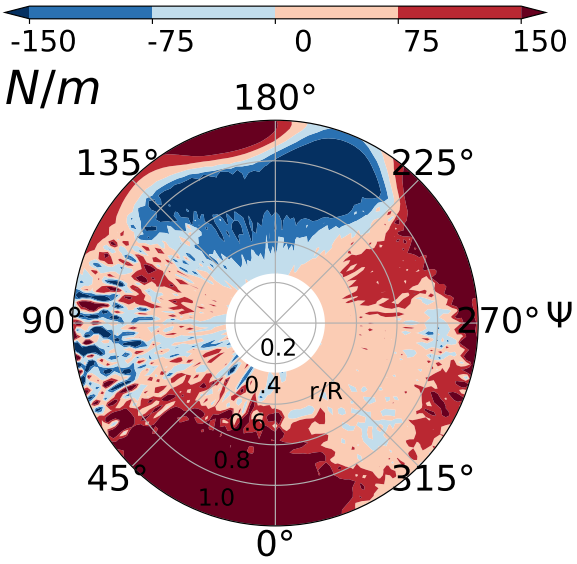

(a) ΔLoads - **METAR**

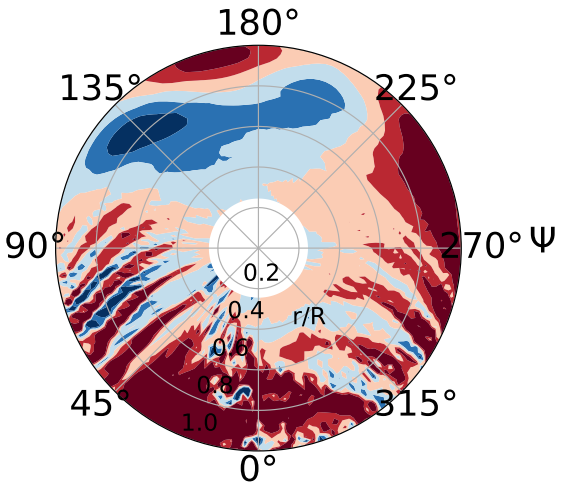

(b) ΔLloads - **MESIR**

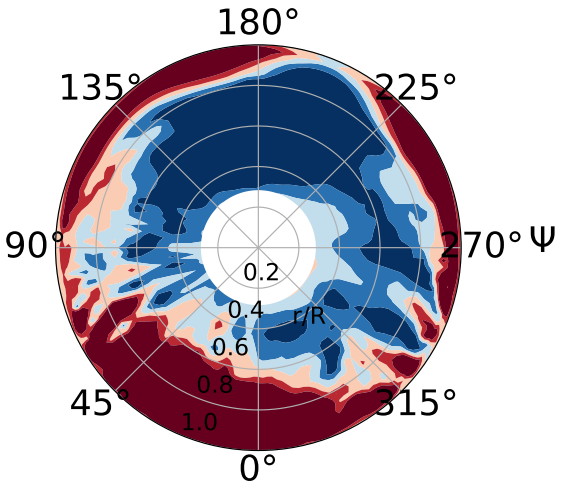

(c) ΔLoads - **UPM-METAR**

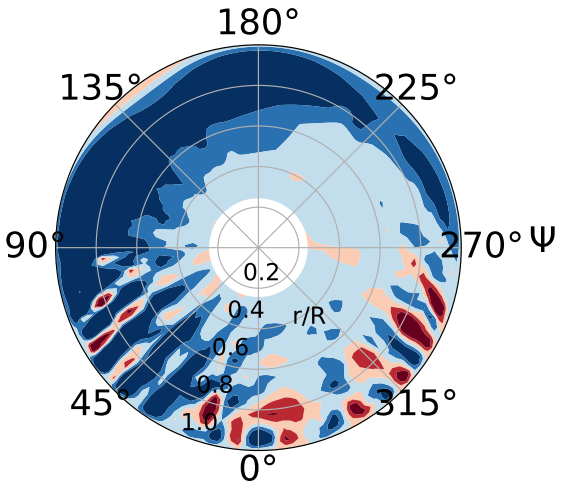

(d) ΔLoads - **UPM-BET**

Figure A.4: ΔLoads for **7AD** with reudced RPM

A.3 Absolute Noise Carpets and Loads of the Parametric Study Results

The following figures display the absolute values for SPL [dB] and loads for the different parameters investigated with variable fidelity methods.

A.3.1 Chord

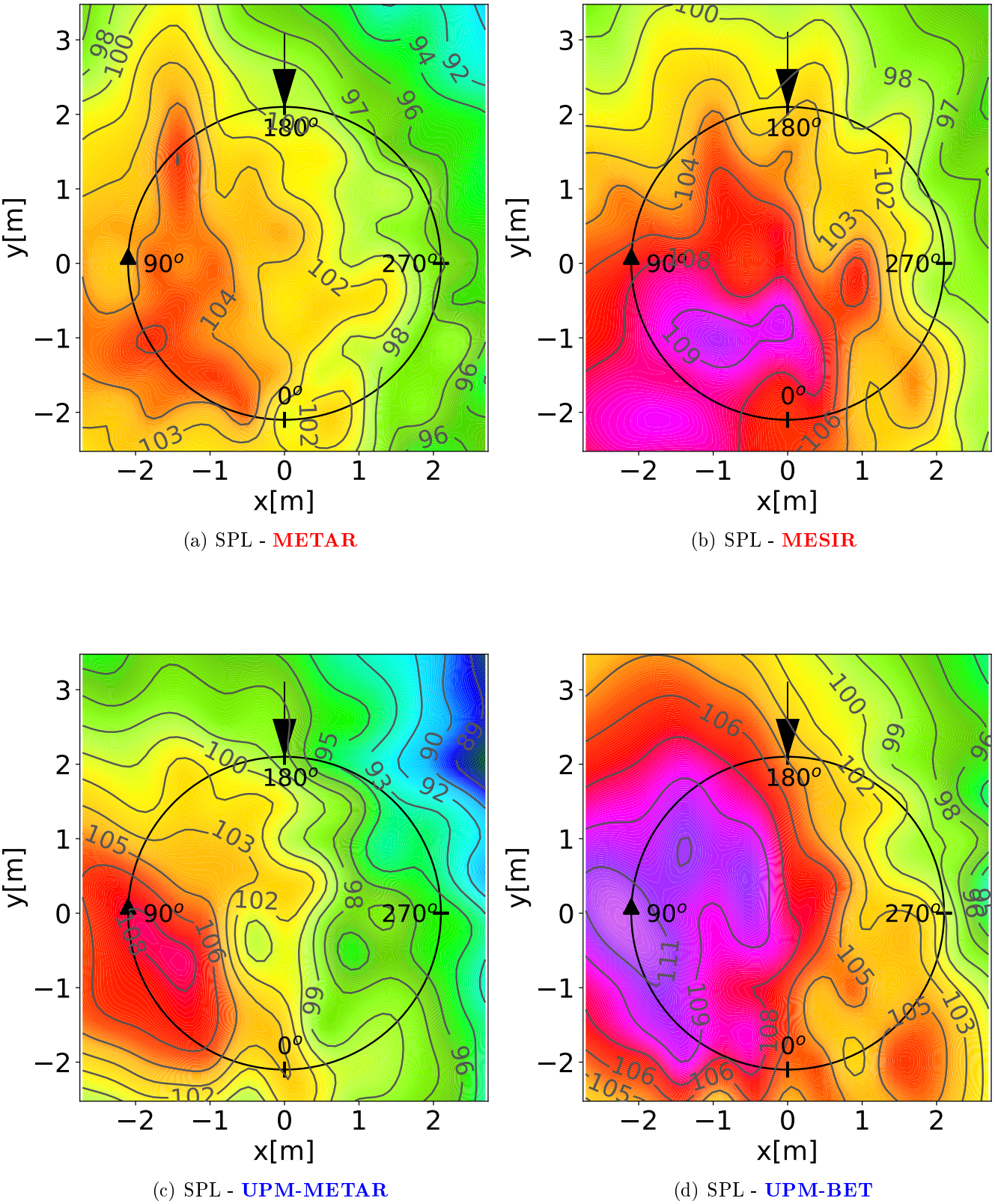

(a) SPL - **METAR**

(b) SPL - **MESIR**

(c) SPL - **UPM-METAR**

(d) SPL - **UPM-BET**

Figure A.5: Best design SPL [dB] for chord parameterization

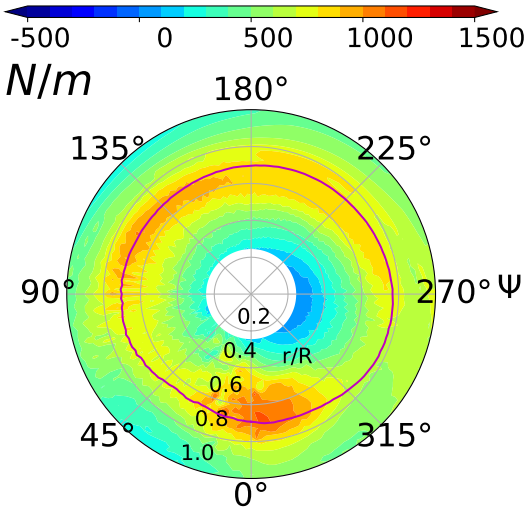

(a) Loads - **METAR**

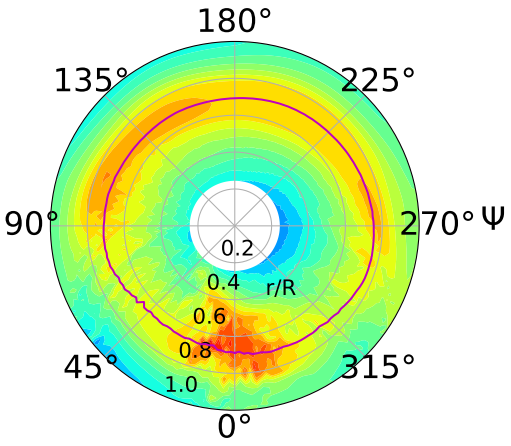

(b) Loads - **MESIR**

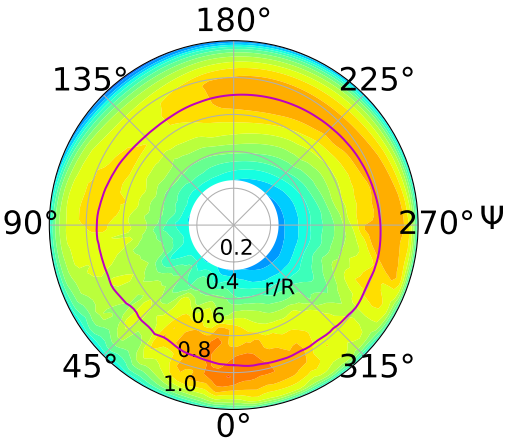

(c) Loads - **UPM-METAR**

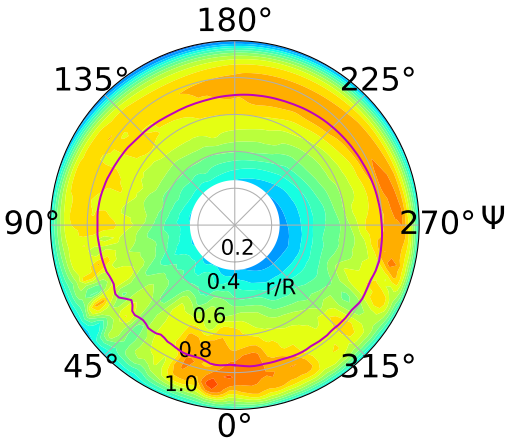

(d) Loads - **UPM-BET**

Figure A.6: Best design loads for chord parameterization

A.3.2 Anhedral

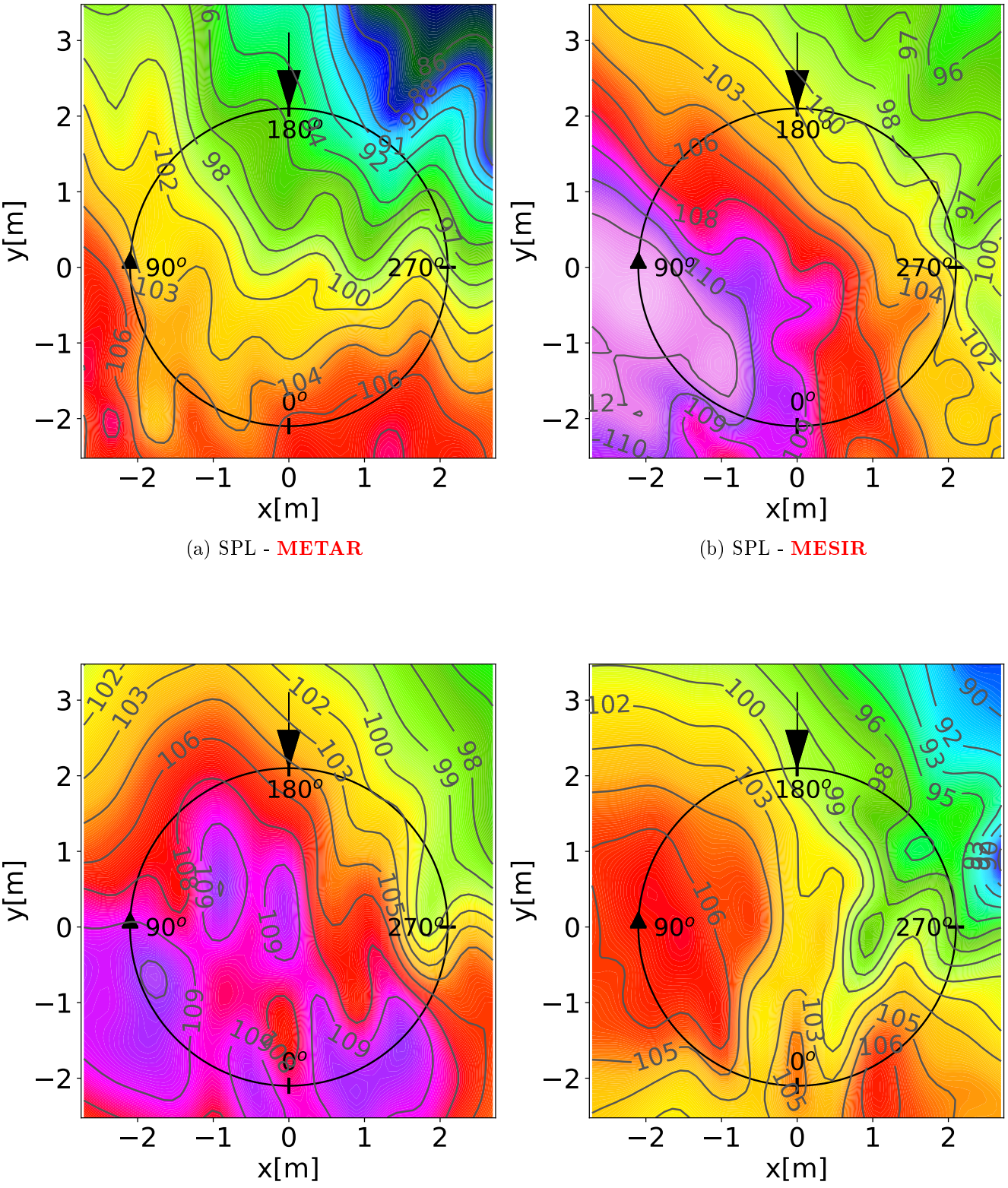

(a) SPL - **METAR**

(b) SPL - **MESIR**

(c) SPL - **UPM-METAR**

(d) SPL - **UPM-BET**

Figure A.7: Best design SPL [dB] for anhedral parameterization

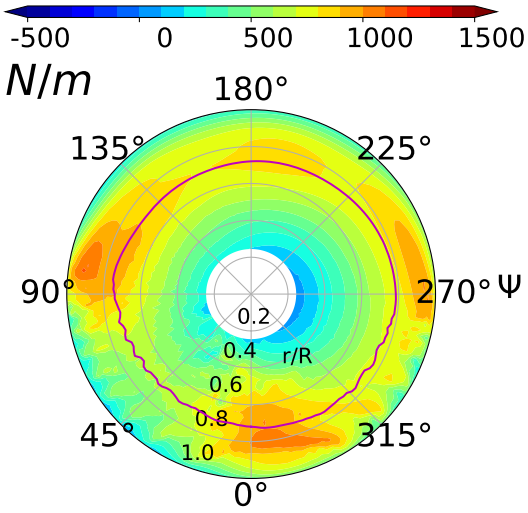

(a) Loads - **METAR**

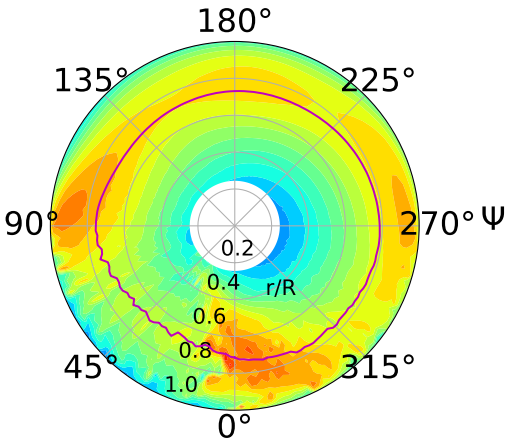

(b) Loads - **MESIR**

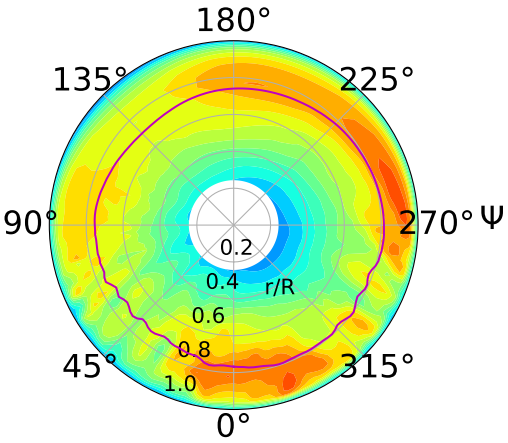

(c) Loads - **UPM-METAR**

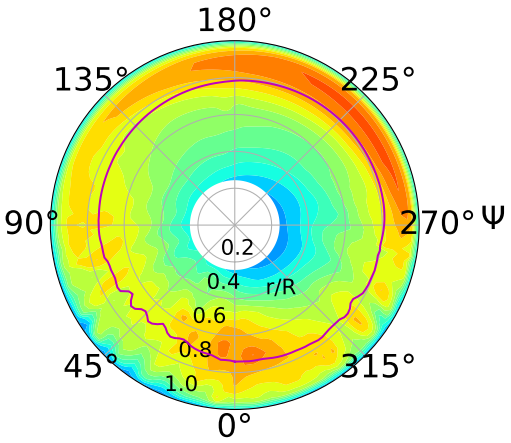

(d) Loads - **UPM-BET**

Figure A.8: Best design loads for anhedral parameterization

A.3.3 Sweep

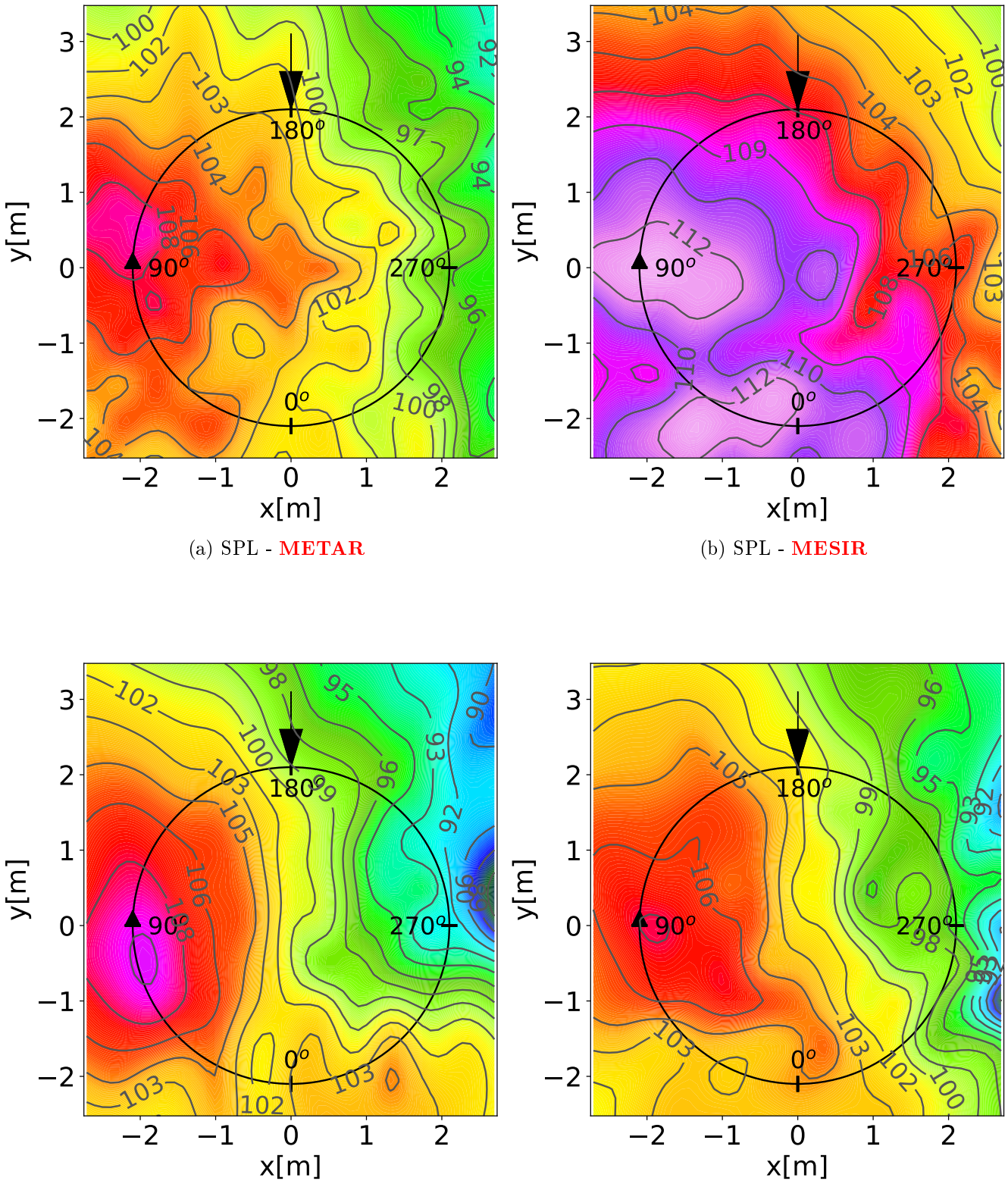

(a) SPL - **METAR**

(b) SPL - **MESIR**

(c) SPL - **UPM-METAR**

(d) SPL - **UPM-BET**

Figure A.9: Best design SPL [dB] for sweep parameterization

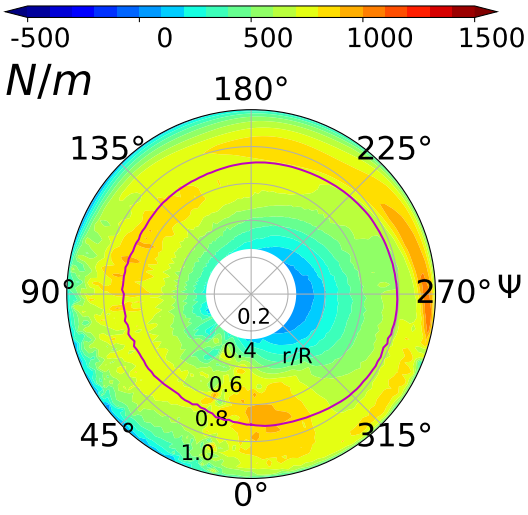

(a) Loads - **METAR**

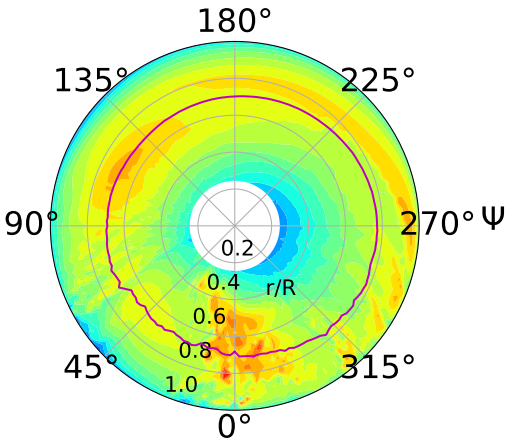

(b) Loads - **MESIR**

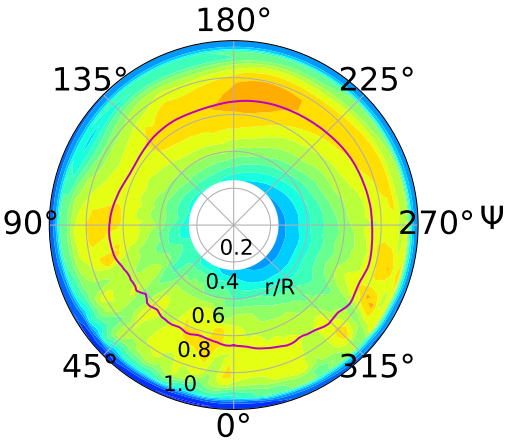

(c) Loads - **UPM-METAR**

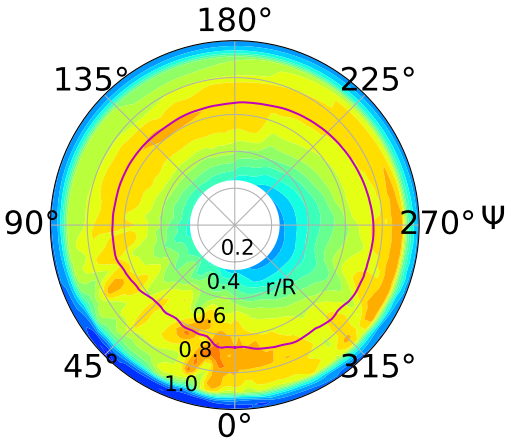

(d) Loads - **UPM-BET**

Figure A.10: Best design loads for Sweep parameterization

A.3.4 Twist

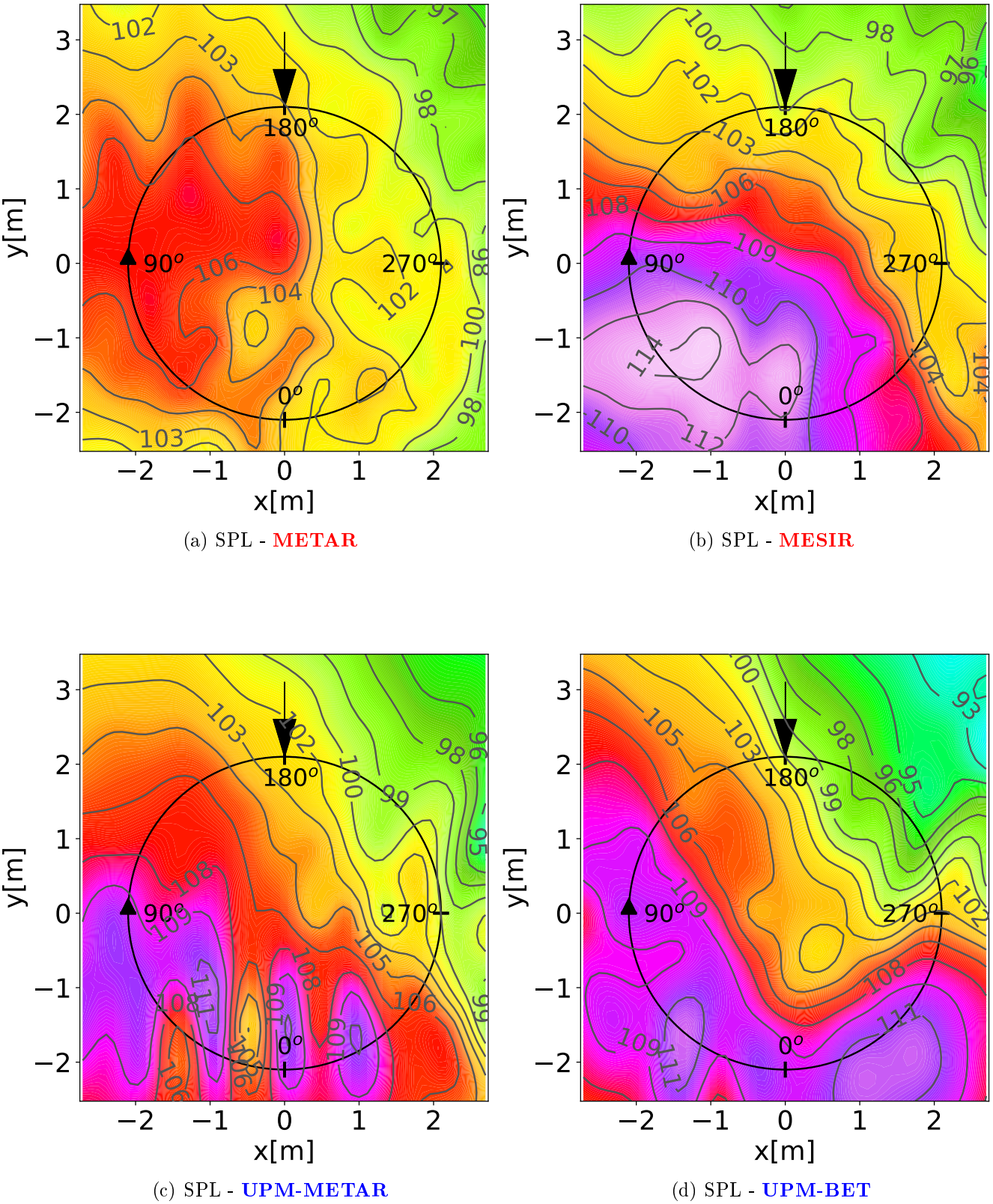

(a) SPL - **METAR**

(b) SPL - **MESIR**

(c) SPL - **UPM-METAR**

(d) SPL - **UPM-BET**

Figure A.11: Best design SPL [dB] for twist parameterization

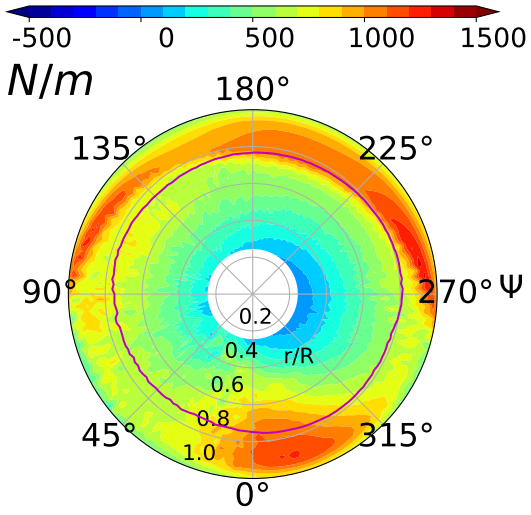

(a) Loads - **METAR**

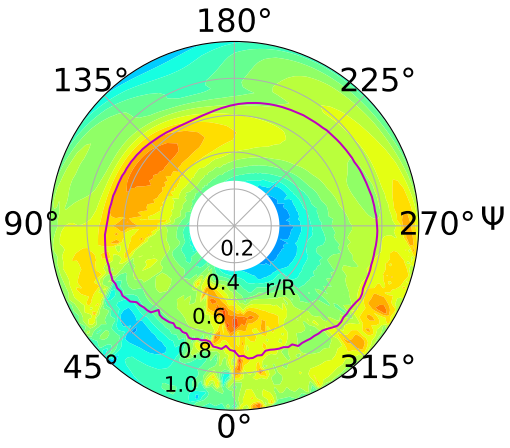

(b) Loads - **MESIR**

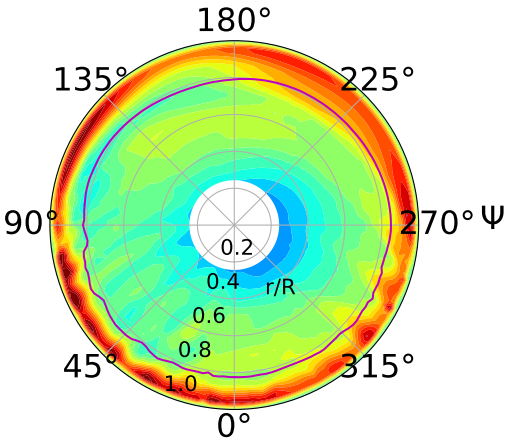

(c) Loads - **UPM-METAR**

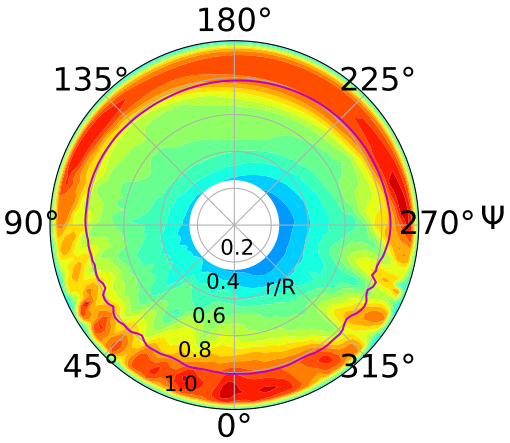

(d) Loads - **UPM-BET**

Figure A.12: Best design loads for twist parameterization

A.4 Wake Visualization of Baselines and best Designs from UPM-BET

In figure A.13, the wakes for the **7AD**, the baseline for the parametric study and from **UPM-BET** are displayed. Displayed is the height of the vortices, so that the effect of each parameter can be analyzed. The planform changes in figures A.13(c), A.13(d) and A.13(e), show that the wake is directly affected. The vortices are larger, compared to the baseline case and especially for anhedral, the wake is set off above the rotor plane.

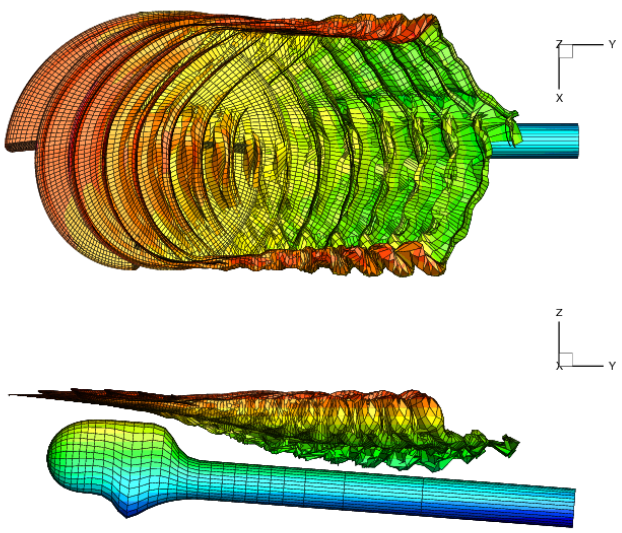

(a) Wake - Study - 7AD

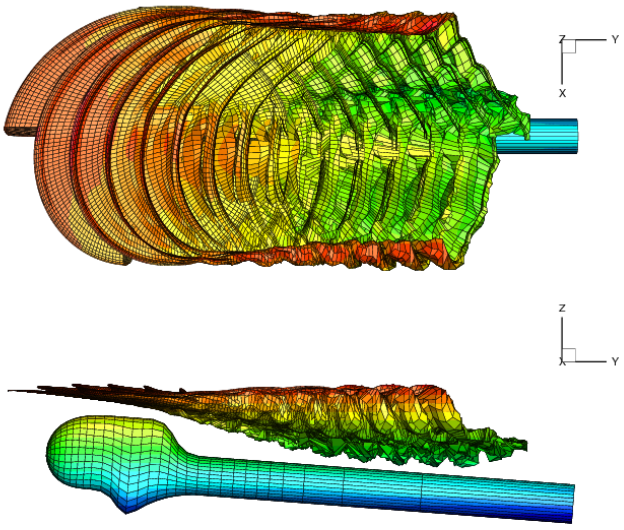

(b) Wake - Baseline

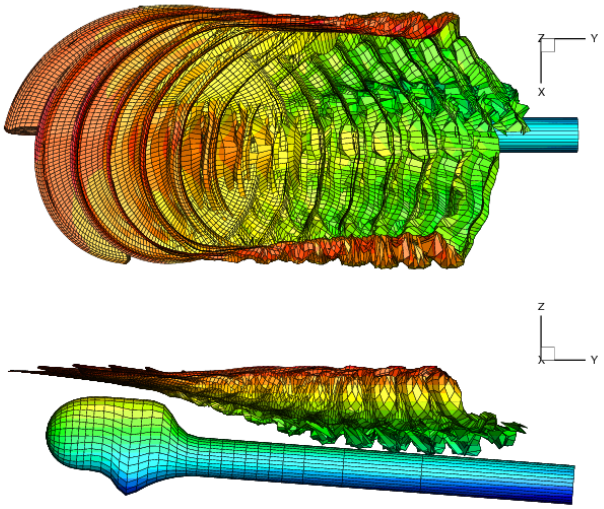

(c) Wake - Chord

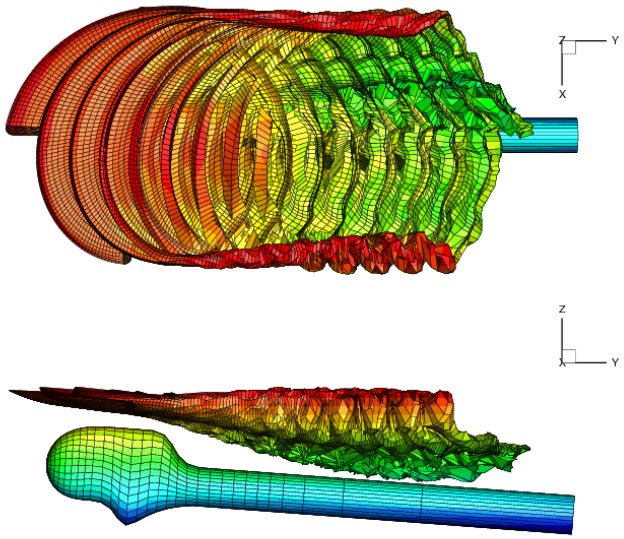

(d) Wake - Anhedral

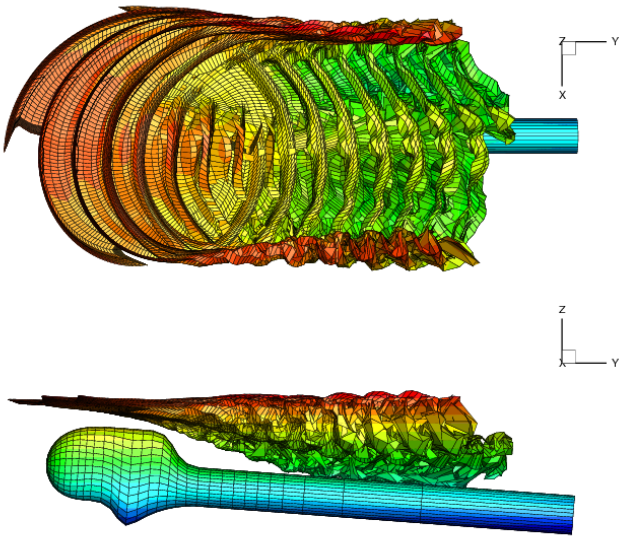

(e) Wake - Sweep

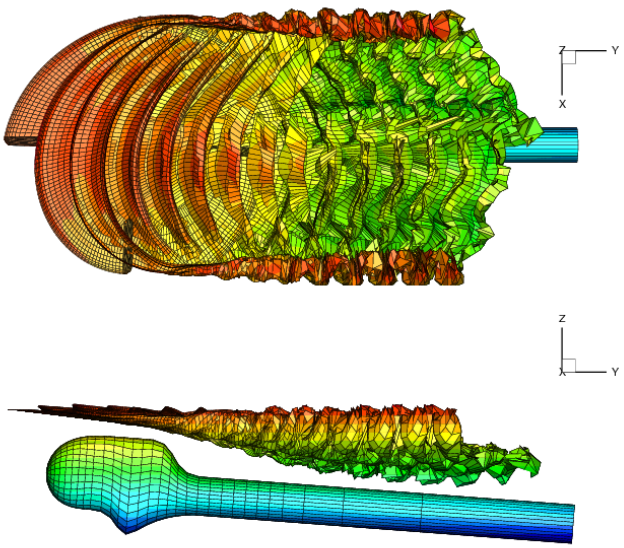

(f) Wake - Twist

Figure A.13: Wake visualization from different parameters from **UPM-BET** results, using the height as value